QUANTIFYING VEGETATION STRUCTURE AND FIRE FUELS IN MONTANE PINE FORESTS IMPACTED BY MOUNTAIN PINE BEETLE USING REMOTELY PILOTED AIRCRAFT SYSTEM MULTI-SPECTRAL, PHOTOGRAMMETRIC AND LIDAR TECHNOLOGIES

SAEID PARSIAN
Master of Engineering, Tafresh University, 2015

A thesis/project submitted
in partial fulfilment of the requirements for the degree of

MASTER OF SCIENCE

in

REMOTE SENSING

Department of Geography and Environment
University of Lethbridge
LETHBRIDGE, ALBERTA, CANADA

QUANTIFYING VEGETATION STRUCTURE AND FIRE FUELS IN MONTANE PINE FORESTS IMPACTED BY MOUNTAIN PINE BEETLE USING REMOTELY PILOTED AIRCRAFT SYSTEM MULTI-SPECTRAL, PHOTOGRAMMETRIC AND LIDAR TECHNOLOGIES

SAEID PARSIAN

Date of Defence: March 10, 2025

Dr. Laura Chasmer	Associate Professor	Ph.D.
Dr. Christopher Hopkinson	Professor	Ph.D.
Thesis Co-Supervisors		
Dr. Craig Coburn	Professor	Ph.D.
Thesis Examination Committee Member		
Dr. Christopher Watson	Ecologist, Parks Canada	Ph.D.
Thesis Examination Committee Member		
Dr. Marc Roussel	Professor	Ph.D.
Chair, Thesis Examination Committee		

DEDICATION

To my family.

ABSTRACT

Jasper National Park, one of the oldest Canadian national parks, has a long history of fire suppression. This has increased the homogeneity of mature pine forests within the park over time, and in recent years has been severely affected by mountain pine beetle (*Dendroctonus ponderosae*) outbreak. Tree mortality associated with Mountain Pine Beetle (MPB), dry fuels, and the potential for fire in the Athabasca and Miette Valleys is of significant concern to the park. Measuring forest fire fuels in the field is difficult and time-consuming, and field plots do not measure all the spatial variability of fuel distribution (though field measurements are effective for measuring surface organic layers (e.g., duff layers), which are difficult to measure using remote sensing or other techniques). Remote sensing platforms, such as remotely piloted aircraft systems (RPAS), can be used to quantify 3D structures and fuels, however, RPAS platforms and sensors have not been fully explored as a tool for identifying fuels in MPB-affected stands. Therefore, the objectives of this thesis are to: 1) quantify and compare fuel attributes using RPAS-photogrammetric, lidar point clouds and 2D multispectral imagery; and 2) examine the distribution of fire fuels based on the proportion of proportion of tree mortality, likely associated with MPB outbreak phases. To answer these objectives, geographic object-based image analysis (GEOBIA) was employed to identify vegetation species, MPB phases and map coarse woody debris. Then, 3D fuel attributes were quantified using RPAS-photogrammetric and -lidar point clouds (a single wavelength collected using the Zenmuse L1 sensor (as a comparison). The results indicated that GEOBIA effectively identified tree species and achieved an overall accuracy of approximately 90% compared to field-based validation. Photogrammetric point clouds were accurate for quantifying tree structures, including tree height (R^2= 0.96, Root Mean Square Error (RMSE)= 1.22 m, Normal Root Mean Square Error (NRMSE)= 6% and Bias=-0.34 m). Crown base height estimated using a novel region-based approach was also identified when compared with field-based validation (R^2= 0.76, RMSE= 2.29 m, NRMSE=17%, Bias= 0.73 m). RPAS-lidar point clouds demonstrate higher accuracy in measuring tree height (R^2= 0.99, RMSE= 0.59 m, NRMSE=3% and Bias= -0.23) and crown base height (R^2= 0.91, RMSE= 1.32 m, NRMSE= 8% and Bias= 0.16 m) compared with measured, illustrating the value of using lidar, especially in dense canopies. RPAS point clouds demonstrated moderate accuracy for estimating crown fuel load (R^2 = 0.38, RMSE = 1.92 kg. tree^{-1}, NRMSE=16% and Bias= 0.30 kg. tree^{-1}) Lastly, fuel distribution was assessed by comparing foliage volume and canopy fuel load and bulk density across 16 plots, and a downward shift was observed in canopy fuels over the progression of MPB outbreaks from green to gray phases. Unaffected plots (e.g., plot 15 (V = 2600 m^3) had greater foliage volume and canopy fuel load than affected plots (e.g., plot 11 (V = 515 m^3)).

CONTRIBUTIONS OF AUTHORS

I am responsible for all the data analysis and the writing of this thesis. The methods were developed by me with suggestions provided by Dr. Christopher Hopkinson, Dr. Laura Chasmer, Dr. Craig Coburn, and Dr. Christopher Watson.

Dr. Christopher Hopkinson conducted all the RPAS surveys, and the RPAS survey crew included Ben Pearse, Behnia Hooshyarkhah, and Italo Rodrigues. Forest plots measurements were supported by Tristan Skretting, Zhouxin Xi, Emily Jones, Dr. Laura Chasmer, and me. Tristan organized all field notes into a spreadsheet and prepared calculations of field measurements.

Dr. Laura Chasmer has managed the project as the principal investigator and guided the overall direction and funding for the project. Dr. Christopher Hopkinson provided technology and resources. The thesis committee members (Dr. Craig Coburn, and Dr. Christopher Watson) contributed by providing suggestions and ideas during all steps.

ACKNOWLEDGEMENTS

Many thanks to my supervisors Dr. Laura Chasmer and Dr. Christopher Hopkinson for their support, guidance, and patience throughout this degree. I would like to thank them for supporting me to present my research at several conferences and arranging field trips to enhance my understanding of forestry and wildland fire research.

Special thanks to Dr. Craig Coburn and Dr. Christopher Watson for being part of my supervisory committee and for their amazing support, guidance, and ideas during several progress and standing meetings.

I would like to express my appreciation to the people who supported me by providing funding, resources/data, and collaborations to Dr. Jonathan Boucher, Jasper National Park, fRI (Foothills Research Institute) Federal-Provincial MPB Research Partnership (Grant 247.150), the Mitacs Accelerate program (IT27605), NSERC SPG-N Canada Wildfire (NETGP 548629 – 19), and the Canadian Forest Service.

Thanks to the people in the "Dr. Laura Chasmer" and "ARTeMiS" labs for their support and help with collecting field data: Tristan Skretting, Zhouxin Xi, Italo Rodrigues, Behnia Hooshyarkhah, Ben Pearse, Emily Jones, Viviana Lartiga, and Celeste Barnes.

Table of Contents

LIST OF TABLES

LIST OF FIGURES

LIST OF ABBREVIATIONS

RPAS	Remotely Piloted Aircraft System
Lidar	Light Detection and Ranging
SfM	Structure from Motion
GEOBIA	Geographic Object-Based Image Analysis
CWD	Coarse Woody Debris
CBH	Canopy Base Height
DBH	Diameter at Breast Height
CFL	Canopy Fuel Load
CBD	Canopy Bulk Density
RMSE	Root Mean Square Error
MAE	Mean Absolute Error
NRMSE	Normal Root Mean Square Error
UAV	Unmanned Aerial Vehicle
TLS	Terrestrial Laser Scanning
DSM	Digital Surface Model
DEM	Digital Elevation Model
CHM	Canopy Base Height
ICP	Iterative Closest Point
PPP	Point Pair Picking
NG-CFFDRS	Next-Generation Canadian Forest Fire Danger Rating System
GNSS	Global Navigation Satellite System
NIR	Near Infrared
RE	Red Edge
SWIR	Short Wave Infrared
NDVI	Normalized Difference Vegetation Index
NDVIre	Red Edge Normalized Difference Vegetation Index
SVM	Support Vector Machine
ISODATA	Iterative Self-Organizing Data Analysis Technique
DT	Delaunay Triangulation
ITD	Individual Tree Detection
DBSCAN	Density-based Spatial Clustering of Applications with Noise
ENVI	Environment for Visualizing Imagery
FLS	Full Lambda Schedule
CSF	Cloth Simulation Filter
OA	Overall Accuracy
ROI	Regions of Interest
GCP	Ground Control Point
RTK	Real Time Kinematic

Chapter 1. Introduction

1.1 Introduction

Canada is known for vast and extensive forests, which cover approximately 40 percent of the land area (Natural Resources Canada, 2022). Climatic changes in the last decades in western Canada have led to increasing temperatures and the loss of moisture from both vegetation and soil, resulting in overall drier environments (Motha and Baier, 2005; Flannigan *et al.*, 2009). This, combined with longer fire seasons (days above 0º C) further increases the drying potential of vegetation, resulting in greater flammability of vegetation fuel. These changes are causing increasingly unpredictable wildland fires in western Canada, where fires are burning more intensely and over larger areas with greater ecological effects (Price et al., 2013; O'Neill, 2011). Fuel availability, fire weather, and ignition sources (e.g. human activities and lightning) can contribute to catastrophic wildland fires (Wang and Anderson, 2010; Johnston *et al.*, 2020; Coogan *et al.*, 2021). In addition to wildland fires, localized warming also exacerbates other disturbance factors including insect infestations, which, along with wildfires, are the main natural disturbances found in North American forests (Jenkins *et al.*, 2014). Given the complexity and frequency of these changes, remote sensing techniques have become essential for assessing forest conditions and monitoring disturbances such as wildland fires and insect outbreaks (Hanes et al., 2019; White et al., 2017; Hall et al., 2016).

1.2 Mountain Pine Beetle (MPB) Outbreaks

In mountain regions of western Canada, climate change has resulted in warmer winters in the last few decades which significantly increased the population of MPB (Embrey, Remais and Hess, 2012). This expansion is expected to continue into the next century (Brush and Lewis, 2024;

Hicke et al., 2006; Carroll et al., 2003). Milder winters associated with climate change have increased MPB, which would have increased spread MPB further north and east (Bentz et al., 2010; Logan et al., 2010). For example, Mitton and Ferrenberg, (2012) found that MPB life cycles have increased from one to two per year due to a 1.5° C rise in average air temperature, and longer growing seasons (above 0^{o} C) over the past two decades in Colorado, USA. In British Columbia and Alberta, forest mortality from MPB became widespread since the late 1990s (Perrakis et al., 2014; Axelson et al., 2011; Robertson et al., 2009; Aukema et al., 2006), increasing especially between 1999 and 2002. The MPB population experienced a second dramatic increase especially along the border between the two provinces in 2003 (Robertson *et al.*, 2009). In another study, Giroday et al., (2012) found that infestation in the Peace River region in British Columbia expanded from 10,000 hectares in 2004 to nearly 35,000 hectares by 2006 primarily through wind-driven dispersal. In total, more than 18 million hectares of pine trees were infested and died by 2011, equal to half of British Columbia’s merchantable timber (Cooke and Carroll, 2017).

1.3 MPB Outbreak Phases and Ecological Impact

MPB outbreaks can be identified and categorized based on the colour of needles and are divided into three phases: green (within 1 year since infestation), red (between 1 to 3 years since infestation), and gray (more than 3 years since infestation) (Klutsch *et al.*, 2009). During green phase, trees are still alive and appear healthy with green foliage, but they are infested. This phase occurs immediately after the beetles have attacked and laid eggs under the bark of the trees. Although the trees look green/healthy, infestation is difficult to detect because larvae actively feed on the inner phloem layer of trees and are not externally visible (Safranyik and Wilson, 2006).

MPB attack trees by first finding and locating suitable trees (typically mature lodgepole pines with thicker bark), then start boring through the tree bark to access the inner phloem layer to lay their eggs. As the larvae hatch, they start feeding and disrupt the vascular system of trees and obstruct their conductive tissues, impairing transportation of nutrients and water (Safranyik and Wilson, 2006). As a defense mechanism against beetle attacks, trees produce resin to expel beetles and microorganisms. To overcome this, MPB responds using pheromones causing a "Mass Attack", where many beetles concentrate on a single tree in a short period of time (Safranyik and Wilson, 2006) often overcoming the tree resulting in tree mortality (Safranyik and Wilson, 2006). MPB attack mature and older trees especially those with a diameter at breast height (DBH) greater than 25 cm (Safranyik and Wilson, 2006). Mature trees have thicker bark and phloem, which provide an ideal environment for reproduction (Safranyik and Wilson, 2006). In contrast, younger trees with thin bark and smaller stem diameter are less likely to be attacked or killed, as they are less suitable for brood production (Safranyik and Wilson, 2006; Dhar *et al.*, 2015). After approximately one year following infestation, trees die from a loss of moisture, resulting in the change of colour of needles from green to red, known as "red phase" (Page et al., 2013; Safranyik and Wilson, 2006; Wulder et al., 2006). At about three years following infestation, trees enter "gray phase" where dead trees have lost most of the needles and some branches, but the main tree stem can either remain standing for long period of time and will eventually fall (Jenkins et al., 2014). Therefore, the accumulation of dry fuel increases wildland fire hazard.

1.4 Mountain Pine Beetle Outbreak and Fire Fuel Availability

The normal life cycle of lodgepole pine (a species prone to MPB outbreaks) includes the stages of seedling, sapling, maturity, and old age. After a wildland fire or a disturbance, seedlings increase significantly and can reach up to ~1.40 m in 10 years (Mason, 1915). As seedlings develop into saplings, growth continues, and saplings reach about ~6 to 10 m in height between 30 and 50 years of age (Mason, 1915). Maturity is typically reached about ~18 to 25 m height of trees, occurring in about 140 years (Mason, 1915). While some trees can live longer, stands older than 250 years are uncommon and considered rare (Mason, 1915). However, in the case of MPB-affected lodgepole pine, these stages change significantly and a lodgepole pine tree can die about three years after being infested.

Knowledge of combustible material or “fuel” availability and fuel spatial and temporal distribution is critical for quantifying and forecasting fire risk, planning prescribed fires and predicting wildland fire behaviour (Hollis *et al.*, 2025). Forest fuel availability varies with time since outbreak and the phase of mortality (Simard *et al.*, 2011; Jenkins *et al.*, 2014). There are no large differences in fuel availability between unaffected or affected trees in green phase and dead conifers with red needles (red attack phase), however, trees in red phase are prone to intense fire due to the presence of dead/dry needles and branches in the canopy and fine fuel accumulation on the forest floor (Jenkins *et al.*, 2014). For example, Jenkins et al., (2014) found that the volume of fine fuel (needles and small branches) increases significantly at the onset of MPB infestation. Trees have lost most/all of the flammable canopy foliage in gray phase. Fine and downed woody debris continue to fall and accumulate on the forest floor, while many tree stems remain standing, others fall. Red and gray phases are important for fire hazard due to two factors: a) during the red phase trees have more flammable canopy material and dry biomass is still on trees as dry needles and small branches (Talucci and Krawchuk, 2019), b) forests remain in the gray phase for a longer period of time than other phases

Jenkins et al., (2014) also investigated the interactions among bark beetle outbreak, fuel availability and wildland fire. They found a significant increase in needle litter load during the early phase of infestation from the red phase which can ignite and promote fire spread. They also indicated that the amount of time it takes for different tree species to lose needles varies. For example, Engelmann spruce (*Picea engelmannii*) lose all needles in the first year of infestation, while lodgepole pine lose needles from between 1-3 years following infestation. Gray et al., (2021) explored spatial and temporal forest fuel changes based on MPB outbreaks in Montana, USA. Similar to other studies (e.g. Simard et al., 2011; Klutsch et al., 2009), they found that conifers lose almost all foliage resulting in gray phase. This shift/transfer from canopy to floor can take between 2 and 4 years from initial attack. Foliage/needle decomposition occurs typically within 2 and 5 years (Prescott *et al.*, 2000). Downed woody debris accumulation is more gradual and includes small and moderate diameter branches to coarse woody debris (larger branches and some fallen trees).

Space-for-time substitution is typically used as an effective ecological technique for quantifying forest fire fuel availability with time since infestation based on data from different locations and with varying conditions at the same time. Although space-for-time substitution can have limitations associated with complex ecosystems and environmental variability, it can be used to understand change without requiring repeat measurements required for time-series data (Enayetullah *et al.*, 2022).

Gibson et al., (2009) and Chen and Walton, (2011) describe that the transition from green to red foliage in infested trees typically occurs within almost one year. During the first year of attack, needles of infested trees generally begin fading 8 to 10 months after the initial attack. This starts with the change from green to yellowish-green, and then to red as the needles dry out and die. The primary cause of this color change is the disruption of water and nutrient transport within the tree, combined with colonization by fungi carried by the beetles, which further impair the vascular system of trees.

1.5 Quantifying Fuels Using Field Data

Field measurements are a necessary method for quantifying vertical and horizontal fuels for wildland fire and vegetation ecology at that location (Loudermilk *et al.*, 2022). Fuels are defined as any biomass (living or dead) which can burn or ignite in a fire. Dead fuel consists of dry and dead biomass such as foliage, branches or understory like grass, downed woody debris that have lost moisture and can burn.

Tree height and crown or canopy base height are commonly used metrics in fire behavior modelling. Generally, taller trees can lead longer flame lengths and lower canopy base heights increase the potential of transferring surface fires to trees and have crown fires. Crown/canopy fuel load and canopy bulk density, which are important metrics for understanding fire behaviour, can be estimated from tree metrics such as diameter at breast height, tree height, species and canopy base height (Andersen, McGaughey and Reutebuch, 2005) .

Despite the need for measured tree attributes, the installation of field plots has various limitations. It is difficult to install plots and measure vegetation in inaccessible areas, therefore plot measurements may not fully represent the range of variability of the broader area (Matasci *et al.*, 2018). It can also be time-consuming and expensive to collect field data at many plot locations, repeated every few years required to monitor forest change (Fassnacht et al., 2018; Hopkinson et al., 2004). To address these challenges, remote sensing has a long history of quantifying forest and tree attributes such as tree height, tree base height, biomass, foliage volume, among others over broader spatial areas, more frequently, and with less overall expense. Remote sensing remains a critical method to gather data and produce information that is important for understanding fuels in rapidly changing environments, and especially in those impacted by MPB over broad areas.

1.6 Quantifying Forest Fire Fuel and Remote Sensing

Passive optical remote sensing technologies record absorbed, transmitted and reflected electromagnetic radiation from objects on the Earth’s surface, typically onboard on satellites and airborne (aircraft and remotely piloted aircraft system) systems. Remote sensing can be used to identify a broad range of vegetation attributes such as vegetation or forest types (conifer, deciduous, etc.), canopy or vegetation cover, and vegetation condition (healthy or unhealthy) and many other attributes (Stueve et al., 2009; Falkowski et al., 2005). Most research on fire fuels over the past few decades has focused on quantifying the overstory canopy visible to these systems (Gale et al., 2021; Korhonen et al., 2017; Palaiologou et al., 2013; Wulder et al., 2012) as overstory canopy plays a critical role in fire spread, the varying predictability of fire behavior as well as the fire severity.

Given that objects (in this case vegetation) have a characteristic spectral response, and remote sensing systems measure the spectral response of objects visible to sensor optics. From these measurements, various forest attributes can be derived to better understand the spatial characteristics of vegetation fuels. Additionally, remote sensing technologies can detect variations in reflected/absorbed (etc.) electromagnetic radiation that may indicate changes, such as tree condition associated with MPB, fires, etc.

Remote sensing data collection began with aerial photography from platforms such as balloons or aircraft (Colwell, 1983). Spaceborne programs such as Landsat have been monitoring forest characteristics since the early 1970’s, however, in the last 25 years, high spatial resolution airborne lidar has become an important tool for quantifying fuels (Wehr and Lohr, 1999; Lefsky *et al.*, 2005; Chasmer *et al.*, 2017; Chamberlain, Sánchez Meador and Thode, 2021). More recently, in the last 15 years, optical and lidar systems have been developed for RPAS, enabling high spatial resolution multi-spectral and 3D structural characterization of vegetation (Berni *et al.*, 2009).

1.7 Quantifying Vegetation and Fuel Characteristics using Remotely Piloted Aircraft Systems (RPAS)

1.7.1 RGB and Multispectral Imagery

RPAS colour imagery (RGB) and multispectral imagery offers several advantages over satellite and airborne imagery including high spatial resolution (often < 5 cm) and greater flexibility (e.g. instantaneous launch, repeat deployment) for data acquisition including under cloud cover. This provides the level of detail and accuracy necessary to characterize more detailed attributes of vegetation, including for example, condition, composition, phenological cycles, and structure (Chadwick et al., 2022; Natesan et al., 2020; Franklin and Ahmed, 2018). RPAS can carry various sensors with different spatial resolutions, including RGB, multispectral, hyperspectral, lidar, and thermal sensors (Eugenio *et al.*, 2020). In this case, RGB, multispectral, and lidar are used for 2D and 3D mapping of forest fire fuels.

High spatial resolution RGB RPAS imagery offers valuable potential for mapping/monitoring vegetation/tree species, despite its limited spectral range. For example, Chadwick et al. (2022) demonstrated that tree species (e.g., lodgepole pine and white spruce) can be mapped using RGB imagery alone, through that the accuracy can be improved by adding additional spectral bands such as red edge and near infrared. Furthermore, Feduck et al., (2018) showed that high spatial resolution RGB RPAS imagery can effectively map forest structures like small seedlings. In addition to RGB bands, red-edge and near infrared are sensitive to vegetation health and species and enhancing the discrimination of tree species and conditions (Chadwick *et al.*, 2022). Vegetation indices like NDVI and Normalized Difference Vegetation Index red-edge

(NDVIre) can also provide additional information for better discrimination of tree species and conditions (Pearse, 2024; Ireland et al., 2021), Especially, NDVIre can help to identify early stressed vegetation, such as the green attack phase of MPB outbreaks, and is less sensitive to saturation (Delegido *et al.*, 2013).

RPAS imagery can be acquired at different flying heights above ground and the resulting images will have varying Ground Sampling Distances (GSD), which determine the area on the ground covered by each pixel. Spatial resolution refers to the sensors' ability to distinguish and resolve small objects or feature in an image. Smaller GSD and higher spatial resolution mean that more details can be observed in an image or recorded by the sensor, which plays a crucial role in the identification and classification of forest structures (Nuijten *et al.*, 2024). The high spatial resolution of RPAS imagery can be used to map many visible forest structures (Araujo *et al.*, 2020). Forest structural attributes such as canopy boundaries, gaps between trees, textures, and tones, can may be used to classify individual trees into tree species (e.g. aspen, lodgepole pine, white spruce, etc.) and forest types (such as coniferous, deciduous and mixed). In the case of wildland fire applications, high spatial resolution multispectral RPAS imagery and field data (for calibration and validation) along with machine learning can be effectively used for 2D mapping of forest fire fuel attributes (Bennett *et al.,* 2022).

In addition to 2D mapping forest fire fuels, RGB imagery can be used to produce 3D model and photogrammetric point clouds from a series of overlapped imagery using the structure from motion method (Xu et al., 2023; Tinkham and Swayze, 2021; Creasy et al., 2021; Iglhaut et al., 2019; Cooper et al., 2017; Wallace et al., 2016). Structure from motion estimates the three-dimensional coordinates of objects by processing overlapping images collected from different locations. This method uses sensor locations, platform orientations and flight height to identify common features within overlapping areas to reconstruct the spatial geometry of ground surface and estimate the three dimensional coordinates of objects using photogrammetric triangulation. These photogrammetric point clouds and also lidar point clouds can be used to quantify tree height, crown/canopy base height, diameter at breast height (using correlation models) and then can be used to model tree dry weight of biomass using allometric equations, which is an important input to canopy bulk density, which is used in fire behaviour models (Phelps et al., 2022; Lambert et al., 2005).

1.7.2 Geographic Object-Based Image Analysis (GEOBIA)

GEOBIA workflow is capable of identifying the shape of vegetation groups and/or features through 2D image segmentation, and within those groups, species (e.g. spruce, alder), characteristics/condition, etc. using, for example machine learning classification, which may be applied to 2D, 3D or a combination of both data types (Pearse, 2024; Sotille et al., 2022; Šiljeg et al., 2022; De Luca et al., 2019; Franklin and Ahmed, 2018).

Image segmentation is the first step of GEOBIA, where an image is divided into meaningful and homogeneous regions/objects based on similarities in spectral and structural characteristics (in this case, pixel values from multiple rasters). Each segment represents a group of similar pixels that can be grouped as one object, allowing classification algorithms (the second step of GEOBIA) to assign a class label to each segment. Image segmentation is a fundamental step in GEOBIA, as under- or over-segmentation can affect all aspects of the classification, including training/applying the machine learning model and the results of classification. Among all segmentation techniques, region-based approaches (such as Mean Shift (GIS), Full Lambda Schedule (NV5), Multiresolution Segmentation (eCognition (Trimble, German)), and Graph-based segmentation (Felzenszwalb)) are widely used in remote sensing (Kavzoglu and Tonbul, 2017). Kavzoglu and Tonbul, (2017) conducted a comparative evaluation of segmentation quality, demonstrating that region-based methods generally produce more accurate and homogeneous segments than edge-based approaches like watershed segmentation. In this thesis, segmentation was performed using NV5 software, which used a hybrid approach by integrating the Edge and Full Lambda, combining both edge-based and region-based methods.

A variety of classification methods and machine learning models are available to be trained in GEOBIA, such as K-Nearest Neighbors, Decision Trees, Support Vector Machine (SVM), Random Forest, etc. Among all of them, Random Forest and SVM are the most widely used algorithms (Jain *et al.*, 2020; Sheykhmousa *et al.*, 2020). Random Forest is particularly well-suited to large and complex datasets with mixed spectral signatures. In contrast, SVM performs well in the cases with limited training data (Chen and Hay, 2011). While many studies have reported strong performance using Random Forest, SVM was selected in this study because of the relatively small training dataset for some classes (e.g., white spruce and subalpine fir) as well as software limitations as the GEOBIA in NV5 does not support Random Forest (Sheykhmousa *et al.*, 2020).

Fernández-Guisuraga et al., (2022) used RPAS multispectral imagery to classify sapling and shrub species and to monitor regeneration and competition of pine saplings and shrubs following fire in 2013 in Spain. Two GEOBIA workflows were compared; 1) using 2D RGB and a 3D canopy height model (derived from photogrammetric point clouds: and 2) multispectral imagery (including red-edge and near infrared) with a canopy height model. With the use of red edge, near infrared and a canopy height model resulted in an overall accuracy of 83.67%, compared with RGB and a canopy height model (74.33%), then Random Forest Regression was then used to predict sapling/shrub (*Pinus pinaster, Halimium alyssoides, Pterospartum tridentatum* and *Erica* *australis*) competition. Cessna et al., (2021) quantified boreal vegetation health condition post-spruce beetle outbreak using RPAS multispectral data in Alaska. They used various spectral and structural variables to classify non-infested, green and dead trees with an overall accuracy of 78%.

GEOBIA can also be employed to map fuels and forest vegetation structures such as coarse woody debris and snags in relatively open canopies. For example, Lopes Queiroz et al., (2020 and 2019) mapped snags, logs, and other vegetation structures using RPAS multispectral imagery and lidar across a 270-hectare study area in the western Canadian boreal forest. RGB and near infrared wavelengths and NDVI were used for segmentation and Random Forest within shapes to classify logs, snags, water, dirt, and an ‘other’ classes. They found that classification was highly complete (completeness= 93.4%), and correct (correctness= 94.50%) for both snags and logs compared to validation data. Correctness refers to how many of the extracted objects or pixels were correctly classified and indicating the reliability of the classification. Completeness refers to how many of the objects or pixels in the ground-truth data were successfully classified and detected (Zhan *et al.*, 2005; Ye, Pontius and Rakshit, 2018). Although, RPAS multispectral imagery variations in spectral response from vegetation, canopy occlusion, shadow and similarity can reduce classification accuracy, especially lower in the canopy/understory/ground vegetation.

3D photogrammetric point clouds can be used with imagery to enhance the information obtained from RPAS imagery. Multiple images with different look directions and locations can be used to slightly tackle or mitigate canopy occlusion in relative open forest areas by using multiple overlapped images (Iglhaut et al., 2019). Photogrammetric point clouds are generated from surface imagery and cannot penetrate through dense canopy, leading to canopy occlusion and less/ not having points (information) on understory and ground vegetation.

1.7.4 RPAS 3D Point Clouds in Assessing Vegetation and Post-Fire Dynamics

Vegetation height is one of the fundamental attributes of fire behaviour modelling, as taller vegetation typically contains more biomass available to burn. This can result in greater flame lengths and faster rate of spread. Therefore it is crucial for modelling fire behavior, fire potential as well as fire intensity (Wang et al., 2024; Proulx, 2021; Beutling et al., 2012). Tree heights can be estimated using photogrammetric point clouds by interpolating the maximum elevation of above ground features and ground-classified points to create DSM and DEM, respectively (e.g. Birdal et al., 2017). Birdal et al. (2017) used a local maxima filter for individual tree identification and tree height, resulting in a SVM correlation coefficient (R^2) of 0.94 and a RMSE of 0.28 m compared with field measurements. Shin et al., (2018) also quantified several fuel and structural attributes using RPAS-derived predictor variables including height and canopy base height, percentile metrics and height-to-crown-diameter ratios. Correspondence with field measured was moderate for canopy height ($R^2 = 0.71$ and RMSE = 1.83 m), but, weaker for canopy base height ($R^2 = 0.34$ and RMSE = 2.52 m). They utilized a point-based segmentation algorithm developed originally by Li et al., (2012) to identify individual trees using RPAR SfM point clouds. This algorithm relies on a distance threshold method to group close points belonging to an individual tree. Then, tree density was determined using the number of trees in 10 m cells (100 m2) with 74% accuracy. Alonzo et al., (2018) used RPAS SfM point clouds and multispectral imagery to quantify boreal forest structure and tree species. Mean-shift segmentation was utilized to identify individual tree crowns, and then structural metrics (e.g., height) and spectral attributes were extracted. These metrics were then used to develop a Random Forest regression and classification models to estimate tree density, basal area and above ground biomass. They got 85% accuracy for tree species classification. Their results showed an R^2 ranged from 0.79 (basal area) to 0.92 (aboveground biomass).

Beyond its application in mapping forest fire fuels and vegetation structures, RPAS imagery and point clouds can also be used to map forest disturbances (e.g., burnt or unburnt, cutlines, anthropogenic, seismic lines) and monitoring post-fire vegetation regeneration. For example, Arkin et al., (2019) conducted a study on fire severity mapping using RPAS imagery and photogrammetric point clouds in British Columbia, one month following the Prouton Lakes Fire. Various structural and textural variables were used to train/apply Random Forest classifiers (a machine learning algorithm that builds an ensemble of decision trees learning method (Breiman, 2001)) to generate disturbance-based land cover maps, including burnt/unburnt coarse woody debris, undisturbed, moderately, and heavily disturbed at trees. Following fire, Castilla et al., (2020) estimated individual boreal conifer seedling height using ultra high resolution RPAS imagery at three ground pixel sizes: 0.35, 0.75 and 3 cm, to create photogrammetric point clouds. The maximum point elevation of each seedling was subtracted from the ground elevation to determine seedling height. Best accuracies compared with ground-truth data were achieved for seedling heights of >30 cm with 0.35 cm pixel size (RMSE = 24 cm; bias = −11 cm; $R^2 = 0.63$; n = 48).

1.7.5 RPAS Lidar Point Clouds

Passive remote sensing has been widely utilized for forest and wildland fire applications. Passive remote sensing also have limitations such as limited visibility of the forest floor due to canopy occlusion and limiting the ability to assess understory vegetation (Keane, Burgan and van Wagtendonk, 2001). To address these limitations, lidar reduces occlusion effects by collecting multiple returns from a single laser pulses resulting measuring both over and understory vegetation

(Hopkinson et al., 2005; Lefsky et al., 1999). Lidar is a remote sensing technology that emits laser pulses to the ground and record the time it takes to travel to the ground and return. By recording this time and using the speed of light, the distance between each ground point and the sensor can be calculated. Additionally, a GNSS antenna records the geographic coordinates of the sensor, while the Inertial Measurement Unit (IMU) captures the orientation of the platform (roll, pitch, and yaw). Using the coordinates and platform orientations, along with the accurate laser pulse locations, the 3D coordinates of the ground can be generated (Wehr and Lohr, 1999; Hopkinson, 2006). In addition to lidar, other active sensors like Radar and SAR can be used to measure forest structural and moisture attributes (Saatchi et al., 2007; BAKER et al., 1994; Le Toan et al., 1992). However, this thesis focuses on lidar systems.

Lidar sensors can be used on various platforms including fixed and rotary wing aircraft and RPAS. Typically, aircraft are employed to collect lidar data over larger areas, while RPAS platforms are flown at lower altitude, collecting dense lidar point clouds over smaller areas (one or more hectares) (Beland *et al.*, 2015).

Lidar data are used to predict forest attributes using two approaches: area-based and individual tree-based (White *et al.*, 2013). Area-based approaches involve utilizing lidar point cloud metrics (e.g., height percentiles, mean height, max height, min height, point density, etc.) within fixed spatial units such as plots or grid cells and using statistical models to predict forest attributes at the plot or stand level. In contrast, individual tree-based approaches are designed to detect individual trees directly from the lidar point cloud, extracting tree-specific metrics such as tree height, canopy cover, etc. Area-based methods are more commonly applied than tree-based approaches, especially in the case of airborne lidar data for larger areas (e.g. Cameron, 2020; Vastaranta et al., 2012). This is because area-based approaches do not need high-density point clouds, however, tree-based methods need dense point clouds to ensure sufficient points for accurately detecting individual trees. Furthermore, area-based approaches are time and computationally efficient. Additionally, the lack of highly accurate individual tree detection algorithms is another limitation for large-scale applications (Yu *et al.*, 2010). For example, Cameron, (2020) quantified boreal fuel characteristics using airborne lidar point clouds and area-based approaches. This included canopy height, canopy base height, canopy fuel load, canopy bulk density, and stem density derived using three lidar point cloud densities: high (10.5 pulses per m^2), moderate (4.7 pulses per m^2), and low (1 pulse per m^2). It was found that high-density lidar data has better accuracy for all fuel attributes than moderate- and low-density data compared with field data (R^2 range 0.51 (canopy base height) and 0.85 (canopy fuel load)). Although this demonstrates that airborne lidar is an effective system for quantifying fuels and with acceptable accuracy, tree-based methods can provide detailed information at the tree level, allowing for species-specific modeling and accurate estimation of attributes such as biomass, height, crown size, and stem distribution (Yu *et al.*, 2010). Furthermore, relying on some statistical and prediction models and limited field data may not be effective for different ecosystems and study areas (White *et al.*, 2013). These prediction models often have limitations, and they are highly dependent on the quality and diversity of forest plot data. They are often ineffective for diverse forest conditions or ecosystems and cannot be used to extrapolate beyond the training data. In forestry and forest fire fuel, these models are highly sensitive to plot design, and inappropriate design can lead to bias and reduce model reliability and accuracy (White *et al.*, 2013).

Although airborne lidar systems are suitable for large-area fuel assessments, RPAS lidar is an effective system for measuring vegetation structures and elevation due to high density point clouds. These can be used to quantify fuel characteristics, independent of field data. For example, Puliti et al. (2020) estimated growing stock volume of boreal trees with RPAS lidar data and RGB imagery. A 2D segmentation approach and high spatial resolution RPAS imagery were employed to identify tree boundaries. These boundaries were then used to detect points associated with each tree using RPAS lidar point clouds. From there, two Random Forest regression were trained to estimate tree species and DBH. To prepare the training data for these models, the Random Sample Consensus (RANSAC) algorithm (performed in the *TreeLS R*) and visual interpretation were used to create samples for tree species and DBH. Then, specific-species volume models (Brantseg, (1967)) were utilized to predict the volume of each tree.

Arkin et al., (2023) compared RPAS lidar and photogrammetric point clouds with ground-based lidar for estimating canopy fuel metrics at the plot level. Iterative closest point was employed to co-register all these point clouds and remove offsets and warps between them. Iterative closest point is a point cloud registration approach which works based on iteratively matching the closest points and using least squares to find the best rotation, translation, and linear scaling. Various predictor variables including: height percentiles, maximum height, canopy relief ratio and others were used to develop linear regression models to predict fuel attributes including canopy fuel load, canopy bulk density, canopy base height and other important metrics.

Results showed that RPAS lidar generally produced more accurate and consistent predictions of canopy fuel characteristics (stand height, canopy fuel load, canopy bulk density, canopy base height, etc.) compared to photogrammetric point clouds and ground-based lidar, however none of these technologies were effective for estimating DBH-related metrics such as stand density index, basal area and quadratic mean diameter.

RPAS technology has been widely utilized in recent years for a variety of applications, offering new opportunities for environmental, vegetation and fuel assessment in challenging environments like mountain forests (Wallace *et al.*, 2012; Goodbody *et al.*, 2017; Eugenio *et al.*, 2020). Given these capabilities, this platform presents many opportunities to enhance our understanding of vegetation structures and available fuels for wildland fire. However, several research knowledge and research gaps remain, which will be explained in the next subsection.

1.8 Research Gaps

Field measurements are the primary and necessary method for quantifying forest fire fuels. While vegetation measurements are necessary, ground-truth data collection has limitations especially across highly variable MPB affected trees (Wulder et al., 2006). In MPB outbreak stand areas, fuel conditions can be highly variable due to mixed stages of tree mortality and making it difficult to capture representative measurements with sparse plots. Moreover, accessing these areas may be challenging or have safety issues due to standing unstable dead trees. Additionally, field measurements are time-consuming, expensive, and inefficient for large and hard to access areas. Therefore, there is a need to develop/apply alternative methods for quantifying fuel availability in MPB impacted forest stands using high spatial resolution and cost-effective remote sensing platforms like RPAS.

Currently, there is limited understanding of how RPAS systems (optical and point clouds) can be used and compared for quantifying fuel metrics at tree and plot levels, especially in areas impacted by MPB. This presents a need for evaluation of RPAS data (optical imagery and point clouds) for quantifying fuel characteristics in complex forest environments to address these needs, several steps are required: first, there is a need to test methods for georeferencing RPAS datasets especially in case of photogrammetric data with 3D distortions and nonlinear scaling problems. Studies have used both direct (post-processed kinematic and real-time kinematic) which require expensive equipment and indirect (ground control points) georeferencing. This method is labour-intensive, expensive and challenging in forests due to revegetation and occlusion of ground control points in forest environment(Padró *et al.*, 2019; Liu *et al.*, 2022). Therefore, there is need to compare methods for georeferencing RPAS datasets in complex forests as accurate alignment/registration is essential to eliminate offsets between datasets collected from different platforms before data fusion.

Second, there is a need to compare and improve methods for identifying tree species and characteristics associated with fuel availability in both stands and those affected by MPB (Sambaraju *et al.*, 2012; Jenkins *et al.*, 2014; Edwards, Krawchuk and Burton, 2015; Bernier *et al.*, 2016). Understanding the effectiveness and accuracy for quantifying vegetation structures may be useful for rapid fuel assessment and use in fire behaviour models. Finally, it is important to understand how MPB infestations change the spatial distribution of available fuels, including the shift of canopy fuel to the forest floor based on the proportion of tree mortality within a given area/plot mostly associated with MPB infestation.

1.9 Thesis Objectives

To address these needs, this thesis has two main objectives: First, to develop/apply methods for quantifying fuels in MPB-affected forests using three RPAS systems. The second is to quantify the distribution of fuels based on MPB attack phase and tree mortality.

The first objective included: 1) comparison of methods for georeferencing RPAS imagery to point clouds from airborne lidar data; 2) implementation of a classification to identify tree species and general forest structures using RPAS imagery; and 3) development and comparison of SfM vs. lidar 3D methods for quantifying fuels in forests impacted by MPB. In Objective 2, the results of Objective 1 were used to better understand how tree mortality and the accumulation of fuels changed over time since initial infestation.

The outcomes of this study are important for forest managers and decision-makers who want to use RPAS data to map fuels and for planning and implementation of management activities of forest areas, especially in the years following pine beetle attack.

1.10 Thesis Organization

This thesis is divided to seven chapters, with most chapters (shortened for text) contributing to a single journal article:

1. The second chapter describes the study area, data collection, and the materials used in this study.
2. The third chapter includes the methodology and results of preprocessing three RPAS datasets including RPAS imagery, photogrammetric and lidar point clouds. This chapter includes the workflow for aligning and registering RPAS point clouds and multispectral imagery with airborne lidar point clouds.
3. The fourth chapter describes the methodology and findings related to using RPAS multispectral imagery, structural information and GEOBIA for identifying tree /species and mapping coarse woody debris. Additionally, this chapter discusses the distribution of canopy coarse woody debris coverage (the total surface area covered by coarse woody debris in each plot (~400 m^2)) aassociated with mortality.
4. The fifth chapter presents the workflow for quantifying 3D canopy fuels using RPAS point clouds from trees identified using methods in Chapter 4. Tree structure and fuel estimates were compared at the tree level, while canopy fuel load (CFL) and canopy bulk density (CBD) were calculated and compared at the plot level. This chapter contributes to Objective 1 and Objective 2 of this thesis. beetle using vertical vegetation profiles and calculates the total fuel load in each plot.

5. The sixth chapter is the discussion chapter. This discusses the workflow developed throughout the thesis and provides future suggestions and recommendations by comparing results with the literature.
6. The final chapter, Conclusion, summarizes how each chapter addresses the research objectives and provides a discussion of future opportunities.
7. An appendix includes all the scripts developed for this thesis.

Chapter 2. Study Area and Materials

2.1 Study Area

Jasper National Park (52°N, 118°W) is approximately 350 kilometers west of Edmonton Alberta in the Canadian Rocky Mountains and was a perfect location for this thesis research (Figure 2.1). The park was established in 1907 as Jasper Forest Park, later became a national park in 1930 (James-Abra, 2011). The park is situated within Treaty 6 and Treaty 8, on the traditional territories of the Anishinabe, Aseniwuche Winewak, Dene-zaa, Nêhiyawak, Secwépemc, Stoney Nakoda, Mountain Métis, and Métis Peoples (Government Of Canada, 2025). Field plots, RPAS and airborne lidar and photogrammetric/multi-spectral data were collected along the Athabasca Valley south of the town of Jasper. Based on a weather station located at 52° 53' 00" N, -118° 04' 00" and elevation 1062.2 m (named Jasper) the average air temperature in Jasper National Park is ~3.3^{o}C and the average annual total annual precipitation is 1958 millimeters (Canadian_Climate_Normals, 2024).

Jasper is home to a variety of tree species including *Pinus contorta* (lodgepole pine), *Picea glauca* (white spruce), *Picea engelmannii* (Engelmann spruce), *Abies lasiocarpa* (subalpine fir), *Pseudotsuga menziesii* (Douglas fir), and *Populus tremuloides* (trembling aspen). MPB mostly attack mature lodgepole pine but may attack other pine species like: jack pine, ponderosa pine and limber pine (Safranyik and Wilson, 2006)). The climate of JNP is favourable for the growth of many tree species and is ideal for pine species (Rhemtulla et al., 2002; La Roi and Hnatiuk, 1980) due to a long history of fire suppression. Recent wildland fires in Jasper, especially the Chetamon fire (2022) and the Jasper Fire Complex 2024, which burned ~30% of the town have highlighted the real threat that wildland fire poses to the Town of Jasper and its surrounding forest areas and infrastructure. Additionally, Jasper includes important montane ecosystems, which provide various benefits including carbon sequestration, economic/natural resources value, wildlife habitat, and numerous other benefits (Rollins, 2012; Kulshreshtha et al., 2000).

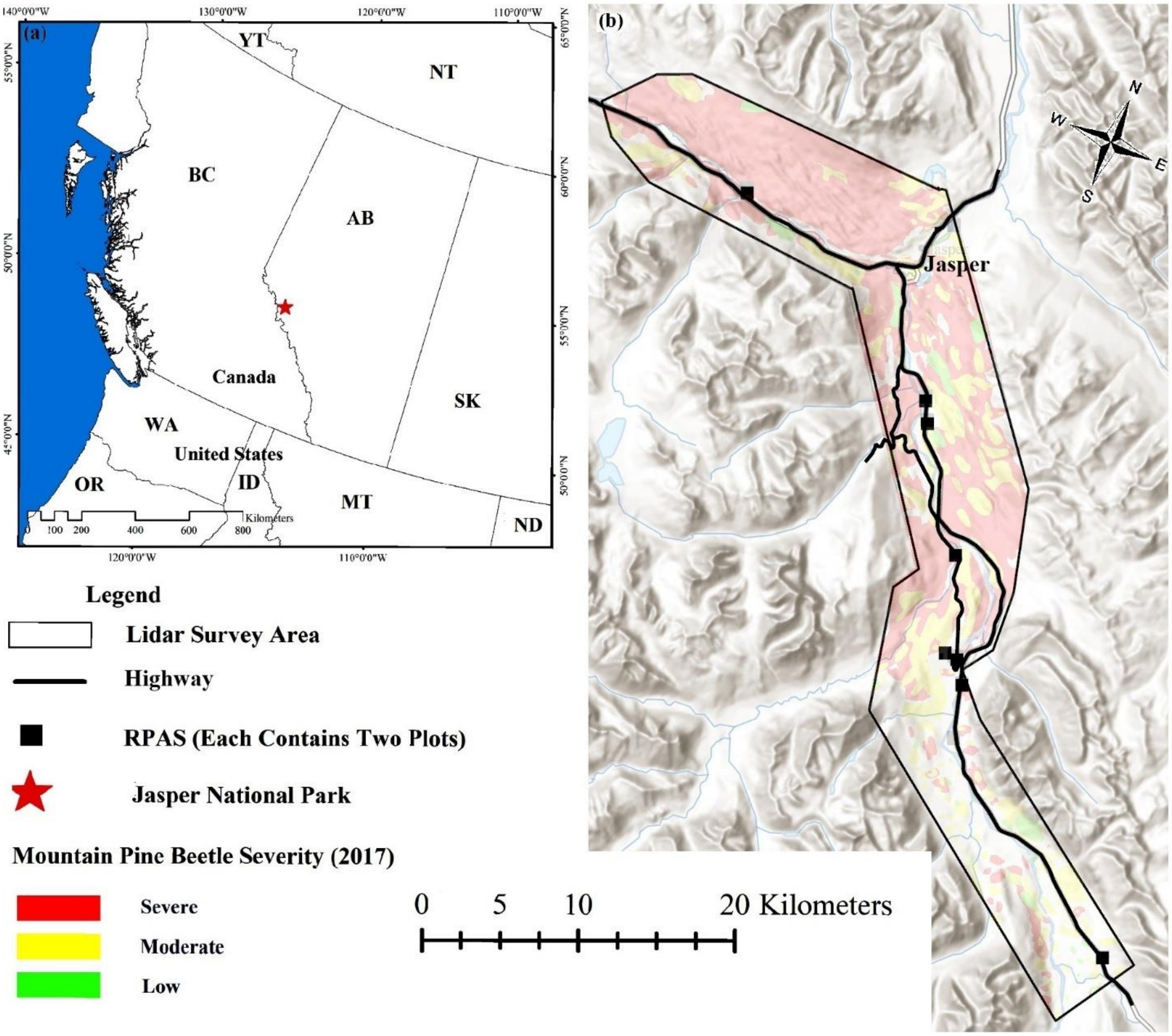

Figure 2.1, (a) The location of the study area in Alberta, Canada; (b) Three airborne lidar polygons south and west of the Town of Jasper. The location of RPAS polygons are also shown, each of which include two field plots. The map also illustrates the severity of MPB infestations observed in 2017 (provided by Parks Canada).

2.2 Field Data

Tree measurements (DBH, crown base height, tree height, tree species, etc.) were collected in 16 forest mensuration/fuel plots (Figure 2.1) using methods described within the Next-Generation Canadian Forest Fire Danger Rating System (NG-CFFDRS) during the summers of 2021 and 2022 (Figure 2.2) (Skretting et al., 2025; Boucher et al,. 2022). Field measurements were used to parameterize allometric models of above ground biomass and crown fuel load (Hollis et al., 2025; Phelps et al., 2022; Ung et al., 2008; Lambert et al., 2005). Tree metrics were also used to validate the proposed methodology and results.

Plot locations were identified using Google Earth and geospatial survey layers provided by Parks Canada (Figure 2.1) across a range of different proportions of tree mortality. GNSS receivers were utilized to measure the location of the plot center. Tree plots covered an area of ~400 m^2 (radius = 11.28 m). These also included a subcanopy plot (radius = 3.99 m (50 m^2)), four regeneration plots (each covering 1 m^2), and a surface fuel plot (radius = 5.64 m (100 m^2)) (Figure 2.2). Within each 11.28 m radius plot, all trees with DBH>3 cm were measured. Measurements included: DBH, crown base height, tree height, tree species and condition (living, pine beetle phase, snag). To do these measurements, a Vertex Hypsometer (Hagloff Inc. Sweden) and a DBH tape were used to measure height and DBH, respectively. Two transects (40 m) were laid out in northeast-southwest and northwest-southeast directions using a compass. These were used to measure coarse woody debris greater than 3 cm diameter including diameter, decomposition status (rotten or sound), location (elevated or on the ground), bearing, and distance from the transect start (Figure 2.2).

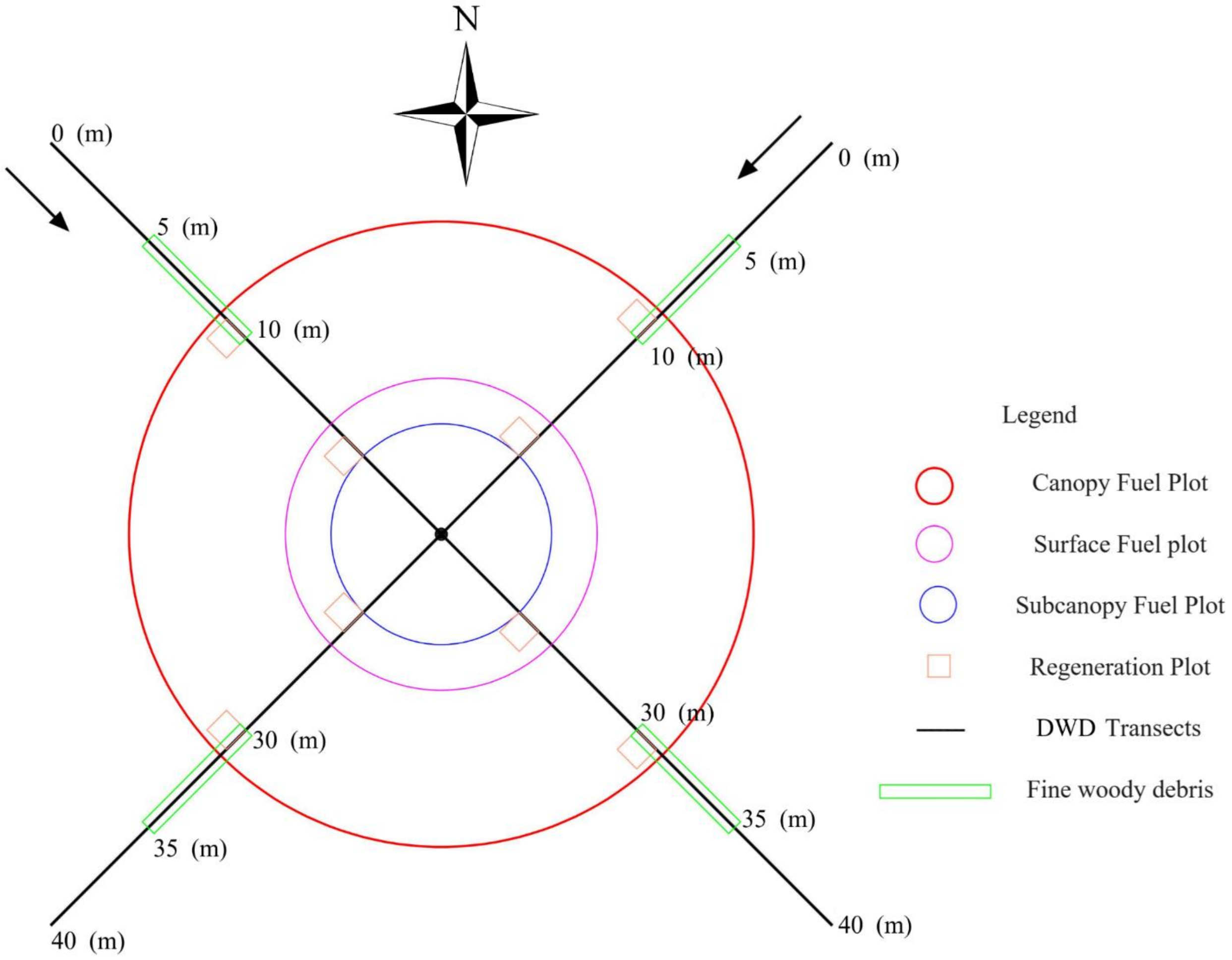

Figure 2.2, Vegetation fuel plot layout at Jasper National Park, including the location of two transects, subcanopy fuel plots and regeneration plots. Figure reproduced from Boucher et al, (2022).

2.3 Remotely Sensed Data

2.3.1 RPAS Data Collections

2.3.1.1 RPAS Survey 2021

Optical (RGB and multi-spectral) data were collected using 6 RPAS survey polygons (each polygon containing 2 plots) across six ~150 m x 150 m areas (Plots 1-12) using DJI Inc. Mavic Pro V2 and Phantom 4 Multispectral sensors. RPAS RGB imagery were collected at a flying height of approximately 60 metres above ground level with almost 90% front and sidelap. There was minimal shadow in almost all imagery due to smoke in the atmosphere as a result of ongoing wildland fires. The Phantom 4 Multispectral collected multispectral data across five bands: green (560 ± 16 nm), blue (450 ± 16 nm), red (650 ± 16 nm), red edge (730 ± 16 nm), and near-infrared (NIR) (840 nm ± 26 nm)) (DJI, 2020). Ground Sample Distance (GSD) for RGB imagery was ~0.013 metres (~1.3 centimetres) and multispectral imagery was collected with GSD of ~0.032 metres (or ~3.2 centimetres). The flight pattern for collecting RGB (Mavic 2 Pro) was double grid (90° cross), and Parallel lines (unidirectional) for collecting multispectral imagery (Phantom 4 Multispectral). Image capture modes for collecting RGB imagery using Mavic Pro V2 and Phantom 4 Multispectral were Fast mode (non-stop) and Waypoint (hover & stare), respectively. While RGB imagery collected with 15º forward tilt, multispectral imagery was collected at nadir (0º). RGB imagery collected by Mavic 2 Pro were processed using the structure-from-motion (SfM) algorithm in Pix4D Mapper software (Pix4D, Switzerland) to generate photogrammetric point clouds and orthomosaics. DJI Terra (DJI Technology Co., Ltd, China) was also used to process multi-spectral bands collected by Phantom 4 Pro. Table 2.1 provides more details about RPAS imagery and photogrammetric point clouds.

Table 2.1, Summary of 2021 RPAS flights specifications.

Year	Platform	Sensor	Flight Height (m)	Flight Pattern	Camera Tilt	GSD (cm)	Front/sidelap	velocity	Image Capture Mode	Notes
2021	Mavic 2 Pro	RGB	60	Double grid (90° cross)	15º forward	~1.5	90% / 90%	3-4 m/s	Fast mode (non-stop)	Minimal shadowing, due to smoke in the atmosphere
	Phantom 4 MS		60	Parallel lines (unidirectional)	0º (nadir)	~3.2	NA	2.5 m/s	Waypoint (hover & stare)	Minimal shadowing, due to smoke in the atmosphere

2.3.1.2 RPAS Survey 2022

RPAS lidar data and multispectral imagery were collected using the DJI Matrice 300 with Zenmuse L1 sensor and Phantom 4 Multispectral across two additional RPAS polygons (plots 13-16). All specification of multispectral imagery collection were the same as the summer 2021. Moreover, lidar data collections were conducted at 60 metres above ground level in a single direction parallel line (no grid) with nadir facing RGB sensor for collecting RGB orthoimages. Furthermore, the lidar system operated at 160 KHz with three returns per pulse and a laser scan sidelap of 75%. DJI Terra (DJI Technology Co., Ltd, China) was also used to produce both all RPAS data and imagery collected in the summer 2022 (lidar and RGB orthoimages collected by DJI Matrice 300 and multispectral bands (red, green, blue, near infrared and red edge) collected by Phantom 4 Pro). While plots 13 and 14 were collected in shadow condition, plots

15 and 16 were collected in cloudy condition with minimal shadow. Table 2.2 provides more details about RPAS imagery and lidar point clouds.

Table 2.2, Summary of 2022 RPAS flights specifications.

Year	Platform	Sensor	Flight Height (m)	Flight Pattern	Camera Tilt	GSD (cm)	Front/Sidelap	velocity	Image Capture Mode	Notes
2022	Matrice 300	Zenmuse L1	60	Parallel lines	0º (nadir)	~1.6	80% / 85%	3.5 m/s	Fast mode (non-stop)	Lidar: 160 kHz,3 returns/pulse, 75% scan overlap, ~1367 pts/m^2
	Phantom 4 MS		60	Parallel lines (unidirectional)	0º (nadir)	~3.2	NA	2.5 m/s	Waypoint (hover & stare)	

2.3.2 Airborne Lidar Data

Three airborne multispectral lidar polygons were surveyed east, south and west of the Town of Jasper (Figure 2.1). Airborne multispectral lidar data were collected at three wavelengths (1550 nm SWIR, 1064 nm NIR and 532 nm green) using a Teledyne Optech Inc. Titan sensor (North York, Canada) at maximum foliage cover during summer of 2021 and 2022. Data were used to align and register all RPAS data to a common reference system and eliminate all offsets/warps.

2.4 RPAS Plots and Tree Mortality Calculation

Figures 2.3-2.5 illustrate tree mortality calculation across 16 forest plots using field observations along with visual representations from RGB imagery, photogrammetric plots (Plots 1-12) and lidar (Plots 13-16) point clouds. For each plot, the total number of trees (excluding snags and aspen trees) and dead trees with red needles or without needles were counted. Afterward, the proportion of tree mortality was calculated by dividing the total number of dead and partially dead trees (with red or no needles) by the total number of trees in each plot (excluding snags and aspen trees). This proportional approach addresses limitations identified in recent literature, where studies frequently used categorical MPB phases (e.g., green, red and gray) rather than proportional measures (Romualdi, Wilkinson and James, 2023) In this thesis, all analyses related to forest fire fuels and comparisons were based on these calculated percentages of tree mortality.

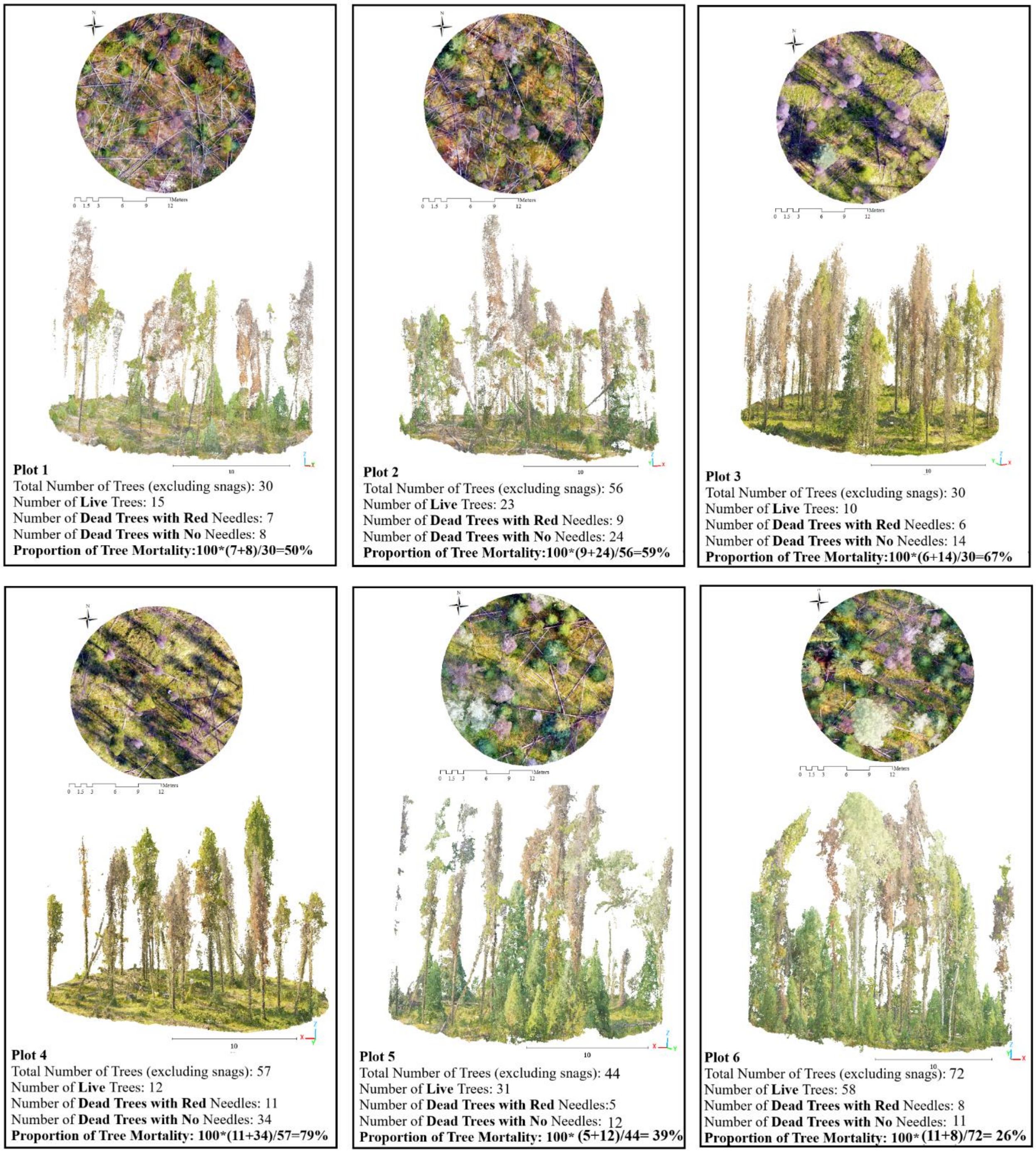

Plot 1
Total Number of Trees (excluding snags): 30
Number of **Live** Trees: 15
Number of **Dead Trees with Red** Needles: 7
Number of **Dead Trees with No** Needles: 8
Proportion of Tree Mortality:100*(7+8)/30=50%

Plot 2
Total Number of Trees (excluding snags): 56
Number of **Live** Trees: 23
Number of **Dead Trees with Red** Needles: 9
Number of **Dead Trees with No** Needles: 24
Proportion of Tree Mortality:100*(9+24)/56=59%

Plot 3
Total Number of Trees (excluding snags): 30
Number of **Live** Trees: 10
Number of **Dead Trees with Red** Needles: 6
Number of **Dead Trees with No** Needles: 14
Proportion of Tree Mortality:100*(6+14)/30=67%

Plot 4
Total Number of Trees (excluding snags): 57
Number of **Live** Trees: 12
Number of **Dead Trees with Red** Needles: 11
Number of **Dead Trees with No** Needles: 34
Proportion of Tree Mortality: 100*(11+34)/57=79%

Plot 5
Total Number of Trees (excluding snags): 44
Number of **Live** Trees: 31
Number of **Dead Trees with Red** Needles:5
Number of **Dead Trees with No** Needles: 12
Proportion of Tree Mortality: 100* (5+12)/44= 39%

Plot 6
Total Number of Trees (excluding snags): 72
Number of **Live** Trees: 58
Number of **Dead Trees with Red** Needles: 8
Number of **Dead Trees with No** Needles: 11
Proportion of Tree Mortality: 100* (11+8)/72= 26%

Figure 2.3, Tree mortality calculation for Plots 1-6 using field data along with visual representations from RGB imagery and RPAS-SfM point clouds.

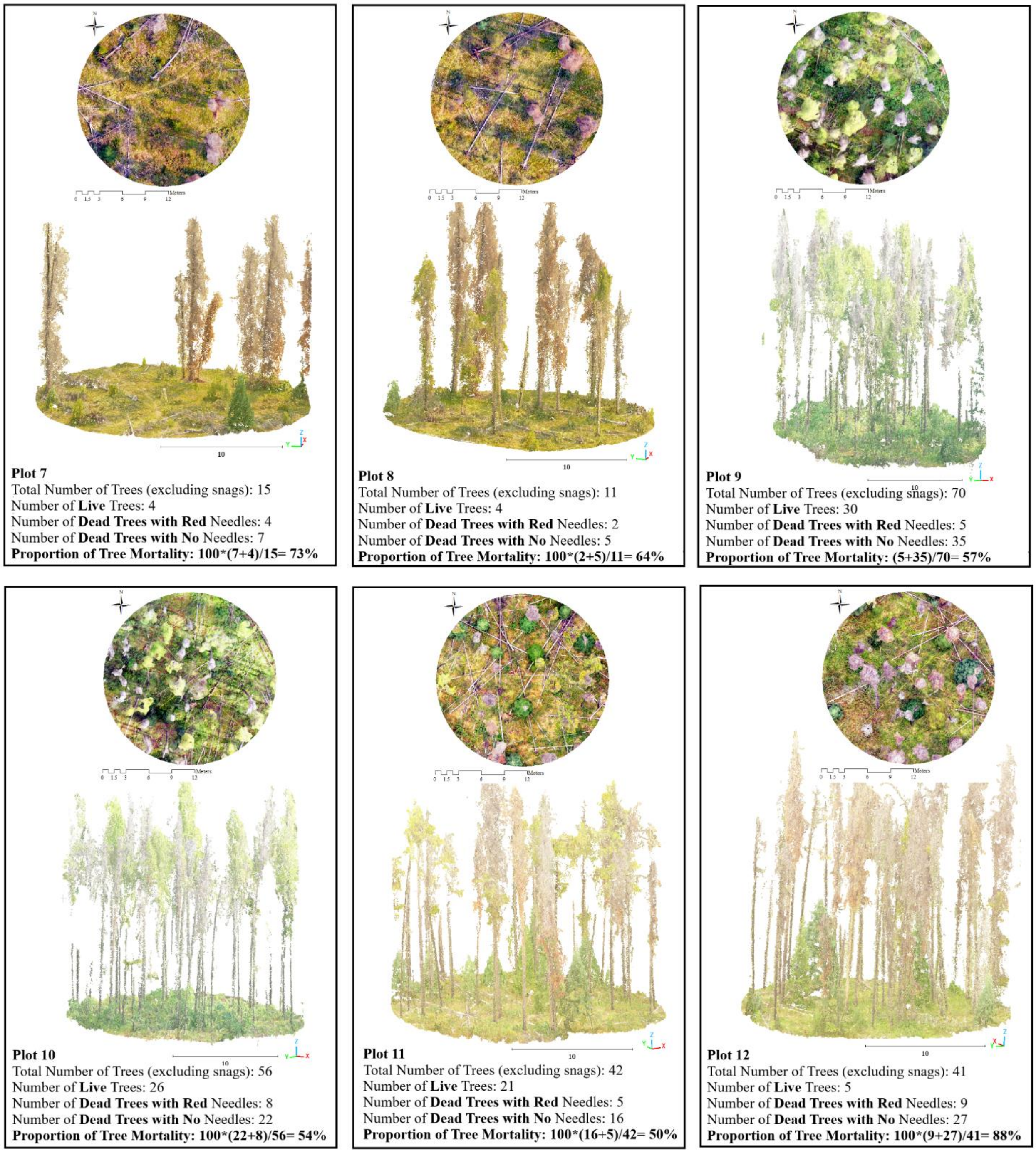

Plot 7
Total Number of Trees (excluding snags): 15
Number of **Live** Trees: 4
Number of **Dead Trees with Red** Needles: 4
Number of **Dead Trees with No** Needles: 7
Proportion of Tree Mortality: 100*(7+4)/15= 73%

Plot 8
Total Number of Trees (excluding snags): 11
Number of **Live** Trees: 4
Number of **Dead Trees with Red** Needles: 2
Number of **Dead Trees with No** Needles: 5
Proportion of Tree Mortality: 100*(2+5)/11= 64%

Plot 9
Total Number of Trees (excluding snags): 70
Number of **Live** Trees: 30
Number of **Dead Trees with Red** Needles: 5
Number of **Dead Trees with No** Needles: 35
Proportion of Tree Mortality: (5+35)/70= 57%

Plot 10
Total Number of Trees (excluding snags): 56
Number of **Live** Trees: 26
Number of **Dead Trees with Red** Needles: 8
Number of **Dead Trees with No** Needles: 22
Proportion of Tree Mortality: 100*(22+8)/56= 54%

Plot 11
Total Number of Trees (excluding snags): 42
Number of **Live** Trees: 21
Number of **Dead Trees with Red** Needles: 5
Number of **Dead Trees with No** Needles: 16
Proportion of Tree Mortality: 100*(16+5)/42= 50%

Plot 12
Total Number of Trees (excluding snags): 41
Number of **Live** Trees: 5
Number of **Dead Trees with Red** Needles: 9
Number of **Dead Trees with No** Needles: 27
Proportion of Tree Mortality: 100*(9+27)/41= 88%

Figure 2.4, Tree mortality calculation for Plots 7-12 using field data along with visual representations from RGB imagery and RPAS-SfM point clouds.

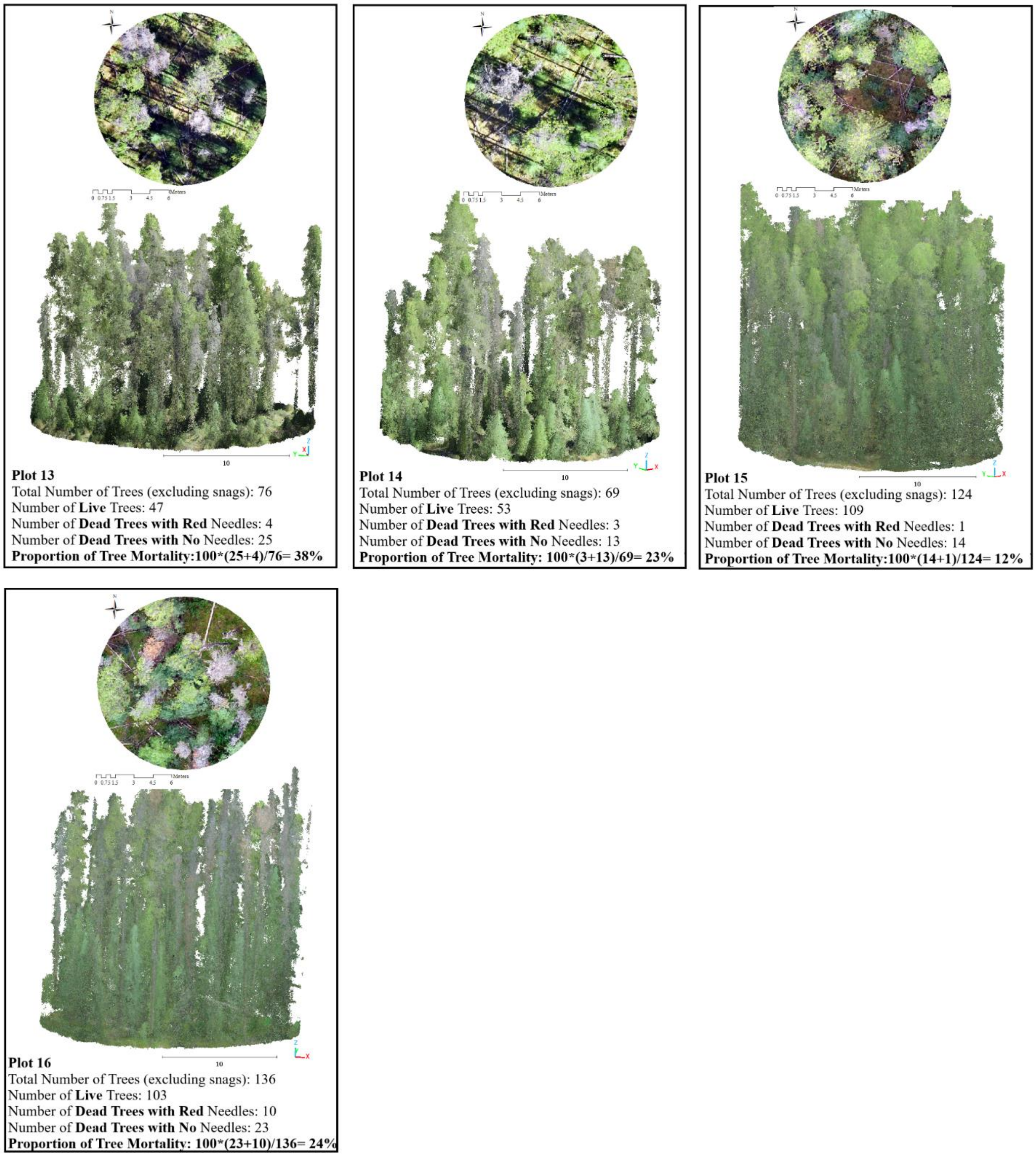

Plot 13
Total Number of Trees (excluding snags): 76
Number of **Live** Trees: 47
Number of **Dead Trees with Red** Needles: 4
Number of **Dead Trees with No** Needles: 25
Proportion of Tree Mortality:100*(25+4)/76= 38%

Plot 14
Total Number of Trees (excluding snags): 69
Number of **Live** Trees: 53
Number of **Dead Trees with Red** Needles: 3
Number of **Dead Trees with No** Needles: 13
Proportion of Tree Mortality: 100*(3+13)/69= 23%

Plot 15
Total Number of Trees (excluding snags): 124
Number of **Live** Trees: 109
Number of **Dead Trees with Red** Needles: 1
Number of **Dead Trees with No** Needles: 14
Proportion of Tree Mortality:100*(14+1)/124= 12%

Plot 16
Total Number of Trees (excluding snags): 136
Number of **Live** Trees: 103
Number of **Dead Trees with Red** Needles: 10
Number of **Dead Trees with No** Needles: 23
Proportion of Tree Mortality: 100*(23+10)/136= 24%

Figure 2.5, Tree mortality calculation for Plots 13-16 using field data along with visual representations from RGB imagery and RPAS-lidar point clouds.

2.5 Data Processing and Analysis

2.5.1 Field data processing to determine tree and plot level canopy fuel load

Tree species, DBH and tree height were used to estimate crown fuel load using allometric equations for each individual tree (Phelps et al., 2022; Ung et al., 2008; Lambert et al., 2005). In this case, foliage biomass was considered as the crown fuel load for healthy/green conifers, branch biomass for dead conifers with no needles, and both foliage and branch biomass for dead conifers with red needles affected by MPB (Talucci and Krawchuk, 2019). Mixed plots with deciduous trees (such as aspen) were excluded from the fuel calculations due to their different burning characteristics compared to coniferous species. Plots dominated by aspen trees (Plots 17 and 18) were excluded, while in mixed plots (Plot 5 (5 aspen trees) and Plot 6 (6 aspen trees)) were included with those aspen trees removed from the analysis. The estimation of foliage and branch biomass (kg. tree^{-1}) was calculated using Equations 1 and 2 from Ung et al., (2008). After calculating the fuel load for each individual tree, the total canopy fuel load (CFL) at the plot level was calculated by adding all tree CFLs within each plot. This total was then divided by the plot area (400 m^2) to estimate the CFL in kg m^{-2}.

$$\text{Canopy fuel load (foliage)} = \mathrm{B}_1 * \mathrm{D}^{\mathrm{B2}} * \mathrm{H}^{\mathrm{B3}} + \mathrm{e}_1 \qquad (1)$$

$$\text{Canopy fuel load (branches)} = \mathrm{B}_4 * \mathrm{D}^{\mathrm{B5}} * \mathrm{H}^{\mathrm{B6}} + \mathrm{e}_2 \qquad (2)$$

Where H and D indicate the height and diameter at breast height of each tree, respectively. Tables 2.1 and 2.2 display values for $B_1 – B_6$ for different conifer species observed and measured in those 16 plots. Additionally, ' e_1 and e_2 ' represent the error terms.

Table 2.3, Parameters of DBH and height-based allometric equations for foliage biomass estimation (Ung, Bernier and Guo, 2008).

	Subalpine Fir		**Lodgepole Pine**		**White Spruce**		**Black Spruce**	
	B (foliage)	e_1	B (foliage)	e_1	B (foliage)	e_1	B (foliage)	e_1
$\mathbf{B_1}$	0.0509	0.3855	0.0769	0.2015	0.1832	0.1171	0.2078	0.1143
$\mathbf{B_2}$	2.9909		2.6834		2.4144		2.5517	
$\mathbf{B_3}$	-1.2271		-1.2484		-1.0948		-1.3453	

Table 2.4, Parameters of diameter at breast height and height-based allometric equations for branch biomass estimation (Ung, Bernier and Guo, 2008).

	Subalpine Fir		**Lodgepole Pine**		**White Spruce**		**Black Spruce**	
	B (branches)	e_2	B (branches)	e_2	B (branches)	e_2	B (branches)	e_2
$\mathbf{B_4}$	0.0265	0.4121	0.0285	0.2138	0.0322	0.1252	0.0405	0.1186
$\mathbf{B_5}$	3.6747		3.3764		2.8961		3.1917	
$\mathbf{B_6}$	-1.5958		-1.4395		-0.9203		-1.3674	

2.6 Summary of field and remotely sensed data collections

This chapter discussed field data collection and measuring common forest fire fuel such as tree height, crown/canopy base height, crown/canopy fuel load and understory fuel including coarse woody debris using NG-CFFDRS. Additionally, RPAS high resolution RGB, multispectral imagery, and lidar point clouds were collected using three RPAS platforms in MPB-affected areas. Photogrammetric point clouds were created using the structure from motion (SfM) method and derived from the RGB imagery. SfM is a photogrammetric method that reconstructs 3D model of structures (in this case vegetation) from overlapping images. It involves some steps such as interior orientation, where camera parameters such as focal length are applied. Then, exterior orientation is performed, which estimates the cameras' spatial position and orientation. SfM performs relative orientation by automatically matching features across multiple overlapping images to define the geometric relationships between them. Afterwards, bundle adjustment is applied, a global least-squares optimization, to refine all interior and exterior parameters by minimizing reprojection error. Finally, absolute orientation is applied using GNSS data to georeference the reconstructed 3D model or point (Westoby *et al.*, 2012; Roberti *et al.*, 2021). Figure 2.6 introduces the workflow of the methodologies used in this thesis and described in Chapters 3, 4, and 5: pre-processing of RPAS optical, multispectral, and lidar data (red), object-based analysis and RPAS imagery (light green), and 3D fuel attributes and volumetric quantification of tree and fuel characteristics (dark green), including data inputs (top) and derivatives (bottom).

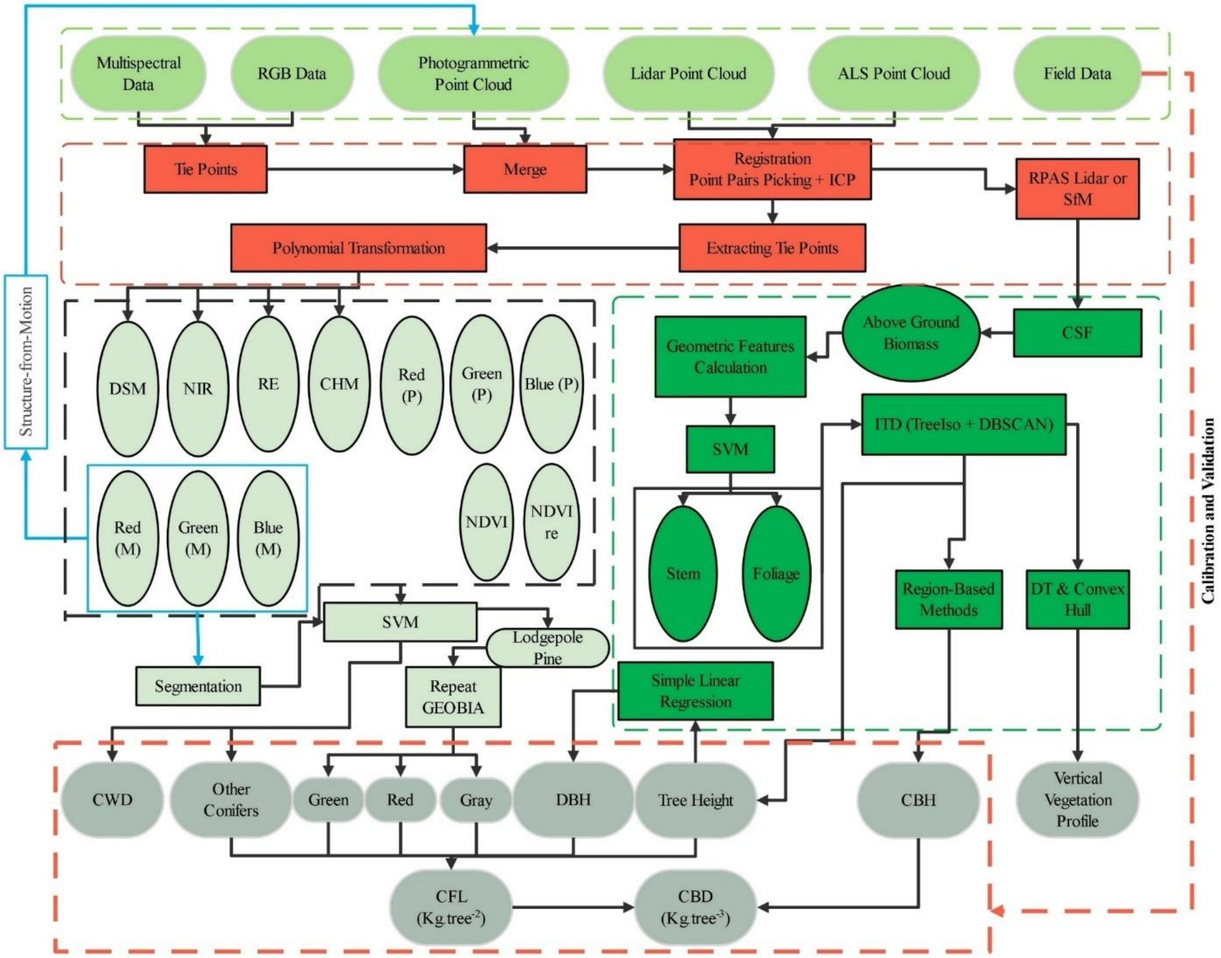

Figure 2.6, An overview of the workflow including inputs (top, green), alignment/registration of RPAS data (red shapes outlined with a red dashed line), application of GEOBIA to identify objects (coarse woody debris and tree species) (light green with dashed line) and application of 3D methods to quantify fuel attributes using photogrammetric and lidar point cloud data (dark green with dashed line). Data derivatives are at the bottom, gray. ((M) in GEOBIA section refers to bands collected with the Mavic 2 Pro or Matrice 300, while (P) refers to bands collected with the Phantom 4 Multispectral Pro. ICP: Iterative Closest Point; CSF: Cloth Simulation Filter; ITD: Individual Tree Detection; DBSCAN: Density-based spatial clustering of applications with noise; DT: Delaunay Triangulation.

Chapter 3. Geocorrection of RPAS Point Clouds and Multispectral Imagery

3.1 Introduction

Differences in platforms and acquisition technologies can introduce spatial offsets and warping between remote sensing datasets, as well as between field data and GNSS data, especially when using multiple platforms. Furthermore, photogrammetric datasets are prone to georeferencing errors due to challenges in absolute orientation and limited image overlap near the edges of survey polygons. Although Real-Time Kinematic (RTK)-equipped platforms can improve geolocation accuracy, there are still some offsets between datasets captured by different platforms. Therefore, ground control points (GCPs) remain an important component for achieving the highest possible georeferencing accuracy (Padró *et al.*, 2019), however, deploying and recording GCPs in forested areas is time-consuming, labour-intensive, and often impractical. A robust and efficient workflow is therefore needed to ensure all datasets are spatially aligned to enable reliable data fusion and cross-comparison.

This chapter discusses the workflow and accuracy assessment of aligning and registering various RPAS datasets, including RGB, multispectral imagery, photogrammetric, and lidar point clouds to a consistent spatial reference. The main purpose of this chapter is to apply a workflow that removes the offsets and warps between various RPAS data and field or airborne lidar data. This ensures comparability and enables data fusion as the first step in the processing workflow. Furthermore, it allows us to use field observations and ground-truth data to calibrate the RPAS imagery and validate all results. To do this, airborne lidar data were used as a reference and all RPAS data was aligned/registered to airborne lidar. ICP has been widely utilized for point cloud registration in remote sensing (Sang et al., 2022; Li et al., 2020). However, it is prone to local minima errors especially in the case of photogrammetric point clouds that require nonlinear translation and scaling (Cao et al., 2023; Decker et al., 2020; Maiseli et al., 2017; Yang et al., 2016; Xie et al., 2010). To improve the performance and accuracy of ICP, Qi et al. (2022) proposed using cloud-to-cloud distance measurements with a 5 cm threshold for re-registration. Although this method mitigates the problem with falling in local minima errors, it is time-consuming and less effective for correcting nonlinear distortions. In this chapter, a workflow was developed to register RPAS photogrammetric and lidar points to airborne lidar point clouds which are highly accurate in terms of georeferencing.

3.2 Methods

The first step towards ensuring comparability between datasets (field, RGB, multispectral, and both photogrammetric and lidar point clouds) is to register datasets to a consistent spatial reference system. This enables the use of cost-effective and affordable RPAS platforms without Real-Time Kinematic positioning or installation of ground control points especially in challenging forest environments. In this case, airborne lidar data collected coincident to field data collections were used due to high locational accuracy of laser returns. To do this, an average of 15 tie points (identifiable locations that can be observed in both images between multispectral and RGB data were manually selected based on the same identifiable features (typically the intersection of two coarse woody debris stems identified in both datasets) with distribution across the image/point cloud to ensure consistent geometric alignment throughout the image requiring registration. Tie points were then merged with RPAS point clouds. Afterwards, RPAS point clouds (with tie points) were registered to airborne lidar data. Tie points in the registered RPAS point clouds were then extracted to align the RPAS imagery. To do this, the global polynomial transformation (Equation 3, using the “Warp” toolbox in ArcMap 10.8.1) was applied (using the initial tie points as reference and the tie points after registration as targets) to align both the multispectral and RGB data with the airborne lidar data (Tondewad and Dale, 2020).

$$\begin{aligned} \mathrm{X_n} &= \mathrm{a_0 + a_1x_0 + a_2y_0 + a_3x_0y_0 + a_4x_0^2 + a_5y_0^2} + \cdots \\ \mathrm{Y_n} &= \mathrm{b_0 + b_1x_0 + b_2y_0 + b_3x_0y_0 + b_4x_0^2 + b_5y_0^2} + \cdots \end{aligned} \tag{3}$$

Where x and y are the coordinates of the tie points before point cloud registration and X and Y are the coordinate of the tie points extracted from registered point clouds. Figure 3.1 shows the performance of different polynomial transformation orders for the geometric correction of an orthoimage. The first-order transformation applies consistent translation, rotation, and linear scaling across the entire image and making it suitable for aligning lidar datasets. In contrast, the second-order polynomial introduces non-linear adjustments such as scaling, translation, and rotation, which are needed for aligning photogrammetric datasets. Although the third-order transformation is rarely used in remote sensing, it can introduce significant image warping and potentially generate no data areas due to overfitting (Esri, 2025). First and second-order polynomial transformations require at least three and six tie points, respectively. Additionally, increasing the polynomial transformation order (third or higher) results in more freedom for deformation (and require more tie points), generating visible distortions. Therefore, it the second order is optimal for registering photogrammetric imagery as this avoids such distortions. Figure 3.1 shows the performance of the first-, second- and third polynomial transformations on a small part of Plot 12.

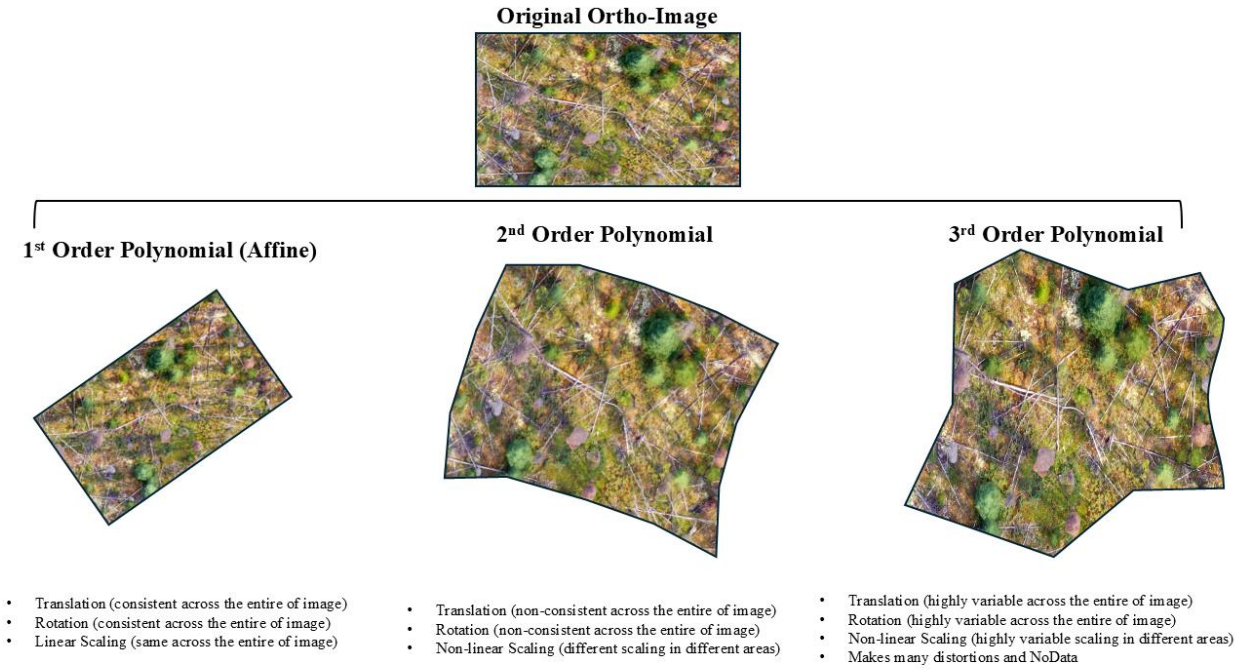

Figure 3.1, The comparison of 1st, 2nd, and 3rd order polynomial transformations on an example of ortho-images (Esri, 2025)

Point cloud registration was also implemented using Point Pair Picking (as initial registration in CloudCompare) and Iterative Closest Point (ICP) algorithms in CloudCompare software (Appendix 2) (Besl and McKay, 1992). The ICP algorithm utilizes the least-squares method to find the optimal registration through translation, rotation, and linear scaling transformations to minimize the Euclidean distance between corresponding points in two point clouds (Persad *et al.*, 2017). Here, Point Pair Picking in CloudCompare was utilized as an initial registration, using at least three points (mostly tree tops) extracted from the digital surface models of RPAS and airborne lidar point clouds, for ICP. This initial registration aims to increase accuracy by mitigating challenges related to linear scaling and to avoid convergence to local optima, which is a common challenge when using ICP (He et al., 2023; Li et al., 2022; Zhang et al., 2015). To enhance the optimal performance of ICP, the root mean square difference was set to 1×10^{-7} (the minimum value supported by CloudCompare). Additionally, with a 100 percent overlap, the random sampling limit ranged between 1 to 2 million points. Lastly, due to the need to adjust rotation along all axes, the rotation adjustment was set through the XYZ axes.

Due to 3D distortions in photogrammetric point clouds, a non-linear scaling registration (a combination of point pair picking (PPP) and ICP (both in CloudCompare software) was implemented for georeferencing all photogrammetric data. In contrast, lidar point clouds were registered using simple translation, rotation, and linear scaling registration (ICP). Thus, PPP and ICP were used for registering photogrammetric point clouds. ICP was used for registering lidar point clouds. PPP was used to address two issues. First, PPP mitigates the scaling problem of ICP in the case of photogrammetric point cloud registration. Second, it decreases the distance between two point clouds to prevent ICP from falling into local minima. It is worth noting that ICP alone was also examined for photogrammetric point clouds.

3.2.1 Testing and Accuracy Evaluation

The evaluation and accuracy assessment of RPAS point cloud registration was determined using RMSE and the sample points automatically selected by CloudCompare software during the ICP step, while the coordinates of the center of plots collected using GNSS were employed to evaluate the georeferencing accuracy of RPAS multispectral and optical imagery.

3.3 Results

In the absence of GNSS and ground control points during photogrammetric data collection in the summer of 2021 (plots1-12), significant vertical (over 20 m) and horizontal (0.5-4 m) offsets/warps were observed between RGB and multispectral data collected by RPAS, field, and airborne lidar data (Figure 3.2).

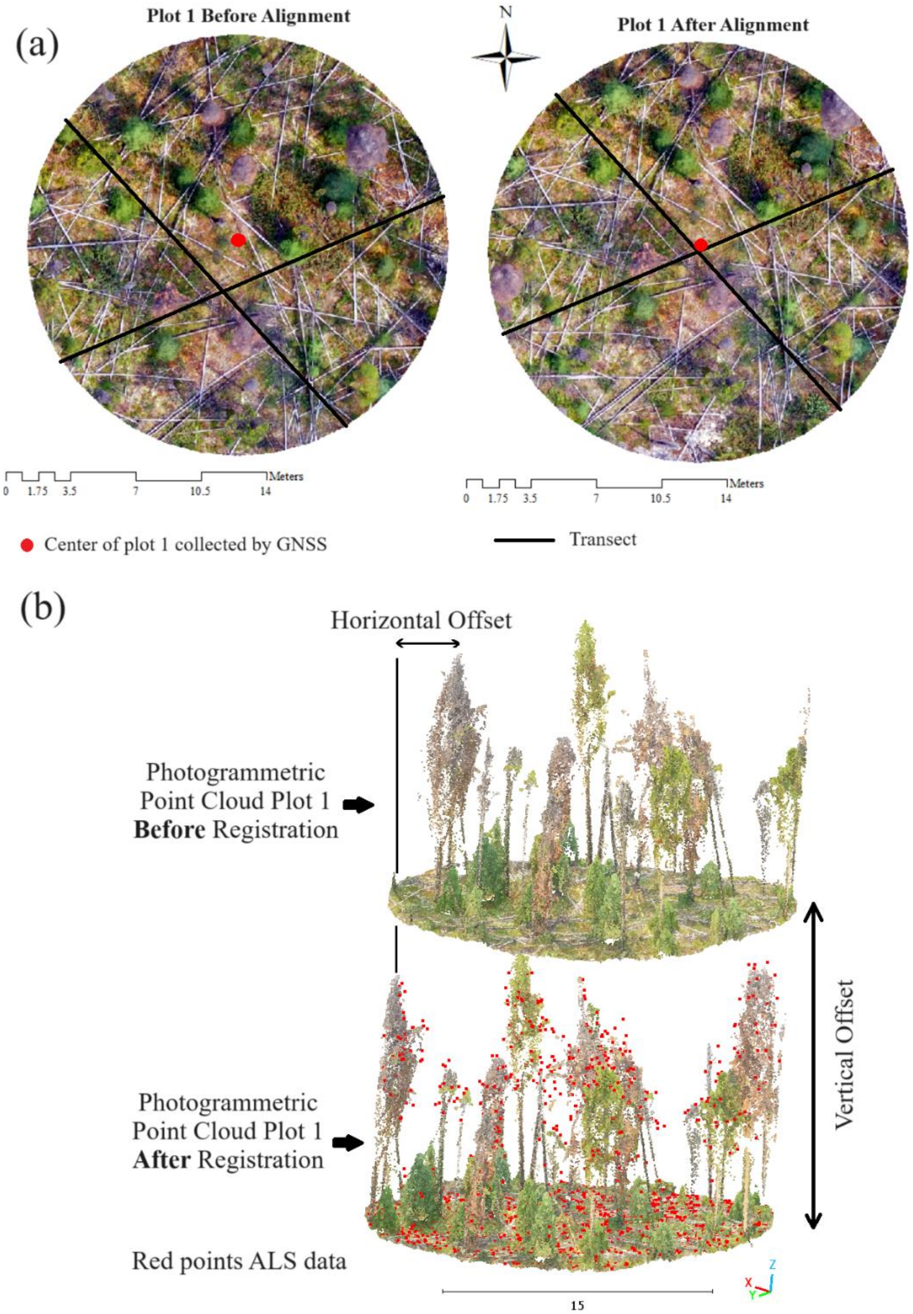

Figure 3.2, A sample (Plot 1) of vertical and horizontal offsets/warps between RPAS data and airborne lidar data: a) Horizontal offsets between the center of RPAS imagery (the intersection of two tape measures indicated by black lines in a) and the coordinates collected with GNSS; b) Vertical and horizontal offsets between the RPAS point cloud (RGB) and airborne lidar point cloud (red points).

Table 3.1 presents the RMSE for 12 plots using photogrammetric point clouds and 4 plots using lidar point clouds. The average RMSE for point cloud registration for the ICP only and the combination of PPP and ICP for all 16 plots were 0.72 and 0.30 m respectively. Furthermore, the average offset between the centers of the plots and GNSS was ~1.30 m before alignment decreasing to ~0.22 m after alignment.

Table 3.1, RMSE for point cloud registration using point pair picking (PPP) and Iterative Closest Point (ICP) for 16 plots, as well as the offset values of plot centers before and after alignment using polynomial transformation for 14 plots. Plots 15 and 16 centre was not geographically located (NA).

Technique	RPAS Polygon	RMSE for ICP Only (m)	RMSE for PPP+ICP (m)	Offset Before Alignment (m)	Offset After Alignment (m)
Photogrammetric	Plots 1&2	0.44	0.23	2.58	0.11
	Plots 3&4	1.96	0.44	1.09	0.30
	Plots 5&6	0.43	0.30	0.29	0.12
	Plots 7&8	0.39	0.28	1.18	0.36
	Plots 9&10	1.52	0.21	1.15	0.14
	Plots 11&12	0.32	0.28	1.11	0.33
Lidar	Plots 13&14	0.33	0.33	1.62	0.24
	Plots 15&16	0.36	0.36	NA	NA

3.5 Summary Outcomes

Due to the lack of real-time kinematic (RTK) or differential RTK as well as ground control points, there were horizontal offsets (ranging from 0.50 to 4 meters) and vertical offsets (ranging from 1 and 20 meters) between RPAS and airborne lidar data. In this chapter, PPP, ICP and polynomial transformation have been employed to eliminate these offsets to ensure a consistent spatial system. It was found that ICP alone was not sufficient for photogrammetric point cloud registration and requires a nonlinear scaling registration as an initial registration to improve the registration accuracy. The second-order polynomial transformation was effective for aligning RPAS imagery.

Chapter 4. 2D Mapping Forest Structures and Tree Species Using Geographic Object-Based Image Analysis (GEOBIA) and RPAS Multispectral Imagery

4.1 Introduction

Accurate classification of tree species and their conditions is critical for forest fuel quantification, particularly for estimating crown fuel load, as well as for assessing forest health in MPB-affected areas. Although field-based methods remain essential for calibrating and validating fire fuel models, they are often limited by safety hazards, high costs, and labour-intensive requirements, particularly in remote and densely forested areas. As a solution, high spatial resolution RPAS imagery with structural attributes can be used to identify tree species. Furthermore, forest structures such as Coarse Woody Debris (CWD) are also important for monitoring fuel dynamics associated with insect outbreaks, wildland fire, or fuel treatments.

Despite the high spatial and temporal advantages of RPAS datasets, traditional pixel-based classification techniques are often not effective for classifying tree species, their conditions, as well as forest structures such as CWD. Therefore, there is a growing need to explore advanced classification frameworks, such as Geographic Object-Based Image Analysis (GEOBIA).

This chapter discusses the workflow for classifying general forest structures such as tree species and coarse woody debris, using GEOBIA and RPAS multispectral imagery and structural information (e.g., CHM and DSM). GEOBIA involves image segmentation, and a machine learning algorithm (in this case support vector machine, SVM) were employed to classify tree species and map forest structures such as coarse woody debris. Additionally, statistical analysis (confusion matrix) was employed to assess the accuracy of the results. This chapter also discusses the challenges (such as shadow and canopy occlusion) of using GEOBIA and RPAS imagery for these classifications.

4.2 Methods

4.2.1 Geographic Object-based Image Analysis Procedure

Identification and classification of forest structures (e.g., tree species or coarse woody debris) were carried out using vegetation indices, multispectral and RGB bands, and structural metrics including the DSM and CHM) within GEOBIA and an SVM machine learning model. RGB imagery from the Mavic Pro V2 was used for image segmentation, due to higher spatial resolution (20 Megapixels). A hybrid method, integrating Edge and Full Lambda Schedule, was employed in ENVI (Environment for Visualizing Images) software (version 5.6, NV5) (Calin et al., 2021; Redding et al., 2002). This hybrid segmentation method utilized the Edge Method (using the Sobel edge detector) to identify homogeneous objects such as tree boundaries and coarse woody debris. Full Lambda Schedule was used to merge adjacent segments iteratively based on spectral similarity to produce image segments (Griffith and Hay, 2018).

4.2.2 Object-Based Classification of Tree Species, MPB Phases and Coarse Woody Debris

GEOBIA is an advanced classification workflow that segments imagery into homogeneous objects based on spectral, and structural information. Unlike traditional pixel-based methods, GEOBIA allows the use of spatial and shape-based attributes such as shape, area, length, etc., making it particularly effective for high spatial resolution imagery. Pixel-based classification assigns a class to each individual pixel based solely on its pixel values and spectral characteristics. While this approach is effective for moderate or coarse resolution imagery (e.g., Landsat imagery), pixel-based approaches are more prone to noise and misclassification in the case of high-resolution RPAS imagery. Therefore, segmentation is a critical step for classifying high spatial resolution RPAS imagery to classify each segment rather than individual pixels. Image segmentation is also an approach to divide the study area into homogeneous objects based on similarity in spectral or structural attributes. Following the segmentation approach, statistical metrics (e.g., mean, max, min, SD, etc. of all pixel values in each segment) were calculated to train a machine learning model (e.g., Random Forest, Support vector machine (SVM), k-nearest neighbors (KNN)). While many papers prove the robustness and effectiveness of Random Forest, the SVM algorithm was selected due to its effectiveness in handling high dimensional data with limited and small training samples. It also performs well with complex, high spatial resolution imagery and avoids overfitting or underfitting (Chen and Hay, 2011).

SVM algorithm was implemented using various spectral and spatial attributes used to differentiate between tree species (e.g., lodgepole pine, subalpine fir, white spruce), MPB phases (e.g., green, red and gray) and coarse woody debris within GEOBIA identified shapes. Although Random Forest has been shown to be effective in similar studies (e.g., De Luca et al., 2019), SVM was selected due to the limited amount of training data for certain classes (e.g., subalpine fir and white spruce), as well as software limitations, specifically, NV5 does not support Random Forest. Tree species and coarse woody debris were classified using spectral attributes including minimum, maximum, standard deviation, and mean per each raster, as well as shape-based attributes including area, length, elongation, main direction, and roundness of objects/segments in ENVI software (under the “Example Based Feature Extraction Workflow” toolbox). MPB attack phases were classified separately after masking lodgepole pine to avoid having a lot of classes in the initial classification, which could have reduced accuracy.

Field data and visual identification were used to select two datasets for training and testing of within GEOBIA shape classification. Tree species included lodgepole pine, subalpine fir, white spruce, and black spruce. During field data collection, MPB phases were observed for each tree, including healthy conifers and dead conifers with or without needles. Then, the proportion of tree mortality within each plot was calculated to represent overall mortality patterns. Dead or partially dead lodgepole pine and coarse woody debris were easily identified visually and confirmed using field-based tree locations. Field data were used to identify white spruce, black spruce and subalpine fir observed in plots. Visible coarse woody debris were identified visually in each plot.

As explained in the previous section, high-resolution imagery (20 megapixels) was used to segment the RPAS imagery in ENVI software under the "Example-Based Feature Extraction Workflow" toolbox. All 12 derived raster layers (Figure 2.3) were used to train and apply the SVM classifier in ENVI software. The Radial Basis Function was selected as the kernel type for training the classifier, since it is highly effective for handling non-linear relationships and complicated classifications of high spatial resolution imagery (Serbouti et al., 2021; Fowler, 2000). The Radial Basis Function kernel is commonly used in SVM classification to handle and classify input features with non-linear relationships. It projects the input attributes/metrics to a higher-dimensional space to allow the SVM to find a linear relationship between classes that are non-linear in the original input feature. This helps SVM classify and handle complex data non-linear patterns and relationship in the input attributes (Mansor *et al.*, 2024).

The Gamma in the kernel function was set as 0.3 with the penalty parameter of 300. These moderate values selected to avoid underfitting and overfitting. Typically, low gamma values (for example, 0.01) make the model simple and result in underfitting while high gamma values (for example, 5) make the model complex and lead to overfitting. Similarly, the penalty parameter was set at a moderate level to avoid these challenges. These values were identified by trial and error during the GEOBIA workflow, but they are supported by a literature review (Nitze, I., Schulthess, U., & Asche, 2012). Additionally, after mapping tree species and CWD in each plot, canopy and

CWD coverage were calculated using the Calculate Geometry tool in GIS software. To do this, all tree species and CWD boundaries were filtered separately from the results of GEOBIA, then their areas were calculated using the Calculate Geometry tool. Afterwards, considering the total area of each plot (400 m^2), the canopy and CWD coverage were calculated.

Given that the majority of lodgepole pine trees in the study area were impacted by MPB, GEOBIA and SVM workflow was repeated (focusing on just lodgepole pine class) to identify their conditions (green, red and gray) on a per plot basis. These condition classes were not included in the initial classification to avoid having many classes, as this can be challenging for identifying optimal inputs for the segmentation method and achieving a balance between over-segmentation and under-segmentation. Additionally, more classes may decrease the accuracy of the classification. The objective of this classification was to classify lodgepole pine conditions to estimate biomass for trees with different fuel weights based on allometry described in Section 2.4. To perform the lodgepole pine phase classification, all bands described in the previous sections and Figure 2.3 were used, and all classes except lodgepole pine trees were masked. Field data along with visual assessment were then used to prepare two datasets: training and test data. The training data was used with the exact same workflow described for the initial classification and apply the SVM classifier to classify all lodgepole pine trees into green, red, and grey phases in ENVI software.

4.2.3 Testing and Accuracy Evaluation

A confusion matrix (or error matrix), was employed to evaluate the accuracy of the GEOBIA and SVM, utilizing Overall, User’s and Produce’s Accuracy, and the Kappa coefficient. To do this, validation data (shapefiles) for accuracy assessment were derived from field data and visual interpretation of high-resolution RGB imagery. CWD and lodgepole pine trees (mostly dead or partially dead) were simply detected by visual interpretation of high spatial resolution RGB imagery. Furthermore, green lodgepole pine, subalpine fir, and spruce trees were identified using field measurements and visual interpretation. Overall Accuracy and Kappa coefficient were computed using the shape file of the validation data for those randomly identified features (individual trees, coarse woody debris, etc.). The Kappa coefficient was included alongside Overall Accuracy to indicate the reliability and robustness of the classification. It reflects the likelihood that the observed classification accuracy occurred by chance or random coincidence. Additionally, a feature-based validation was also used to assess the accuracy of GEOBIA to better understand the limitations of RPAS multispectral data for classifying features affected by canopy occlusion. To do this, GEOBIA results were extracted using the tree centre coordinates. Tree centres, which were calculated from point clouds after individual tree detection (described in Chapter 5). These were also compared using a confusion matrix. Table 4.1 provides a sample of a confusion matrix with equations of Overall Accuracy, User's Accuracy and Producer's Accuracy (Equations 4-6) (Congalton, 1991). Although Overall Accuracy and the Kappa coefficient were emphasized in the main results section as general indicators for all classes (tree species and CWD), User’s and Produce’s Accuracy were also used to evaluate the performance of the classification for individual classes, such as CWD, and to examine commission and omission errors.

Table 4.1, A sample of Confusion Matrix.

		Classified as			
		Class 1	Class 2	Class 3	User's Accuracy
Actual (Ground-truth data)	Class 1	A	B	C	$\frac{\mathrm{A}}{\mathrm{A+B+C}}$
	Class 2	D	E	F	$\frac{\mathrm{E}}{\mathrm{D+E+F}}$
	Class 3	G	H	I	$\frac{\mathrm{I}}{\mathrm{G+H+I}}$
	Producer's Accuracy	$\frac{\mathrm{A}}{\mathrm{A+D+G}}$	$\frac{\mathrm{E}}{\mathrm{B+E+H}}$	$\frac{\mathrm{I}}{\mathrm{C+F+I}}$	

$$\text{Overall Accuracy} = \frac{\text{Correctly Classified Samples}}{\text{Total Samples}} = \frac{\mathrm{A+E+I}}{\mathrm{A+B+C+D+E+F+G+H+I}} \quad (4)$$

$$\text{User Accuracy} = \frac{\text{Correctly Classified Samples in class 1}}{\text{Total Samples as Class 1}} = \frac{\mathrm{A}}{\mathrm{A+B+C}} \quad (5)$$

$$\text{Producer Accuracy} = \frac{\text{Correctly Classified Samples in class 1}}{\text{Total Samples for Class 1}} = \frac{\mathrm{A}}{\mathrm{A+D+G}} \quad (6)$$

4.3 Results

4.3.1 Atmospheric and Shadow Conditions in RPAS Imagery for 2021 and 2022

Plots 1-12 were collected during smoky atmospheric conditions (summer of 2021) from relatively open canopies with minimal shadows. Therefore, GEOBIA for these plots was considerably better than for plots 13-16 collected during less smoky conditions, summer 2022, thereby reducing understory and ground occlusion. Plots collected in the summer of 2022 have high shadow conditions (Plots 13 and 14) and very closed canopy with high density of laser pulse returns, which were challenging for all GEOBIA steps and decreased the accuracy. Figure 4.1 a and b shows two samples of shadow condition in the summer 2021 and the summer 2022, respectively.

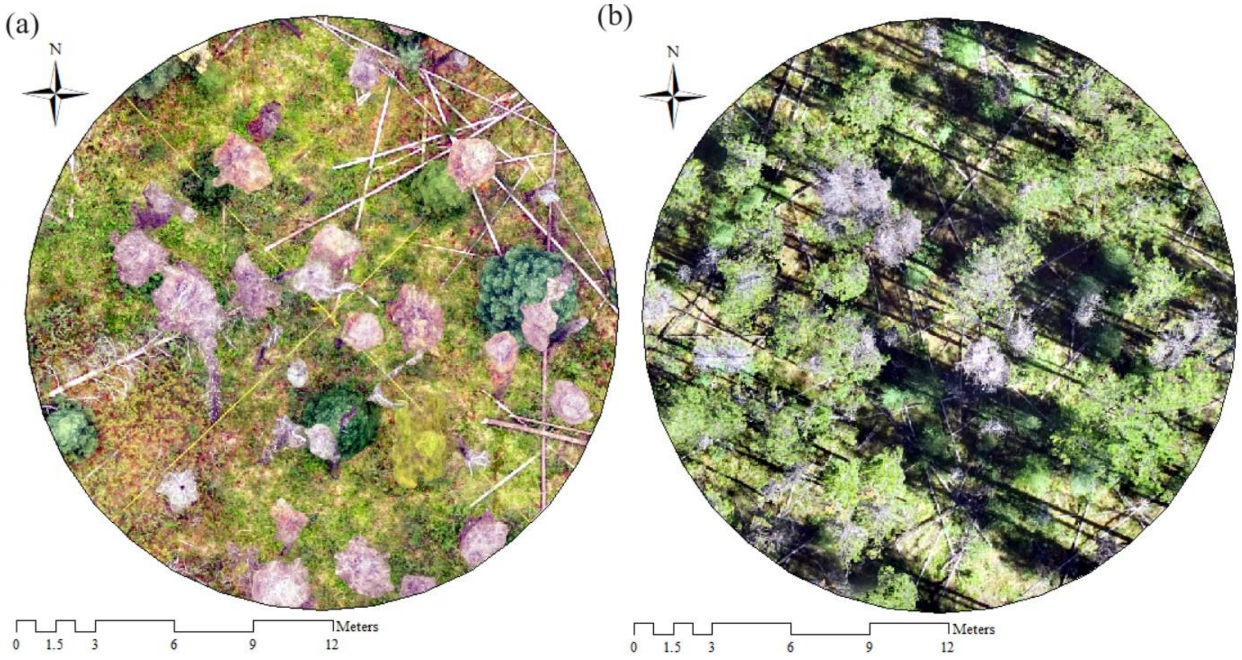

Figure 4.1, Comparison of shadow conditions in RPAS imagery from summer 2021 and summer 2022; (a) Plot 12 with minimal shadow condition and open canopies collected in the summer 2021; (b) Plot13 with high level of shadow collected in the summer 2022.

4.3.2 Classification of Coarse Woody Debris

Figure 4.2 shows the results of GEOBIA segmentation of features with SVM classification. Trial and error was used to determine an appropriate balance between over- and under-segmentation in Edge and Full Lambda Schedule parameters, resulting in 16-22% and 90-98%, for individual tree canopy extent and coarse woody debris, respectively. GEOBIA was highly effective for mapping visible CWD in open canopies (e.g. Plots 11 and 12 (Producer accuracy = ~99%)). However, mapping visible coarse woody debris in closed canopies with high occlusion using passive RPAS imagery (e.g., Plots 15 and 16 (Producer accuracy = ~71%)) was challenging. The condition of CWD (e.g. sound vs. rotten) is another factor that could affect the accuracy. For example, coarse woody debris in plots 7 and 8 had ~80% producer accuracy due to having some rotten coarse woody debris. Table 4.2 shows the producer and user accuracy for 16 plots.

Table 4.2, Validation of GEOBIA results for mapping coarse woody debris.

Plot	Plots 1&2	Plots 3&4	Plots 5&6	Plots 7&8	Plots 9&10	Plots 11&12	Plots 13&14	Plots 15&16
Producer Accuracy (%)	98	91	95	81	97	99	91	71
User Accuracy (%)	99	100	95	75	85	98	55	83

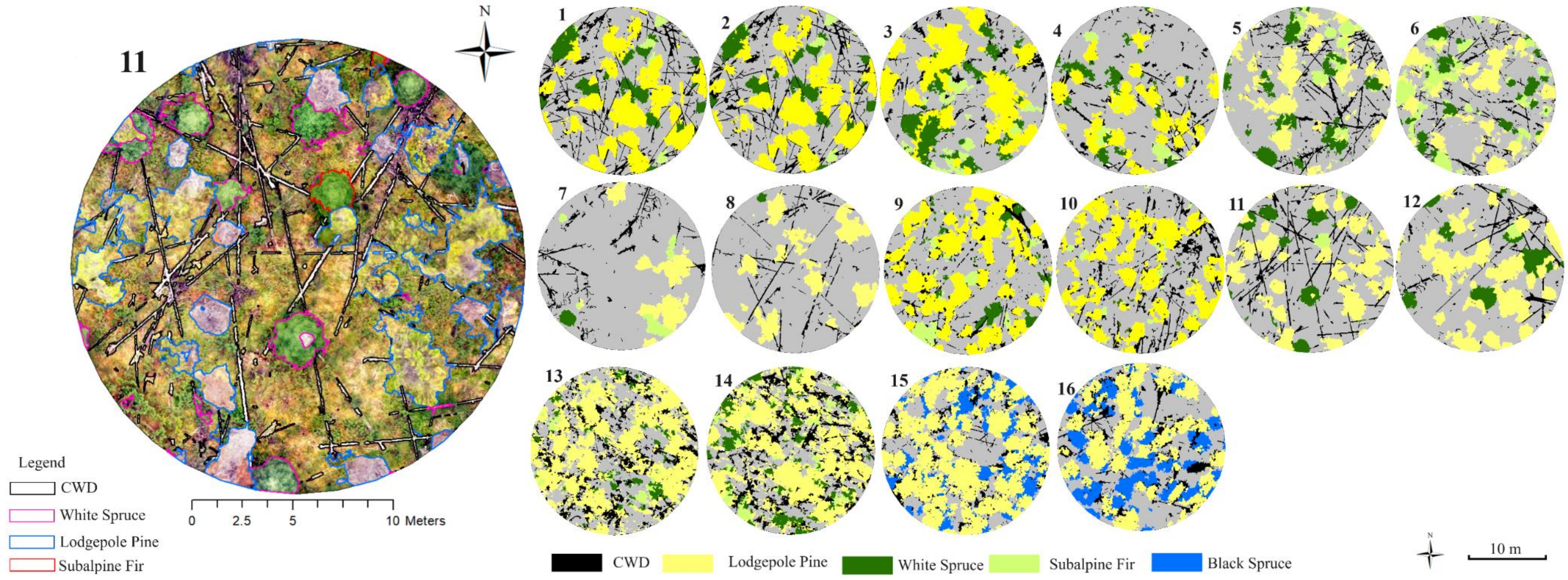

Figure 4.2, The results of GEOBIA workflow for identifying tree species and mapping visible coarse woody debris.

4.3.3 Species classification

Lodgepole pine had better accuracy (average producer accuracy = ~96%) as most lodgepole pine trees in plots 1-13 were infested by MPB and were dead or half dead with spectral responses that were distinguishable from other healthy and green conifers. However, GEOBIA was less accurate for identifying white spruce (average producer accuracy = ~90%), black spruce (average producer accuracy = ~78%), and subalpine fir (average producer accuracy = ~77%) compared to lodgepole pine trees. All in all, the average producer accuracy for mapping lodgepole pine, coarse woody debris, and other conifers were 96%, 90%, and 83%, respectively. Table 4.2 (a, b, and c) presents the average producer, user, and overall accuracy of tree species classes and coarse woody debris as well as the Kappa coefficient for eight RPAS polygons containing 16 plots using the confusion matrix. Tree mortality did not influence the accuracy GEOBIA as most dead or dying trees were lodgepole pine. For example, the Overall Accuracy for higher mortality plots: 11 (59% mortality) and 12 (84% mortality) is 95.6%, while the Overall Accuracy for lower mortality plots: 15 (18% mortality) and 16 (33% mortality) is 93.9% which is similar to those with high tree mortality.

High tree density and shadows (or shadow proportion) can decrease GEOBIA accuracy (Tables 4.3, 4.4 and 4.5). For instance, RPAS polygons from closed canopies: plots 13 and 14 which also have a high proportion of shadows has an Overall Accuracy of 80.2% and Kappa coefficient of 0.60. In contrast, an RPAS polygon including open canopies with the least shadow proportion (plots 11 and 12) have a high Overall Accuracy of 95.6% and a Kappa coefficient = 0.93.

Table 4.3, A pixel-based validation of GEOBIA results based on tree mortality.

		Low Tree Mortality (12%)		→		**High Tree Mortality (88%)**	
Plots 15 & 16	Plots 13 & 14	Plots 5 & 6	Plots 9 & 10	Plots 1 & 2	Plots 7 & 8	Plots 11 & 12	Plots 3 & 4
Avg. Producer Accuracy (%)							
82.2	79.1	87.7	94.0	96.4	91.7	93.8	82.3
Avg. User Accuracy (%)							
92.4	70.2	89.1	93.4	95.3	89.6	96.1	93.4
Overall Accuracy (%)							
93.9	80.2	88.3	96.7	98.2	82.6	95.6	84.7
Kappa Coefficient							
0.90	0.60	0.84	0.93	0.96	0.79	0.93	0.75

Table 4.4, A pixel-based validation of GEOBIA results based on tree density.

		Low Tree Density (14 Trees)		→		**High Tree Density (128 Trees)**	
Plots 7 & 8	Plots 3 & 4	Plots 11 & 12	Plots 1 & 2	Plots 5 & 6	Plots 9 & 10	Plots 13 & 14	Plots 15 & 16
Avg. Producer Accuracy (%)							
91.4	82.3	93.8	96.4	87.7	94.0	79.1	87.2
Avg. User Accuracy (%)							
89.6	93.4	96.1	95.3	89.1	93.4	70.2	93.4
Overall Accuracy (%)							
82.6	84.7	95.6	98.2	88.3	96.7	80.2	93.9
Kappa Coefficient							
0.79	0.75	0.93	0.96	0.84	0.93	0.60	0.89

Table 4.5, A pixel-based validation of GEOBIA results based on shadow conditions.

			Low Shadow Condition		→		**High Shadow Condition**
Plots 11 & 12	Plots 9 & 10	Plots 1 & 2	Plots 5 & 6	Plots 7 & 8	Plots 3 & 4	Plots 15 & 16	Plots 13 & 14
Avg. Producer Accuracy (%)							
93.8	94.0	96.4	87.7	91.4	82.3	82.2	79.1
Avg. User Accuracy (%)							
96.1	93.4	95.3	89.1	89.6	93.4	92.4	70.2
Overall Accuracy (%)							
95.6	96.7	98.2	88.3	82.6	84.7	93.9	80.2
Kappa Coefficient							
0.93	0.93	0.96	0.84	0.79	0.75	0.89	0.60

Table 4.6 presents the pixel-based confusion matrix for Plots 1 and 2 (corresponding to RPAS Polygon 1) as a sample, including all accuracy metrics such as overall accuracy, user's and producer's accuracy, and the Kappa coefficient. The confusion matrices for Plots 3–16 (within seven RPAS polygons) are presented in the Appendix 3.

Table 4.6, Confusion matrix for Plots 1 and 2 (RPAS Polygon 1).

Class	CWD	Lodgepole pine	White Spruce	Subalpine Fir	Total	User's Accuracy
CWD	14251	21	0	0	14272	99.85
Lodgepole pine	194	75246	0	0	75440	99.74
White Spruce	0	20	7739	1430	9189	84.22
Subalpine Fir	40	0	424	17058	17522	97.35
Total	14485	75287	8163	18488	116423	
Producer's Accuracy	98.38	99.95	94.81	92.27		
			Overall Accuracy	98.17		
			Kappa Coefficient	0.96		

Table 4.7 displays two feature-based confusion matrices for data collected in the summers of 2021 (relatively open canopies with less shadow) and 2022 (dense or high shadow) based on field/RPAS matched trees. The Overall Accuracy for the 2021 data was 84% and for the data collected in 2022 was 75% with higher accuracy in 2021 compared to 2022 due to open canopies and less canopy occlusion. The main reasons for lower accuracy for RPAS 2022 than 2021 were canopy occlusion (because of closed and dense canopy cover in 2022 and more detailed and denser point clouds from the L1 sensor) and shadow conditions which were in the previous sections.

Table 4.7, Feature-based validation using two confusion matrices, a) RPAS data collected in the summer 2021, b) RPAS data collected in the summer 2022.

		Classified Species			
	(a)	Lodgepole Pine	Subalpine Fir	White Spruce	Non-Tree
Ground-Truth	Lodgepole Pine	217	2	8	7
	Subalpine Fir	5	28	13	5
	White Spruce	1	4	15	3
	Non-Tree	0	0	0	0
		Overall Accuracy =			84%

		Classified Species				
	(b)	Lodgepole Pine	Subalpine Fir	White Spruce	Black Spruce	Non-Tree
Ground-Truth Data	Lodgepole Pine	85	1	1	1	7
	Subalpine Fir	6	7	5	0	1
	White Spruce	2	0	3	0	4
	Black Spruce	13	0	0	32	2
	Non-Tree	0	0	0	0	0
				Overall Accuracy=		75%

4.3.4 MPB phase classification

The average Overall Accuracy for the classifications of lodgepole pine conditions including green, red, and gray was also approximately ~75%. Plots (1 and 2) and (11 and 12) have the highest accuracy (86%) and the average tree mortality of 68%, however, plots 13 and 14 have the lowest accuracy (66%) and the average tree mortality of 43%. Table 4.4 shows the Overall Accuracy of these classifications of lodgepole pine conditions in the 16 plots with their mortality.

Table 4.8, The feature-based confusion matrix for assessing the accuracy of GEOBIA for MPB attack phase classification

		Classified MPB Phases			
		Green	Red	Gray	Unclassified
Ground-Truth Data	Green	48	3	2	1
	Red	2	26	8	0
	Gray	1	13	40	4
	Unclassified	0	0	0	0
		Overall Accuracy =			77%

Table 4.9, Validation of lodgepole pine conditions classifications in 16 plots based on tree mortality.

Plot	15&16	5&6	13&14	9&10	1&2	7&8	11&12	3&4
Overall Accuracy (%)	68	70	66	76	86	76	86	67
Tree Mortality (%)	25.5	37.5	43	56	64.5	71	71.5	74

4.3.5 Canopy Cover and Coarse Woody Debris Distribution

Table 4.9 shows the canopy and coarse woody debris coverage in square meters and percentage per plot for 16 plots. It was found that the plots with high tree mortality have less canopy coverage (for example, plot 12, 33%) than unaffected plots (plot 15, 60.7%). Despite the overestimation in plots 13-14, almost all plots have the same coarse woody debris coverage (~7% in average). This is because coarse woody debris accumulation increases over decades following infestation (old stage of MPB outbreaks) and dead conifers can remain standing as snags for a long period of time (Jenkins *et al.*, 2014).

Table 4.10, Canopy and Coarse woody debris coverage in square meters and percentage per plot for 16 plots.

Plot	15	14	6	16	5	10	13	9	11	1	8	2	3	7	4	12
Tree Mortality (%)	12	23	38	24	39	54	38	57	50	50	64	59	67	73	79	88
CWD Coverage (m^2)	29	55	16	35	23	33	50	23	28	39	15	33	16	16	19	18
CWD Percent (%)	7.3	13.8	4	8.8	5.8	8.3	12.5	5.8	7	9.8	3.8	8.3	4	4	4.8	4.5
Canopy Coverage (m^2)	243	206	137	198	118	120	189	164	112	86	61	146	172	50	96	132
Canopy Coverage (%)	60.7	51.5	34.2	49.5	29.5	30	47.2	41	28	21.5	15.2	36.5	43	12.5	24	33

4.4 Summary

In this chapter, it was found that GEOBIA along with RPAS multispectral imagery and structural information from lidar and photogrammetric point clouds, can be used for identifying tree species and their conditions and mapping visible forest structures such as coarse woody debris respectively. Shadow and canopy occlusion are two main limitations for this workflow.

Chapter 5. 3D Fuel Attributes and Volumetric Quantification of Tree and Fuel Characteristics

5.1 Introduction

This chapter discusses 3D fuel modeling using photogrammetric and lidar point clouds. The overall objective of this chapter was to explore methodologies for measuring/estimating common canopy fuel using RPAS point clouds and then assess shift of vertical fuel to the forest floor due to MPB outbreaks and tree mortality. A point-based classification method was developed to classify stem and foliage points using RPAS point clouds. The purpose of this classification was to identify canopy base height using the region-based method as well as calculate foliage volume. Afterwards, tree height and diameter at breast height were measured/estimated. Using all variables and the results from the previous section (tree species) canopy fuel load and canopy bulk density were estimated using allometric equations. Finally, the vertical vegetation profile and volume of foliage are utilized to assess fuel distribution.

5.2 Methods

5.2.1 Above-Ground and Ground Point Separation, Stem and Foliage Classification

The overall approach of this chapter was to quantify above-ground canopy fuels across different tree mortality by classification and analyzing tree structures using RPAS photogrammetric and lidar point clouds. This was achieved by separating above-ground biomass from ground and short vegetation, classifying trees into stem and foliage points, detecting individual trees, and measuring or estimating key forest fuel metrics including tree height, diameter at breast height, canopy base height, canopy fuel load and canopy bulk density.

The quantification of canopy/above-ground fuels available to burn in different MPB phases of mortality first requires the separation of overstory data (in this case, points) and excluding ground and short vegetation to work on trees. To do this, after completing georegistration, the Cloth Simulation Filter (in CloudCompare software) was used to segment above ground biomass from ground biomass points (Zhang *et al.*, 2016). All advanced parameters for Cloth Simulation Filter were considered as described in (Zhang et al., 2016), except the classification threshold (Cloth resolution (size of the grid for the simulated cloth) =2 metres and max iterations (number of iterations) =500). The classification threshold which represents the distance between each point and the simulated terrain was considered in the range of 0.50 to 0.70 metres, depending on the height of short vegetation such as grass, seedling, and shrub at the plot floor.

Following ground points removal, above ground biomass points were classified into foliage and stem points using SVM learning (in MATLAB, Appendix 1) to calculate tree metrics such as foliage volume, and canopy base height, which are essential for fuel quantification and then important for fire behavior modeling. To do individual point-based classification, various geometric features: 3rd Eigenvalue, Verticality, Sphericity, Surface Variation, Normal Change Rate, Anisotropy and Principal Component Analysis (PCA) 1 (Atik et al., 2021; Cabo et al., 2019; Becker et al., 2018; Weinmann et al., 2015) were calculated in CloudCompare (using the "Compute Geometric Features" toolbox) as attributes to classify RPAS point clouds, illustrated within the overall graphical workflow in Figure 5.1 a and b.

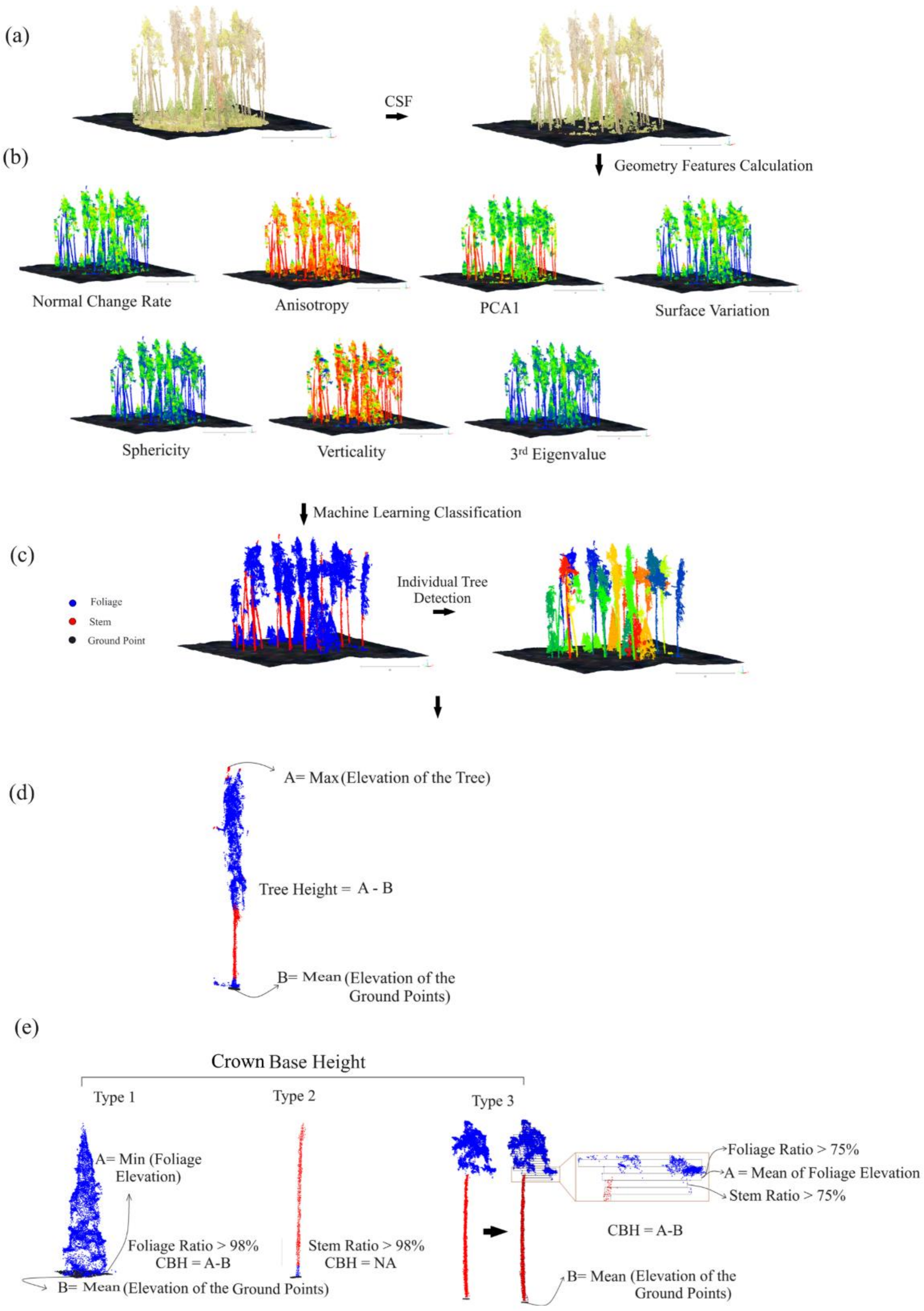

Figure 5.1, The graphical flowchart of the point cloud processing workflow (for plot 11 as an example): a) segmentation of above-ground biomass from ground biomass points, b) calculation of geometric features, c) classification of stem and foliage points along with individual tree detection, d) estimation (SfM)/measurement (RPAS lidar) of tree height, and e) estimate of crown base height. (CSF: Cloth Simulation Filter; PCA: Principal Component Analysis; CBH: Crown Base Height)

SVM classifiers were trained using approximately 4.6 million points (2.9 million from RPAS lidar and 1.7 million from photogrammetric point clouds) which were manually selected from various locations within the RPAS polygons and manually classified into stem and foliage categories using CloudCompare software (using the "Segment" toolbox). Then, SVM was trained and saved for RPAS lidar and photogrammetric point clouds to classify RPAS point clouds. Figure 5.2 illustrates the original and classified training data for RPAS lidar and photogrammetric point cloud classifications.

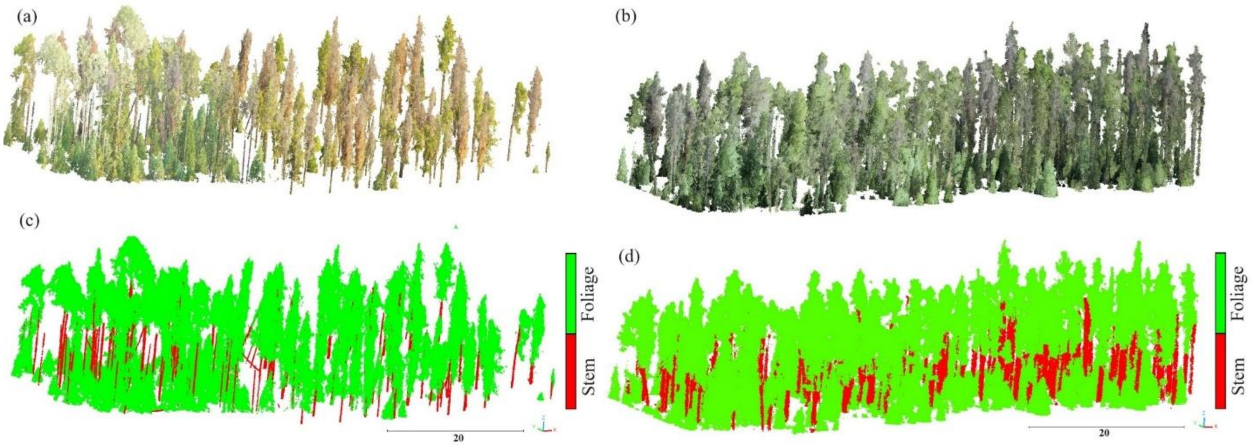

Figure 5.2, (a) Training data for Support Vector Machine classification of above-ground biomass photogrammetric point clouds in RGB colour; (b) Training data for Support Vector Machine classification of above-ground biomass lidar point clouds in RGB colour; (c) Classification of the photogrammetric training point cloud into stem and foliage points; (d) Classification of the lidar training point cloud into stem and foliage points.

5.2.2 Individual Tree Detection

Following the classification of stem and foliage, TreeIso was used to identify individual trees in CloudCompare (Xi and Hopkinson, 2022), illustrated in Figure 5.1c. The TreeIso process involves two stages of 3D and 2D cut-pursuit clustering, followed by a final stage of global refinements. In this case, all parameters were configured according to Xi and Hopkinson, (2022) using the default settings of CloudCompare software. The number of nearest points determined by the user (k) was set 4 for 3D clustering and 5 for 2D clustering.

Since TreeIso is a method for individual tree detection for terrestrial laser scanning point clouds (with minimum gaps), it may struggle to identify individual trees in closed and complex canopies or interacting RPAS point clouds within overlapping canopies. In these cases, TreeIso may mis-identify two trees as one especially when applied to RPAS lidar point clouds within dense forest areas with overlapping tree stems/canopies. To address this issue, a Density-Based Spatial Clustering of Applications with Noise (DBSCAN) technique in MATLAB (Appendix 1) was also performed to improve the results of TreeIso (Comesaña-Cebral et al., 2021; Ester et al., 1996) reducing misidentifications and rectifying them. To do this, the minimum number of points in each cluster was set to 20 with a distance threshold of 0.50 m.

5.2.3 Methods for determining tree metrics required for quantifying fuels

Tree height was determined on a per-tree basis by subtracting the maximum height of individual tree points from the average interpolated airborne lidar ground elevation (Hopkinson *et al.*, 2004). First, the point density of airborne lidar ground points was increased/resampled to 200 points per square meter as there is a need to have at least one point directly under the tree. To do this, a mesh was fitted to the ground points of airborne lidar using the 'Mesh' tool in CloudCompare. Then, using the 'Point Sampling on the Mesh' tool in CloudCompare, the point density of the airborne lidar was increased to 200 points per square meter. Subsequently, airborne lidar points near each tree were considered within a small area (30 cm x 30 cm) directly under the maximum height of each individual tree (Figure 5.1d).

To assess how above ground biomass shifts to the forest floor based on the different tree mortality conditions, foliage volume was calculated using classified foliage points and compared across plots with different tree mortality. Vertical vegetation profiles were used to do the comparison by estimating foliage volume at 0.5 meter intervals. Delaunay triangulation (Lawson, 1977) and Convex Hull (Anderson, 1978) are common methods used to calculate the volume of a 3D point cloud. Here, Delaunay triangulation was applied to the classified foliage points of all points in each interval to reconstruct the 3D surface envelope of canopy foliage and branches. Then, the Convex Hull was used to estimate the approximate volume of foliage (Appendix 1).

As one of the important/challenging fire fuel parameters, a novel workflow was developed to directly estimate canopy base height from individual tree points, illustrated graphically in Figure 5.1e. In this case, three tree structure types were considered: trees with almost all stem points as a snag (e.g. dead, no/few broken branches), trees with all or most foliage points, and lastly, those containing both stem and foliage, where the canopy base height is above the ground. For each structure type, the ratio of stem and foliage points was determined. If the ratio of stem points was more than 98% (deducting 2% to decrease the impact of misclassification and noise), the tree was classified as a snag and therefore does not have a canopy nor a canopy base height. Conversely, a foliage ratio of more than 98% indicates that the tree has a canopy that extends almost to the ground, and therefore, has a short canopy base height, with the assumption that the minimum elevation of foliage considered as canopy base height is the same as the ground elevation.

Region-based methods were then used if the stem to foliage ratio was between these two (snag vs. foliage to ground) (Figure 5.1e). Two Regions of Interest (ROI) with 0.50 m height were moved via a moving window approach from the base of tree to the top consecutively. The lower ROI checked the ratio of stem points while the upper ROI checked the ratio of foliage. If both

ROIs had a ratio of more than 75%, the average height of foliage above ground level in the upper ROI was considered as the above ground canopy base height elevation. These criteria (0.5 m ROI height and 75% threshold) were determined through trial and error, and the results were not highly sensitive to small variations (+/-10%) in these parameters. Afterwards, canopy base height was calculated from the subtraction of canopy base elevation from average ground elevation (Figure 5.1e). Theoretically, all foliage and stem point ratios in this workflow should be 100%. However, these are rarely achievable in the real world due to misclassification and noise in the data. Additionally, in the case of lidar point clouds, there are still stem points within the tree crowns (due to penetration). Therefore, multiple ranging from 50% to 100% were checked, and a ratio of 75% was found to provide an optimal balance to avoid having overestimation and underestimation of measuring the canopy base height. All steps of this workflow were implemented in MATLAB and the script can be found in the appendix 1.

Measuring diameter at breast height directly using stem points are challenging due to the presence of noise around tree stems and the lack of sufficient points for trees with small diameter at breast height. Therefore, given the strong correlation between tree height and diameter at breast height, a simple linear regression was used to estimate diameter at breast height (Kutner et al., 1983). In this case, 75% of the data were randomly selected for developing a linear regression model (using Microsoft Excel software), and the remaining 25% were used for accuracy assessment using the correlation coefficient (R^2) and RMSE. Crown/Canopy fuel load was calculated using allometry (Equations 1 and 2) using RPAS GEOBIA classification of tree species and condition (with misclassifications removed), RPAS-derived tree height and diameter at breast height based on foliage only (healthy); foliage and branches (dead conifer with needles); and branches only (dead conifer without needles). Canopy bulk density was calculated using the

Equation 7, where canopy fuel load represents the total amount of canopy fuel load in each plot, stand height represents the average of tree height and canopy base height represents the average of canopy base height in each plot.

$$\text{Canopy Bulk Density}\left(\frac{\text{kg}}{\text{m}^3}\right)=\frac{\text{Canopy Fuel Load}\left(\frac{\text{kg}}{\text{m}^2}\right)}{\text{Stand Height (m)}-\text{Canopy Base Height (m)}} \quad (7)$$

Plot-level vertical vegetation profiles are an effective method for assessing the distribution of fuels vertically within the plot (Skowronski et al., 2020; Pimont et al., 2016; Simard et al., 2011). Vertical vegetation profiles were used to better understand the shift of fuels to the forest floor based on the proportion of tree mortality mostly associated with MPB attack phases compared with generally healthy, mixed stands. Delaunay triangulation was used to create the object of foliage points above the canopy base height at 0.50 m increments for each tree, then, convex hull was used to calculate the volume of foliage. All steps of this were implemented in MATLAB and the script can be found in Appendix 1.

5.2.4 Testing and Accuracy Evaluation

More than 500 individual trees were matched with field measurements in 16 plots based on their location in quadrants (NW, NE, SW, and SE), tree height, and canopy base height. Fuel attributes of individual trees (tree height, crown base height, and crown fuel load) were validated per tree and varied based on tree condition including healthy conifers, dead lodgepole pine with red needles, and dead lodgepole pine with no needles, assuming these died as a result of MPB infestation. The validation and accuracy assessment of tree height, canopy base height, and canopy fuel load within utilized performance indicators such as Mean Absolute Error (MAE), RMSE, Normalized Root Mean Square Error (NRMSE), and correlation coefficient (R^2) (Equations 8-12).

$$\mathrm{RMSE} = \sqrt{\sum_{k=1}^{n} \frac{(y'_k - y_k)^2}{n}} \tag{8}$$

$$\mathrm{MAE} = \sum_{k=1}^{n} \frac{|y'_k - y_k|}{n} \tag{9}$$

$$\mathrm{NRMSE} = \frac{\mathrm{RMSE}}{\max(y_k) - \min(y_k)} \tag{10}$$

$$R^2 = 1 - \frac{\sum_{k=1}^{n} (y'_k - y_k)^2}{\sum_{k=1}^{n} (y'_k - \bar{y})^2} \tag{11}$$

$$\mathrm{BIAS} = \sum_{k=1}^{n} \frac{(y'_k - y_k)}{n} \tag{12}$$

Where y'_k represents measured/estimated fire fuel values, y_k represents field measurements and n is the number of trees that used for validation, $\bar{y}$ is also the mean for field data.

5.3 Results

5.3.1 General characteristics of structure extraction within plots

Figure 5.3 shows visual representations of all plots after applying the Cloth Simulation Filter and Support Vector Machine learning, classifying point clouds into ground biomass, stems, and foliage. The variations in plot characteristics are shown, including variable tree density (lowest density = plot 7, number of trees = 14; highest plot density = plot 15 number of trees = 128), tree mortality (lowest mortality = plot 15, 12%; highest tree mortality = plot 12, 88%), tree height (shortest trees = plot 15, 1.3 m; tallest trees = plot 15, 33.4 m), and seedling/sapling density (lowest seedling/sapling density found in plot 12, number of seedlings/saplings = 0; highest density found in plot 14, number of seedling/sapling = 46). Lidar point clouds provided high point densities (1.3 - 1.8 million points per plot (400 m^2)) and more detail than photogrammetric point clouds (0.40 - 1 million points per plot).

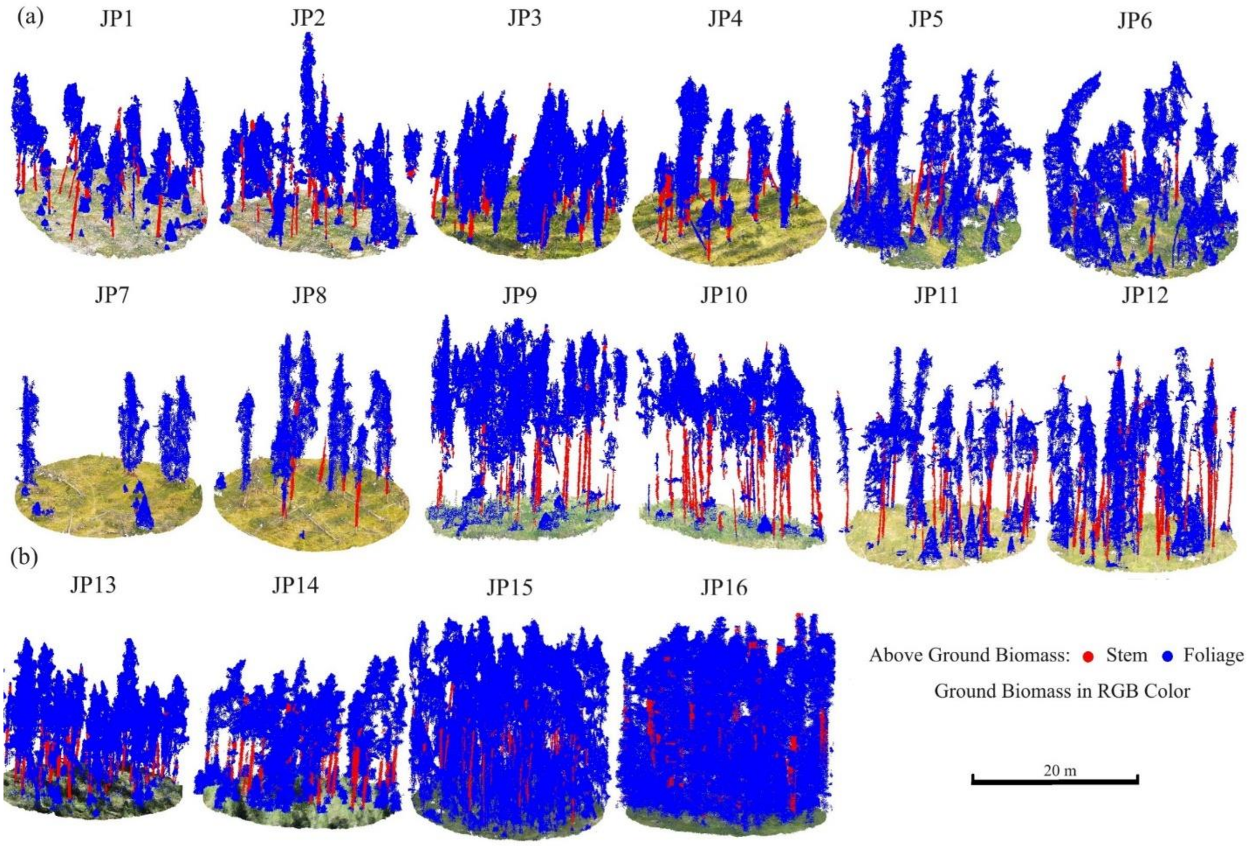

Figure 5.3, The visual representation of 16 plots including ground biomass (in RGB colour) and classified above ground biomass into stem and foliage, a) photogrammetric point clouds (Plots 1-12), b) lidar point clouds (Plots 13-16).

Plots 9 and 10 (Figure 5.3 contain tall, dense trees with greater canopy occlusion. In plots containing a high number of short vegetation (e.g., seedlings and shrubs) (e.g., plots 5, 6, 14, 15, and 16), identification of stems and foliage using geometric features was challenging, given that geometric features are calculated based on neighboring points. However, in plots 10, 11, and 12, stems and foliage points were more distinguishable due to higher canopy base height and fewer small trees and shrubs. Additionally, high tree densities in plots 13 to 16 resulted in misclassification of some individual trees using TreeIso, where two trees that were close together were identified as one.

5.3.2 Comparison of RPAS-derived fuel metrics with field measurements

Vegetation fuel attributes, including tree height, crown base height and crown fuel load were derived using photogrammetric and lidar systems, as these are important fuel metrics for understanding the distribution of fuel and modeling fire behaviour. Figure 5.4 illustrates R^2, RMSE, NRMSE and BIAS calculated for tree height and crown base height using photogrammetric and lidar technologies compared with 472 field measurements of trees based on tree condition/mortality. The results indicate high accuracy estimating (using photogrammetric) and measuring (lidar) both tree height (Figure 5.4 a, b) and canopy base height (Figure 5.4 c, d) across all tree conditions. Generally, lidar point clouds have better accuracy than photogrammetric point clouds despite collection from plots with higher density of trees and closed canopies. This is because lidar can penetrate through the canopy whereas photogrammetric methods based on structure from motion are impacted by canopy occlusion. Lidar point clouds have the highest accuracy when used for height of green/healthy conifers (R^2= 0.99, RMSE = 0.59 m, and NRMSE = 2.81%) compared with measured. Lowest accuracy of tree heights was found for dead conifers with no needles using photogrammetric point clouds (R2= 0.92, RMSE= 1.53 m, and NRMSE= 4.08%). Tree height using both lidar and photogrammetric systems is relatively high (R^2 ranging from 0.75-0.91), crown base height is over-estimated using photogrammetric methods. Crown base height accuracy for dead conifers with no needles (R^2= 0.80, RMSE= 1.86 m, and NRMSE= 13.48%) was higher than for healthy conifers (R^2= 0.78, RMSE= 2.40 m, and NRMSE= 18.19%)

and dead conifers with red needles (R^2= 0.76, RMSE= 2.29 m, and NRMSE= 16.63%) due to reduced canopy occlusion. In contrast to the photogrammetric system, lidar can penetrate the canopy and collect information under canopy cover to more accurately measure crown base height regardless of tree mortality and density. Therefore, the results from lidar are similar across phases, regardless of stem density and canopy closure.

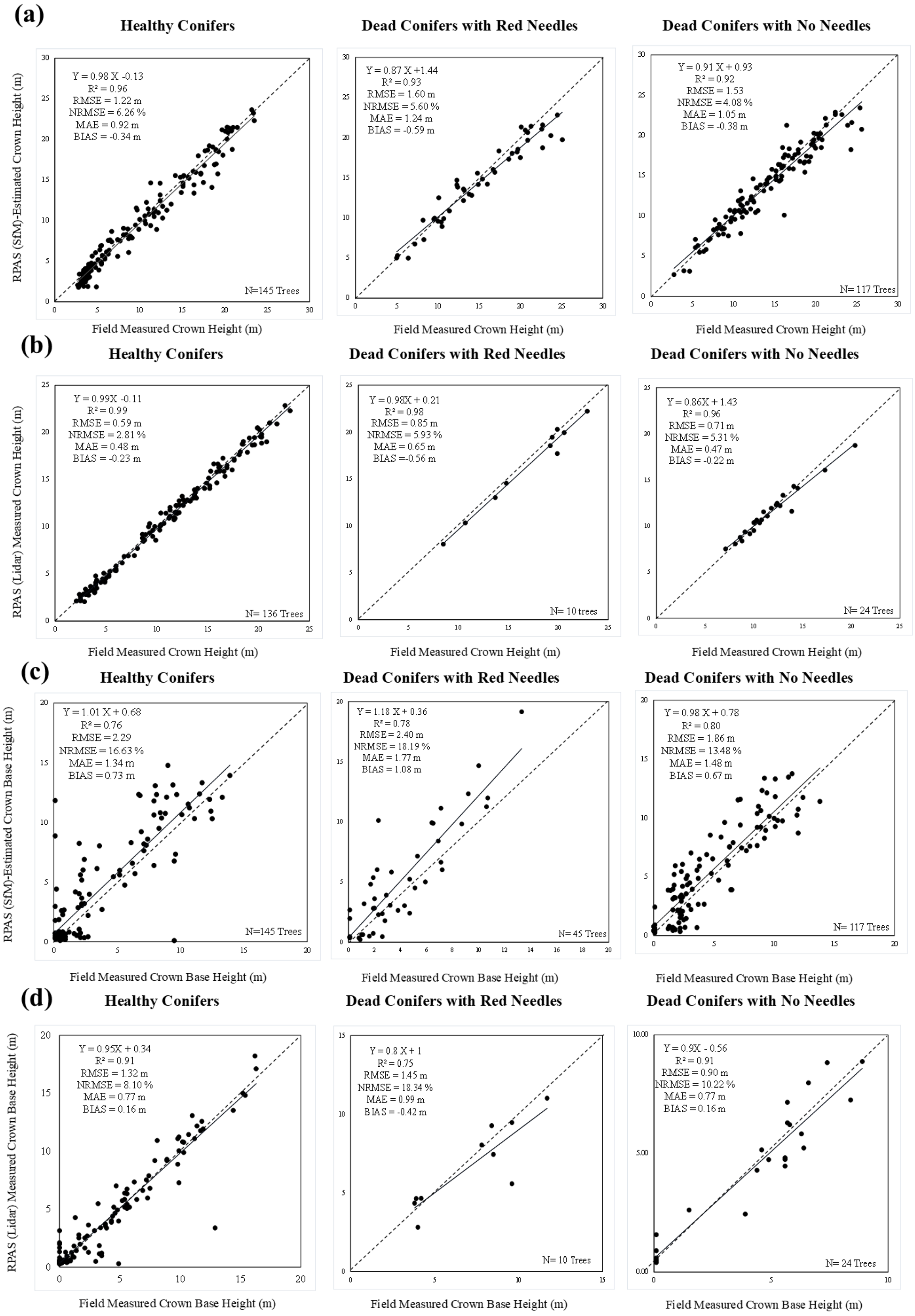

Figure 5.4, A comparison of the accuracy of utilizing photogrammetric and lidar point clouds to measure, a) and b) tree height and, c) and d) crown base height based on the tree mortality.

Even though the accuracy for measuring (lidar)/estimating (photogrammetric) crown base

Diameter at breast height (DBH) is another important factor for estimating canopy fuel load (weight of dry biomass) for use in allometric equations (Equations 1 and 2). Figure 5.5 shows the relationship between tree heights and DBH using RPAS point clouds and a linear regression, restricted to pass through the origin under the assumption that a tree with zero height has a DBH of zero. This model was employed to estimate DBH for all individual trees in each plot using tree height, and the predicted DBH were then used for estimating CFL in the next sections using allometric equations.

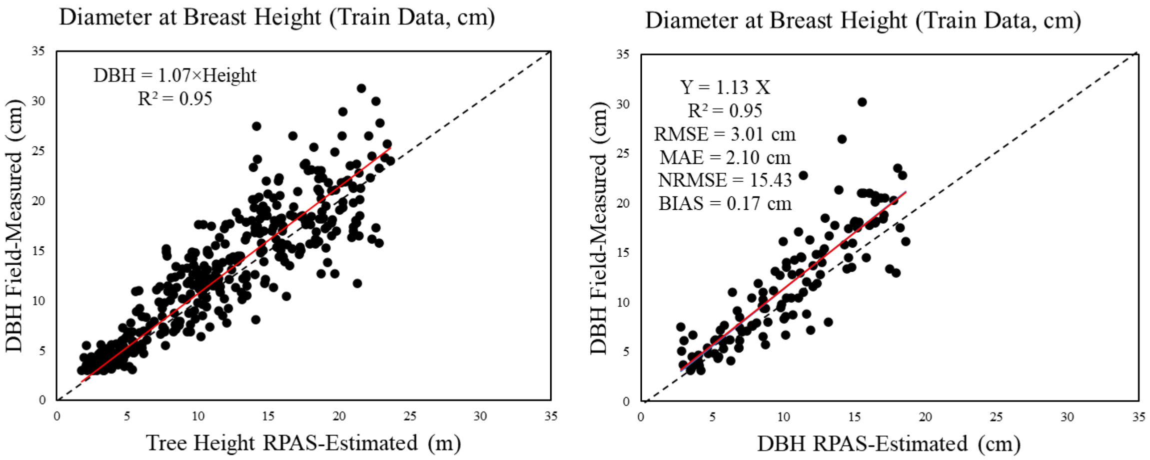

Figure 5.5, a) Linear regression model for estimating DBH using tree height and b) Validation of the predicted DBH against field-measured DBH for 25% of trees not used in model development

Figure 5.6 compares crown fuel load estimated using allometric equations and RPAS-derived tree height, diameter at breast height, and tree species. The estimation of crown fuel load for healthy conifers was more accurate (R^2 = 0.38; RMSE = 1.92 kg. tree^{-1}; NRMSE = 15.7%) compared with dead conifers with red needles (R^2 = 0.11; RMSE = 12.2 kg. tree^{-1}; NRMSE = 21.1%) and dead conifers with no needles (R^2 = 0.29; RMSE = 7.8 kg. tree^{-1}; NRMSE = 12.0%), illustrating increased uncertainties when using modelled DBH. There was more underestimation of crown fuel load for all unhealthy conifers (dead conifers with needles, BIAS= -4.66 kg. tree^{-1}; dead conifers without needles, BIAS= -1.71 kg. tree^{-1}). The primary reason for these underestimations was uncertainty associated with the allometric equations as small inaccuracies in tree height and DBH estimations can result in significant biases in crown fuel load estimates due to the sensitivity of the allometric model to input errors.

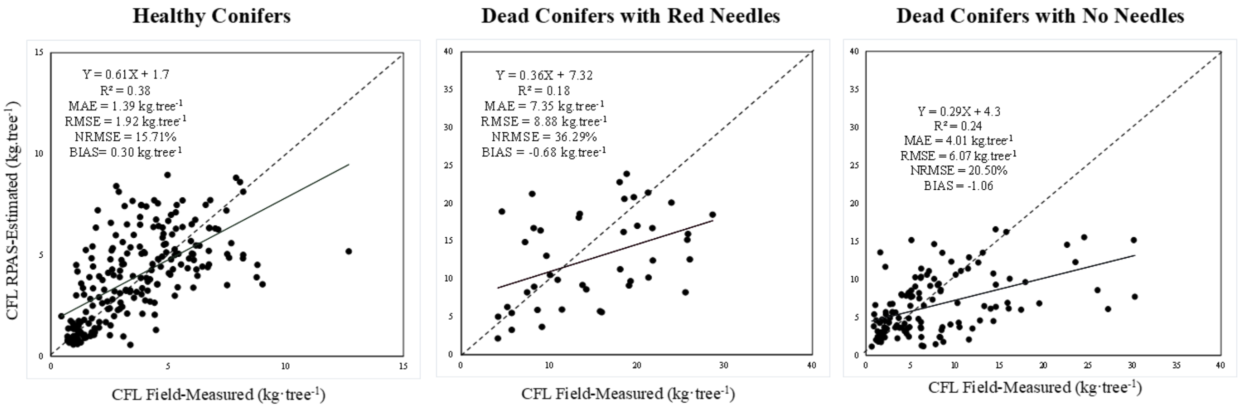

Figure 5.6, Comparison of the accuracy of RPAS (photogrammetric and lidar combined) point clouds to estimate crown fuel load based on individual tree condition.

5.3.3 Distribution of fuels with Proportion of Tree Mortality at Plot-level

A noticeable shift from the canopy foliage volume to the forest floor was observed within plots with greater proportion of tree mortality (Figure 5.7). For example, plot 15 had the lowest tree mortality (Figure 5.7) and the highest volume of foliage (2,600 m^3/plot) while plot 7 had one of the highest tree mortalities and the lowest volume of foliage (200 m^3/plot). Figure 5.7 provides graphical comparison of the total foliage volume across 16 plots.

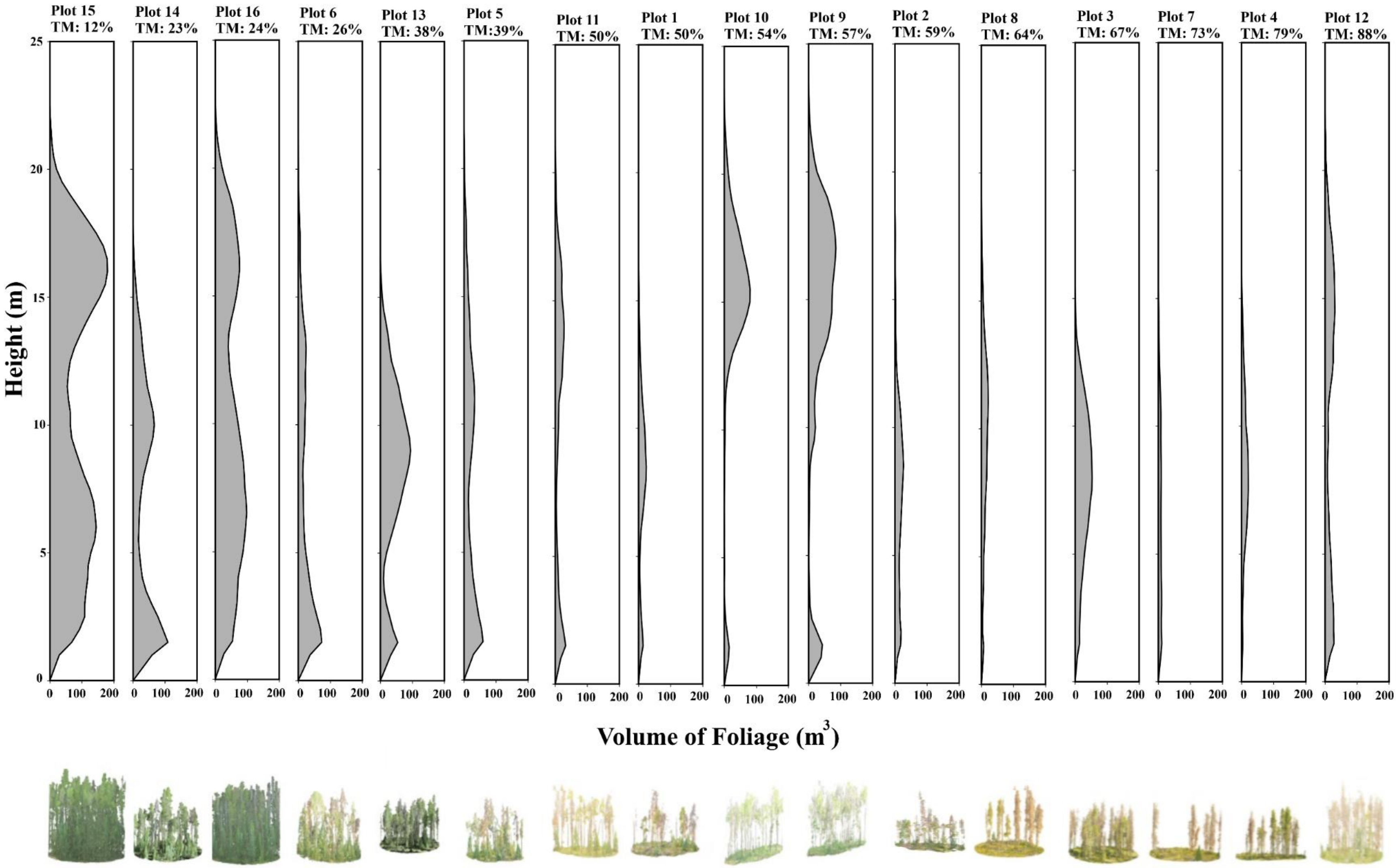

Figure 5.7, Comparison of vertical conifer foliage volume at 0.50 m increments in 16 plots using vertical vegetation profiles.

Figure 5.8 shows a comparison of the amount of canopy fuel load and bulk density per square meter (RPAS detected trees only) determined from allometric equations using RPAS results. Despite high tree density in some plots, plots with mostly dead conifers with red needles and unaffected/green conifers (e.g. Plots 15 and 16) have more canopy fuel load than plots with dead conifers with no needles (Plots 4, 7, 8, and 3) which demonstrates a noticeable shift in canopy fuel load in response to the progression of pine beetle outbreak phases from green to gray.

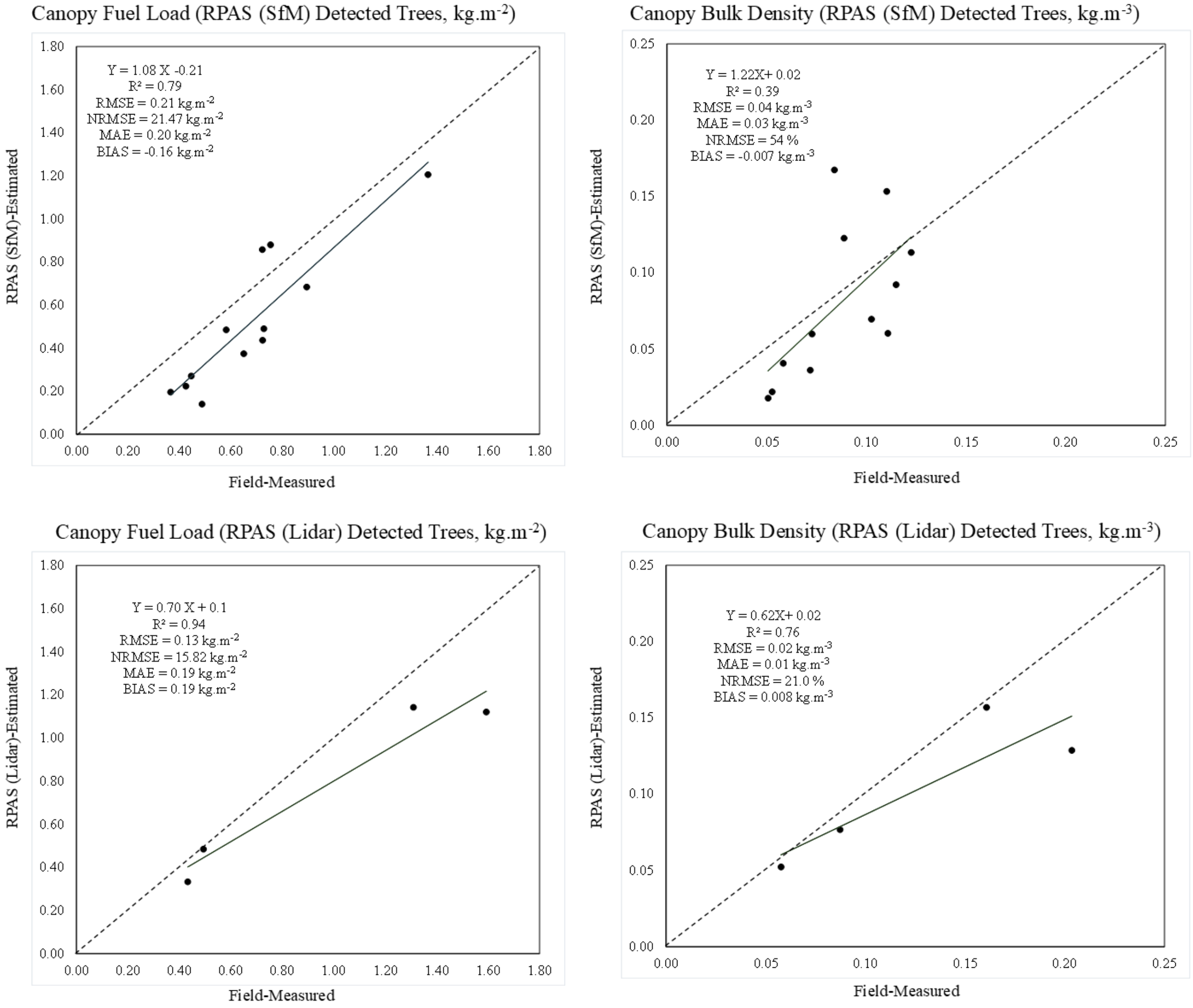

Figure 5.8, Comparison of the accuracy of RPAS point clouds to estimate canopy fuel load and bulk density.

For photogrammetric point clouds (plots 1–12), canopy fuel load was underestimated with a bias of -0.30 kg.m^{-2}, and canopy bulk density was also underestimated with a bias of -0.007 kg.m^{-3}. In contrast, for lidar point clouds (Plots 13–16), canopy fuel load was overestimated with a bias of 0.19 kg.m^{-2}, and canopy bulk density was similarly overestimated with a bias of 0.008 kg.m^{-3} (Figure 5.8).

5.4 Summary

In this chapter, an individual tree-based workflow was employed to quantify common crown/canopy fuel in MPB affected mountain forests. Lidar system proved to be more accurate than photogrammetric systems for measuring/estimating tree height and canopy base height. Diameter at breast height was found to be highly correlated with tree height. Crown/canopy fuel load and canopy bulk density calculation had a moderate accuracy using RPAS point clouds, but there was underestimation for photogrammetric systems. Plots with less tree mortality have more volume of foliage than plots with higher tree mortality due to shift of fuel to forest floor.

Chapter 6. Discussion

One of the primary methods for quantifying forest fire fuels and assessing fuel dynamics over time is using plot-based field measurements. However, field measurements have several limitations: They are labor-intensive and expensive (Goodbody et al., 2023; Chasmer et al., 2020, 2020a; Chen et al., 2017), limited in spatial coverage and are generally inadequate for large-area due to sampling bias (Dietmaier *et al.*, 2019) due to a lack of unbiased and sufficient samples for a large study area, and the potential for human/equipment errors; and lastly, accessibility to the entire study area can be difficult. In contrast, broad-area forest management and fire behavior prediction strategies utilize a wide range of remote sensing technologies to estimate the spatial and temporal variability of fuel (Gale et al., 2021; Jolly et al., 2012a).

Recently, RPAS platforms have gained popularity for forest monitoring because of the unique ability to collect data at high spatial and temporal resolutions (Guimarães et al., 2020; Tang and Shao, 2015) using user-friendly technologies and software. In this thesis, three RPAS systems were utilized and compared: photogrammetric methods and lidar for 3D structure and multispectral and structural information for species classification. These were used to quantify and assess forest fuel variability based on attack phase. The comprehensive methodology developed highlights the effectiveness of RPAS for forest monitoring.

6.1 Initial Processing and Georeferencing of RPAS SfM and Lidar Data

An innovative geometric correction and georeferencing workflow, including point cloud registration and global polynomial transformation were used to georeference RPAS data in this study. Although many studies have demonstrated the effectiveness of the ICP algorithm for point cloud registration (e.g. Sang et al., 2022; Li et al., 2020), ICP alone is inherently limited to handling linear scaling and is prone to local minima errors (Maiseli, Gu and Gao, 2017). These limitations are noticeable especially in the case of photogrammetric point clouds, which often require non-linear scaling registrations (Cao et al., 2023; Decker et al., 2020; Yang et al., 2016; Xie et al., 2010). To address these, Qi et al., (2022) utilized cloud-to-cloud distance measurements to evaluate ICP performance on RPAS point clouds by iteratively calculating the distances between two point clouds reapplying ICP. Although this workflow achieved high accuracy, this can be time-consuming and is not suitable for non-linear scalability registration associated with photogrammetric point clouds. Persad et al. (2017) also developed a method for the registration of photogrammetric point clouds to airborne lidar point clouds using tie points to calculate the 3D Conformal Transformation parameters and then register photogrammetric point clouds with RMSE of 0.47 m using these parameters. The main limitation of their study was that 3D conformal transformation can be used for linear scaling registration, while photogrammetric point cloud registration needs non-linear scaling registration.

In this thesis, this issue was resolved by utilizing an initial registration method (the point pair picking method) to improve the accuracy and decrease the RMSE of the point cloud registration using ICP. An average RMSE of RPAS point cloud registration of 0.30 m was achieved, which is high in the absence of GNSS and base station data for RPAS data collected in 2021 (Plots 1-12) (Table 3.1). Even though Mao et al., (2021) recommended using Real-Time Kinematic (RTK), ground control points (GCPs), or a combination of both to achieve acceptable geolocation accuracy, in this case, a workflow was developed to georeference RPAS data without relying on RTK and GCPs in complex and dense forest canopies with acceptable accuracy. From this, a novel technique was presented for aligning RPAS imagery to airborne lidar point clouds using point cloud registration (Figure 2.6, 3.2 and Table 3.1). The second polynomial transformation was most effective for eliminating all non-linear horizontal warps from RPAS multispectral data.

6.2 Object-Based Analysis and RPAS Imagery to Determine Tree Canopy Cover, Species

The high spatial resolution offered by multispectral and RGB RPAS imagery facilitates relatively accurate vegetation species classification, which are important for identifying vegetation species and condition/mortality, and estimating biomass (Chadwick *et al.*, 2020) (Figure 2.6). GEOBIA involves a workflow for segmenting multispectral imagery into homogeneous objects based on spectral and spatial characteristics (Ming et al., 2018; Chen et al., 2018), and then trains and applies a classifier (e.g. SVM). The main advantage of shape-based method over traditional pixel-based classification is the consideration of the geometry of features in addition to spectral information during training (Whiteside, Boggs and Maier, 2011). SVM has been established as an effective machine learning approach for both tree species classification and vegetation health assessment (Abdollahnejad and Panagiotidis, 2020). High accuracy was in the identification of tree species utilizing vegetation indices, five spectral bands and structural information (Figure 4.2, and Tables 4.3-4.6). Abdollahnejad and Panagiotidis, (2020) used GEOBIA with spectral and structural RPAS data to classify tree species, mostly Norway Spruce and Scots Pine. The overall accuracy and Kappa coefficient of their results were 81.2% and 0.70, respectively, which were less than the average overall accuracy 90% and Kappa coefficient 0.84 of this study (Table 4.3-4.5). However, some challenges were observed in accurately classifying dead conifer trees due to the spectral similarity among dead conifers. Here, Lodgepole pine were more accurately classified than other species in our study area due to their distinctive spectral characteristics and as the dominant tree species. Lastly, higher overall accuracy (~90 %) was achieved for classification of coarse woody debris. Others, e.g. Jarron et al., (2021) achieved 64%, while Lopes Queiroz et al., (2019) achieved 93.4 ± 4.2% using similar methods. Jarron et al., (2021) used airborne lidar point clouds (23 points/m^2) and utilized Cloth Simulation Filter (to separate understory points) and a linear feature extraction method (to map coarse woody debris), which were expected to have less accuracy than GEOBIA.

While SVM was selected for some reasons such as limited training data for some classes (e.g. white spruce) and software limitations. It is important to note that it has limitations: the method is less effective for classifying classes with overlapping spectral responses especially in the case of high number of classes. Random Forest could potentially produce similar or better results due to its robustness for handling complex classifications. However, as Random Forest was not supported in NV5 software, SVM were used as the most suitable option for this thesis.

6.3 3D Fuel Attributes Using Photogrammetric and RPAS Lidar Point Clouds

Photogrammetric and lidar point clouds were utilized to quantify vertical (tree) fuel attributes including tree height, canopy base height, and canopy fuel load. Photogrammetric point clouds were derived from passive optical remote sensing data which can be used to quantify vertical forest fire fuel structures using the Structure from Motion (SfM) methodology. Photographs with high sidelap of forests with open canopies have reduced canopy occlusion (Iglhaut *et al.*, 2019). The vertical forest structures and therefore the availability of fuel when dry, available for wildland fires can be estimated using point cloud metrics and common prediction or statistical methods such as random forest regression (e.g.; Chávez-Durán et al., 2024; Cova et al., 2023; Hoffrén et al., 2023; Cameron et al., 2022; Cameron, 2020; Filippelli et al., 2019; Shin et al., 2018).

In this study, tree height was determined using the maximum elevation of each individual tree point (Figure 5.1 d) and crown base height from classified (stem and foliage) tree points using region-based methods directly from point clouds (Figure 5.1 e). Crown base height is a challenging but important fuel metric for quantifying canopy bulk density, which is an important fuel attribute that we can get for understanding and predicting fire behaviour.

During the classification of stem and foliage, colour and intensity attributes alone were not sufficient for training of the SVM classifier. However, similar to Duran et al., (2021), the addition of geometric features improved training of SVM for trees that were visible (not occluded) to the RPAS optical imagery. The main limitation for this classification was the presence of seedlings, shrubs, and short vegetation near the stem of the tree, reducing the ability to determine geometric features (especially found in plots 15 and 16, Figure 5.3).

Using 3D data, TreeIso (Xi and Hopkinson, 2022) was an effective method for identifying 3D individual trees, but has some limitations using RPAS point clouds due to overlapping canopies. Here, the Density-Based Spatial Clustering of Applications with Noise (DBSCAN), Ester et al., (1996), technique was used to rectify the results of TreeIso and separate two trees identified as one tree (Figure 5.1 c). The TreeIso method uses 3D and 2D cut-pursuit clustering and identifies individual tree points based on the gaps between trees, which has advantages over 2D individual tree detection methods commonly used for tree segmentation based on local maxima and estimating crown boundaries (Chávez-Durán et al., 2024; Aubry-Kientz et al., 2019; Goldbergs et al., 2018; Shin et al., 2018; Nevalainen et al., 2017). Using TreeIso and Density-

Based Spatial Clustering of Applications with Noise (DBSCAN), small trees covered by tall trees, which are the main limitations of 2D individual tree detection, can be detected (Figure 5.1 c).

Tree height measurements using both RPAS lidar (R^2= 0.99, RMSE= 0.59 m, NRMSE= 2.81%) and photogrammetric point clouds (R^2= 0.96, RMSE= 1.22 m, NRMSE= 6.26%), compared very well with field measurements regardless of tree mortality, density, and canopy cover (Figure 5.4 a and b). Qi et al. (2022b) used quantitative structure models for quantification of tree metrics such as height and achieved $R^2 > 0.80$ and NRMSE < 16% regardless of tree density and canopy cover in southern British Columbia, Canada. Zhang et al., (2021) also developed methods for tree height in tropical forests using both photogrammetric and lidar point clouds and found that both datasets had almost the of accuracy with $R^2 = 0.88$ and RMSE = 1.6 m. This suggests that tree height can be reliably measured/estimated regardless of forest type and canopy conditions, using photogrammetry and lidar systems.

Crown/canopy base height is one of the challenges but is important for modeling fire behaviors and prediction of active crown fires. Most studies achieved moderate correlation and accuracy compared to field data. For example, Shin et al. (2018) used a prediction model to estimate canopy base height using photogrammetric point clouds from relatively dense canopies and found a weaker correlation ($R^2 = 0.34$, RMSE = 2.52 m) with field data. Arkin et al., (2021) also estimated canopy base height using RPAS lidar point clouds by characterizing the vertical distribution of points and they obtained $R^2 = 0.31$ and RMSE = 3.55 m. In another study, Arkin et al. (2023a) used photogrammetric and lidar point clouds to quantify common forest fire fuels around Williams Lake, British Columbia, Canada. They extracted various predictor variables (height percentiles, max height, canopy relief ratio etc.) to develop many linear regression models to predict forest fire fuel attributes such as canopy fuel load, canopy bulk density, canopy base height etc. Based on their validation and accuracy assessment, they found that lidar (R^2 = 0.63 and NRMSE = 19.33%) had almost the same accuracy as photogrammetric point clouds (R^2 = 0.69 and NRMSE = 17.81%) for quantifying canopy base height. However, the innovative workflow used in this study based on classified point clouds and region-based methods was highly accurate using photogrammetric point clouds (R^2= 0.76, RMSE= 2.29 m, NRMSE= 16.63%) and lidar (R^2= 0.91, RMSE= 1.32 m, NRMSE= 8.10%) (Figure 5.4 c and d).

Although our plots (e.g., 1.8 million points (~130 trees) in plot 15 (Figure 5.3)) were denser and had greater canopy overlap than plots in Arkin et al. (2023a) (0.40 million points with almost the same average point density), the methods developed here were more accurate for quantifying crown base height using both lidar and photogrammetric point clouds at the tree-level (Figure 5.4 c and d). Although the accuracy of the results of this study for measuring crown base height were better than similar studies for healthy/green conifers, the accuracy for measuring crown base height of dead conifers with no needles (R^2= 0.80, RMSE= 1.86 m, and NRMSE= 13.48%) and dead conifers with red needles (R^2= 0.78, RMSE= 2.40 m, and NRMSE=18.19%) were better than healthy/green conifers since trees lost needles/small branches and there was less canopy occlusion

(Figure 5.4 c and d). One limitation in quantifying crown base height is the presence of understory canopy/ladder fuels near stems, where some trees were less accurately represented by small branches. These were misclassified as foliage points (Figure 5.3) leading to a slight over- and under-estimated in canopy base heigh quantifications in some situations. In contrast, due to canopy occlusion, crown base height quantifications using photogrammetric point clouds were overestimated due to gaps (lack of points/information under canopy because of canopy occlusion) (Figure 5.4 c and d), which will have some implications for calculating the canopy bulk density from canopy fuel load and the canopy length. In addition to all of these, the primary limitation in utilizing our workflow for crown base height quantification at the tree-level is the need to develop an individual tree detection method suitable for RPAS point clouds. TreeIso was originally designed for terrestrial laser scanning point clouds with minimal gaps in individual tree points, while RPAS point clouds, especially photogrammetric point clouds contain several gaps in the close canopies due to canopy occlusion.

Another important fuel attribute for modeling and predicting fire behavior is crown/canopy fuel load. Allometric equations have been widely used for quantifying crown fuel load using DBH, height, and tree species (Phelps et al., 2022; Ung et al., 2008; Lambert et al., 2005). Due to noise in accurately classifying the stem points, insufficient points for trees with small diameter at breast height, and canopy occlusion, quantifying diameter at breast height directly from RPAS point clouds is challenging and prone to large uncertainties. However, due to the strong correlation between tree height and DBH (Nunes Miranda et al., 2022; Chen et al., 2020; Sharma and Parton, 2007; Peng et al., 2001), simple linear regression can be used to estimate DBH using only height attributes. Studies have been conducted to estimate crown/canopy fuel load, the weight of canopy biomass per unit area/tree using only field data (Phelps et al., 2022; Ung et al., 2008; Lambert et al., 2005). However, studies have used field data to calibrate remote sensing data and to develop models for predicting crown/canopy fuel load for larger area using these data. For example, Hartley et al., (2022) used a variety of spatial and intensity metrics from RPAS lidar point clouds to develop a prediction regression model for estimating above ground biomass of wilding conifer forests in Aotearoa New Zealand. Their results indicated that total above ground biomass has an NRMSE range between 11.3% to 34.5%. In this study a slightly better accuracy was achieved with NRMSE at the range of (11.9% to 21.1%). Arkin et al., (2023a) also used FuelCalcBC based on the methods presented in Sando, (1972) to estimate canopy fuel load using both lidar and photogrammetric point clouds. They achieved an accuracy of R^2= 0.67 using lidar point clouds at the plot level. However, the results of this study achieved R^2 = 0.94 (Figure 5.8), despite the high density of trees in our lidar plots, including small trees and those occluded by the canopy, which are more difficult to estimate using RPAS methods and with varying mortality (Figure 5.8).

The workflow for the utilization of three RPAS technologies in this study presents several advantages compared to similar studies, but there are some opportunities for future improvements. First of all, the use of multispectral RPAS data proves effective in mapping visible coarse woody debris within fairly open forest canopies. However, there are two main limitations of GEOBIA: shadow and canopy occlusion in dense forest canopies. Therefore, coarse woody debris can be mapped with a GEOBIA workflow with a high level of accuracy in the absence of shadow and in open canopies (Figures 4.1 and 4.2). However, there are also issues regarding canopy closure and overlapping coarse woody debris, resulting in gaps in single fallen stems, for example. Therefore, it is recommended to conduct further investigation to find methods to fill these gaps between different parts of a coarse woody debris, such as gap filling and reconstruction (possibly considering close coarse woody debris with the same azimuth/bearing as a single coarse woody debris and fill the gap). It is also recommended to explore/develop an individual coarse woody debris detection method to identify each coarse woody debris and removing branches. This allows us to calculate the width and length of each coarse woody debris and then estimating their volume or probably biomass. Additionally, as seen in Figure 4.2 and Tables 4.3-4.6, GEOBIA can identify tree species; however, the difference in overall accuracy between pixel-based and feature-based (considering small trees below the canopy occlusion) accuracy assessments shows that the biggest limitation for using GEOBIA to identify tree species is canopy occlusion and the inability to identify small trees under tall trees.

RPAS lidar and photogrammetric point clouds were highly accurate for quantification of tree height and compared well with field measurements despite conifer mortality/conditions (Figure 5.4 a and b). RPAS lidar was more accurate for quantifying crown base height than photogrammetric point clouds (Figure 5.4 a and b). This underestimation for quantifying crown base height using photogrammetric point clouds has two reasons: a) lack of proper individual tree detection for RPAS point clouds with many gaps, and b) canopy occlusion resulting in a lack of information on occluded parts of trees (Figure 5.4 c and d). Therefore, it was observed that photogrammetric point clouds have better accuracy for measuring crown base height for dead conifers with no needles (NRMSE = 13.48%) than for healthy/green conifers (NRMSE = 16.63%) and dead conifers with red needles (NRMSE = 18.19%) due to less canopy occlusion (Figure 5.4 c and d). Additionally, crown fuel load results indicated a moderate correlation between RPAS-estimated results and field data due to the limitation of allometric equations and their high sensitivity to a small error in tree height and DBH. The highest accuracy for quantifying crown fuel load belonged to healthy/green conifers using photogrammetric point clouds (R^2 = 0.38, NRMSE = 15.71% and BIAS= 0.30 kg. tree^{-1}). Although, there is underestimation in quantifying canopy fuel load using photogrammetric point clouds, RPAS lidar has a better accuracy for estimating canopy fuel load in plots (plots 13,14 and 15) (Figure 5.8).

6.4 Fire Fuel Distribution Assessments associated with Tree Mortality

Schoennagel et al., (2012) conducted a study in lodgepole pine forests of northern Colorado, US, to answer the question of how forest fire fuels interact with MPB outbreaks across four green, red, gray, and old stage of MPB attack phases. They used field measurements including tree height, diameter at breast height and canopy base height. They also estimated canopy fuel load using diameter at breast height and tree species at the tree level and then calculated canopy bulk density. They found that dead foliage fuel load was significantly high in trees in the red attack phases, and the surface fire fuels increase in the gray and old stages of MPB outbreaks. Similarly, our research indicated the amount of canopy fuel load and volume of foliage in gray phase decrease significantly due to shift of canopy fuel to forest floor (Figures 5.7, and 5.8). Additionally, it was observed that despite tree mortality, plots with high level of tree density (Plots 15, 16, 9, 12 and 10) have more canopy fuel load.

In addition to CFL and CBD comparisons, the volume of foliage was also used to better understand how MPB outbreaks affect fire fuel availability. It was observed that plots with less tree mortality (e.g., Plots 15, 16, 14, and 6) had more foliage volume. However, the volume of foliage in plots with mostly dead conifers with or without needles is less than in unaffected areas. Therefore, it is expected that there will be more fuels on the forest floor due to the shift of fuels from canopy to floor also observed in Jenkins et al., 2014; Simard et al., 2011, where they found that almost all needles shifted vertically to forest floor following MPB outbreak and tree mortality.

Chapter 7. Conclusions

7.1 Research Overview

This study investigated the quantification of vegetation/tree structures and forest fire fuels post-MPB outbreak in Jasper National Park using three popular RPAS systems/technologies (multispectral imagery, photogrammetric, and lidar point clouds). This thesis includes 7 chapters and addresses two main objectives. The first main objective was to develop a workflow utilizing these three RPAS systems to quantify forest fire fuels. The second main objective was to better understand vertical/horizontal forest fire fuel availability in response to MPB outbreak as trees die and to answer the question of how forest fire fuel in Jasper National Park has changed in response MPB-based tree mortality.

In Chapter 3, an innovative workflow was introduced to eliminate all offsets between these three datasets with field data (GNSS) and airborne lidar to have a consistent spatial reference system.

In Chapter 4, machine learning and high-resolution multispectral image classification was applied to identify tree species and to map visible coarse woody debris. Canopy and coarse woody debris coverage were compared in 16 plots based on tree mortality using field data collection at the individual tree and plot levels.

In Chapter 5, an innovative workflow was developed/applied to quantify various important/required 3D fuel attributes for fire behavior modeling at the tree level using photogrammetric and lidar RPAS point clouds. It was observed that some fire fuel attributes, such as tree height and canopy base height, can be quantified directly from RPAS point clouds at the tree level, independent of field data with a high level of accuracy. Additionally, other important fire fuel metrics, such as canopy fuel load and diameter at breast height, were estimated at the tree level using field data and the results of RPAS tree height. Moreover, volumetric attributes, canopy fuel load, and canopy bulk density at the plot level were used to assess the change of fuel in response to tree mortality. Lastly, vertical/horizontal fuel availability and the shift from canopy fuel to the forest floor were discussed to better understand the interaction between MPB outbreaks and the vertical and horizontal distribution of fire fuels with increasing proportions of mortality.

In Chapter 6, the accuracy of all these fuel attributes/metrics and fuel changes were discussed based on tree mortality and conifer cover/conditions. These were compared with the literature.

7.2 Technical and Ecological Conclusion

Jasper National Park as one of the oldest parks in Canada has been significantly affected by MPB outbreak in the past two decades due to homogeneity of mature pine trees because of more than a century of fire suppression history. During the last decade RPAS systems have become popular technologies for collecting forest fire fuel data and can help to address the limitations of field data. In this case, a comprehensive methodology workflow was developed from georeferencing of three different RPAS datasets, classification, and quantification of forest fire fuels using three RPAS systems. RPAS multispectral data was found to be accurate for identifying tree species using both spectral and spatial attributes. Furthermore, RPAS point clouds were found to be effective for quantifying canopy forest fuel. Moreover, machine learning and a region-based method can be used to classify above ground biomass points to stem and foliage and quantifying canopy base height respectively. Photogrammetry and lidar point clouds can both provide high accuracy measurements of tree height and canopy base height independent of field data. Additionally, RPAS results can be used to quantify canopy fuel load using allometric equations. It was observed that RPAS lidar point cloud has moderate/high level of accuracy for estimating canopy fuel load and bulk density using the lidar system, but there were underestimation using photogrammetric point clouds. Additionally, plots with dead conifers with red or no needles have less foliage volume than healthy conifers due to shift of canopy fuel to forest floor.

7.3 Recommendations/Suggestions for Fuel Treatment

Due to the increased surface (can start a fire) and canopy fuel load (both branches and foliage are dry) in the red phase of MPB outbreaks, it is recommended to focus on these areas for fuel treatments more than other areas in green and gray MPB attack phases. First, it is recommended to increase the canopy base height of trees in these areas by pruning and remove ladder fuels to prevent transferring fires from the forest floor to the crown and generate active crown fires. Then, prescribed/controlled fires are recommended to clear the forest floor from needles and small woody components/branches that shifted from the canopy in red phase to eliminate the ignition hazard. If trees in the red phase are close to towns/facilities, it is also recommended to create fuel breaks and remove all fuels through a line to separate these areas from facilities in addition to conducting those fuel treatments.

7.4 Future Work and Suggestions

Future research may explore the utilization of more spectral and structural metrics to enhance SVM models for tree species/conditions classifications. It is also recommended to check alternative classification algorithms such as Random Forest, to potentially improve the model accuracy and robustness. Moreover, it is suggested to explore a new workflow for reconstructing and gap-filling visible coarse woody debris that occluded by canopy. Given that calculating/estimating coarse woody debris volume and fuel load need the diameter and length of each individual coarse woody debris, future research may explore methods for identifying individual coarse woody debris structures (removing branches and separating overlapped coarse woody debris). Given that accurate individual tree detection can improve the accuracy of estimating fuel attributes (e.g. canopy fuel load, canopy bulk density, and canopy base height), further exploration of individual tree detection methods specific to RPAS point clouds should be considered. Finally, due to uncertainties associated with using allometric equations, future research should develop new methods for quantifying tree metrics especially foliage volume to dry weight biomass using RPAS point clouds.

References

Abdollahnejad, A. and Panagiotidis, D. (2020) ‘Tree Species Classification and Health Status Assessment for a Mixed Broadleaf-Conifer Forest with UAS Multispectral Imaging’, *Remote Sensing*, 12(22), p. 3722. Available at: https://doi.org/10.3390/rs12223722.

Alonzo, M. *et al.* (2018) ‘Quantifying Boreal Forest Structure and Composition Using UAV Structure from Motion’, *Forests*, 9(3), p. 119. Available at: https://doi.org/10.3390/f9030119.

Andersen, H.-E., McGaughey, R.J. and Reutebuch, S.E. (2005) ‘Estimating forest canopy fuel parameters using LIDAR data’, *Remote Sensing of Environment*, 94(4), pp. 441–449. Available at: https://doi.org/10.1016/j.rse.2004.10.013.

Anderson, K.R. (1978) ‘A reevaluation of an efficient algorithm for determining the convex hull of a finite planar set’, *Information Processing Letters*, 7(1), pp. 53–55. Available at: https://doi.org/10.1016/0020-0190(78)90041-8.

Araujo, R.F. *et al.* (2020) ‘Integrating high resolution drone imagery and forest inventory to distinguish canopy and understory trees and quantify their contributions to forest structure and dynamics’, *PLOS ONE*. Edited by J. Müllerová, 15(12), p. e0243079. Available at: https://doi.org/10.1371/journal.pone.0243079.

Arkin, J. *et al.* (2019) ‘Integrated fire severity–land cover mapping using very-high-spatial-resolution aerial imagery and point clouds’, *International Journal of Wildland Fire*, 28(11), p. 840. Available at: https://doi.org/10.1071/WF19008.

Arkin, J. *et al.* (2023) ‘Canopy and surface fuel estimations using RPAS and ground-based point clouds’, *Forestry: An International Journal of Forest Research* [Preprint]. Available at: https://doi.org/10.1093/forestry/cpad020.

Atik, M.E., Duran, Z. and Seker, D.Z. (2021) ‘Machine Learning-Based Supervised Classification of Point Clouds Using Multiscale Geometric Features’, *ISPRS International*

Journal of Geo-Information, 10(3), p. 187. Available at: https://doi.org/10.3390/ijgi10030187.

Aukema, B.H. *et al.* (2006) 'Landscape level analysis of mountain pine beetle in British Columbia, Canada: spatiotemporal development and spatial synchrony within the present outbreak', *Ecography*, 29(3), pp. 427–441. Available at: https://doi.org/10.1111/j.2006.0906-7590.04445.x.

Axelson, J.N. *et al.* (2011) 'Ecological Impacts of the Mountain Pine Beetle on Pine Forests of the Southern Foothills , Alberta : A Case Study in Waterton Lakes National Ecological Impacts of the Mountain Pine Beetle on Pine Forests of the Southern Foothills , Alberta A Case Study in', (August 2016).

Baker, J.R. *et al.* (1994) 'Relationships between physical characteristics and polarimetric radar backscatter for Corsican pine stands in Thetford Forest, U.K.', *International Journal of Remote Sensing*, 15(14), pp. 2827–2849. Available at: https://doi.org/10.1080/01431169408954287.

Becker, C. *et al.* (2018) 'Classification of Aerial Photogrammetric 3D Point Clouds', *Photogrammetric Engineering & Remote Sensing*, 84(5), pp. 287–295. Available at: https://doi.org/10.14358/PERS.84.5.287.

Beland, M. *et al.* (2015) 'White Paper – On the Use of LiDAR Data at AmeriFlux Sites', *AmeriFlux Meetings and Workshops*, (December), pp. 1–33. Available at: https://doi.org/https://hdl.handle.net/10779/uos.23426096.v1.

Bennett, L. *et al.* (2022) 'Image to attribute model for trees (ITAM-T): individual tree detection and classification in Alberta boreal forest for wildland fire fuel characterization', *International Journal of Remote Sensing*, 43(5), pp. 1848–1880. Available at: https://doi.org/10.1080/01431161.2022.2048914.

Bentz, B.J. *et al.* (2010) 'Climate change and bark beetles of the western United States and Canada: Direct and indirect effects', *BioScience*, 60(8), pp. 602–613. Available at:

https://doi.org/10.1525/bio.2010.60.8.6.

Berni, J. *et al.* (2009) ‘Thermal and Narrowband Multispectral Remote Sensing for Vegetation Monitoring From an Unmanned Aerial Vehicle’, *IEEE Transactions on Geoscience and Remote Sensing*, 47(3), pp. 722–738. Available at: https://doi.org/10.1109/TGRS.2008.2010457.

Bernier, P. *et al.* (2016) ‘Mapping Local Effects of Forest Properties on Fire Risk across Canada’, *Forests*, 7(8), p. 157. Available at: https://doi.org/10.3390/f7080157.

Besl, P.J. and McKay, N.D. (1992) ‘A method for registration of 3-D shapes’, *IEEE Transactions on Pattern Analysis and Machine Intelligence*, 14(2), pp. 239–256. Available at: https://doi.org/10.1109/34.121791.

Beutling, A., Batista, A.C. and Soares, R. V. (2012) ‘Fire behavior modeling based on simulated field plots’, in, pp. 27–37. Available at: https://doi.org/10.2495/FIVA120031.

Birdal, A.C., Avdan, U. and Türk, T. (2017) ‘Estimating tree heights with images from an unmanned aerial vehicle’, *Geomatics, Natural Hazards and Risk*, 8(2), pp. 1144–1156. Available at: https://doi.org/10.1080/19475705.2017.1300608.

Boucher, J. Cotton-Gagnon, A. Taylor, S.Perrakis, D.Hanes, C. Thompson, D., and Wotton, M. (2022) ‘Sampling Fuels in the Context of the Next-Generation Canadian Forest Fire Danger Rating System and’.

Brantseg, A. (1967) ‘Volume functions and tables for Scots pine, South Norway.’, pp. 689–739. Available at: https://www.cabidigitallibrary.org/doi/full/10.5555/19670604314.

Breiman, L. (2001) ‘Random Forests’, *Machine Learning*, 45, pp. 5–32. Available at: https://doi.org/10.1023/A:1010933404324.

Brush, M. and Lewis, M.A. (2024) ‘Characterizing the speed and severity of mountain pine beetle spread under climate change with a mechanistic model’. Available at: https://doi.org/10.1101/2024.06.27.601084.

Cabo, C. *et al.* (2019) ‘Multiscale Supervised Classification of Point Clouds with Urban and Forest Applications’, *Sensors*, 19(20), p. 4523. Available at: https://doi.org/10.3390/s19204523.

Calin, M.A., Elfarra, F.-G. and Parasca, S.V. (2021) ‘Object-oriented classification approach for bone metastasis mapping from whole-body bone scintigraphy’, *Physica Medica*, 84, pp. 141–148. Available at: https://doi.org/10.1016/j.ejmp.2021.03.040.

Cameron, H. (2020) *Predicting Fuel Characteristics of Black Spruce Stands Using Airborne Laser Scanning (ALS) in the Province of Alberta, Canada*. University of Alberta. Available at: https://doi.org/10.7939/r3-zc8y-e407.

Canadian_Climate_Normals (2024) *Canada, Environment*. Available at: https://climate.weather.gc.ca/climate_normals/.

Cao, L. *et al.* (2023) ‘A Global Structure and Adaptive Weight Aware ICP Algorithm for Image Registration’, *Remote Sensing*, 15(12), p. 3185. Available at: https://doi.org/10.3390/rs15123185.

Carroll, A.L. *et al.* (2003) ‘Effects of climate change on range expansion by the mountain pine beetle in British Columbia’, *Mountain Pine Beetle Symposium: Challenges and Solutions*.

Castilla, G. *et al.* (2020) ‘Estimating Individual Conifer Seedling Height Using Drone-Based Image Point Clouds’, *Forests*, 11(9), p. 924. Available at: https://doi.org/10.3390/f11090924.

Cessna, J. *et al.* (2021) ‘Mapping Boreal Forest Spruce Beetle Health Status at the Individual Crown Scale Using Fused Spectral and Structural Data’, *Forests*, 12(9), p. 1145. Available at: https://doi.org/10.3390/f12091145.

Chadwick, A.J. *et al.* (2020) ‘Automatic Delineation and Height Measurement of Regenerating Conifer Crowns under Leaf-Off Conditions Using UAV Imagery’, *Remote Sensing*, 12(24), p. 4104. Available at: https://doi.org/10.3390/rs12244104.

Chadwick, A.J. *et al.* (2022) ‘Species Classification of Automatically Delineated Regenerating Conifer Crowns Using RGB and Near-Infrared UAV Imagery’, *IEEE Geoscience and Remote Sensing Letters*, 19, pp. 1–5. Available at: https://doi.org/10.1109/LGRS.2021.3123552.

Chamberlain, C.P., Sánchez Meador, A.J. and Thode, A.E. (2021) ‘Airborne lidar provides reliable estimates of canopy base height and canopy bulk density in southwestern ponderosa pine forests’, *Forest Ecology and Management*, 481, p. 118695. Available at: https://doi.org/10.1016/j.foreco.2020.118695.

Chasmer, L. *et al.* (2016) ‘A Physically Based Terrain Morphology and Vegetation Structural Classification for Wetlands of the Boreal Plains, Alberta, Canada’, *Canadian Journal of Remote Sensing*, 42(5), pp. 521–540. Available at: https://doi.org/10.1080/07038992.2016.1196583.

Chasmer, L., Cobbaert, D., *et al.* (2020) ‘Remote Sensing of Boreal Wetlands 1: Data Use for Policy and Management’, *Remote Sensing*, 12(8), p. 1320. Available at: https://doi.org/10.3390/rs12081320.

Chasmer, L., Mahoney, C., *et al.* (2020) ‘Remote Sensing of Boreal Wetlands 2: Methods for Evaluating Boreal Wetland Ecosystem State and Drivers of Change’, *Remote Sensing*, 12(8), p. 1321. Available at: https://doi.org/10.3390/rs12081321.

Chasmer, L.E. *et al.* (2017) ‘Using Multitemporal and Multispectral Airborne Lidar to Assess Depth of Peat Loss and Correspondence With a New Active Normalized Burn Ratio for Wildfires’, *Geophysical Research Letters*, 44(23). Available at: https://doi.org/10.1002/2017GL075488.

Chávez-Durán, Á.A. *et al.* (2024) ‘Forest Canopy Fuel Loads Mapping Using Unmanned Aerial

Vehicle High-Resolution Red, Green, Blue and Multispectral Imagery', *Forests*, 15(2), p. 225. Available at: https://doi.org/10.3390/f15020225.

Chen, G. *et al.* (2018) 'Geographic object-based image analysis (GEOBIA): emerging trends and future opportunities', *GIScience & Remote Sensing*, 55(2), pp. 159–182. Available at: https://doi.org/10.1080/15481603.2018.1426092.

Chen, G. and Hay, G.J. (2011) 'A Support Vector Regression Approach to Estimate Forest Biophysical Parameters at the Object Level Using Airborne Lidar Transects and QuickBird Data', *Photogrammetric Engineering & Remote Sensing*, 77(7), pp. 733–741. Available at: https://doi.org/10.14358/PERS.77.7.733.

Chen, H. and Walton, A. (2011) 'Mountain pine beetle dispersal: spatiotemporal patterns and role in the spread and expansion of the present outbreak', *Ecosphere*, 2(6), p. art66. Available at: https://doi.org/10.1890/ES10-00172.1.

Chen, J. *et al.* (2020) 'Using machine learning to synthesize spatiotemporal data for modelling DBH-height and DBH-height-age relationships in boreal forests', *Forest Ecology and Management*, 466, p. 118104. Available at: https://doi.org/10.1016/j.foreco.2020.118104.

Chen, S. *et al.* (2017) 'Measuring Vegetation Height in Linear Disturbances in the Boreal Forest with UAV Photogrammetry', *Remote Sensing*, 9(12), p. 1257. Available at: https://doi.org/10.3390/rs9121257.

Colwell (1983) 'Manual of Remote Sensing', *American Society of Photogrammetry*, 1, p. 2440.
Comesaña-Cebral, L. *et al.* (2021) 'Individual Tree Segmentation Method Based on Mobile Backpack LiDAR Point Clouds', *Sensors*, 21(18), p. 6007. Available at: https://doi.org/10.3390/s21186007.

Congalton, R.G. (1991) 'A review of assessing the accuracy of classifications of remotely sensed data', *Remote Sensing of Environment*, 37(1), pp. 35–46. Available at:

https://doi.org/10.1016/0034-4257(91)90048-B.

Coogan, S.C.P. *et al.* (2021) 'Fifty years of wildland fire science in Canada', *Canadian Journal of Forest Research*, 51(2), pp. 283–302. Available at: https://doi.org/10.1139/cjfr-2020-0314.

Cooke, B.J. and Carroll, A.L. (2017) 'Predicting the risk of mountain pine beetle spread to eastern pine forests: Considering uncertainty in uncertain times', *Forest Ecology and Management*, 396, pp. 11–25. Available at: https://doi.org/10.1016/j.foreco.2017.04.008.

Cooper, S. *et al.* (2017) 'Examination of the Potential of Terrestrial Laser Scanning and Structure-from-Motion Photogrammetry for Rapid Nondestructive Field Measurement of Grass Biomass', *Remote Sensing*, 9(6), p. 531. Available at: https://doi.org/10.3390/rs9060531.

Cova, G.R. *et al.* (2023) 'Evaluating Close-Range Photogrammetry for 3D Understory Fuel Characterization and Biomass Prediction in Pine Forests', *Remote Sensing*, 15(19), p. 4837. Available at: https://doi.org/10.3390/rs15194837.

Creasy, M.B. *et al.* (2021) 'Potential for individual tree monitoring in ponderosa pine dominated forests using unmanned aerial system structure from motion point clouds', *Canadian Journal of Forest Research*, 51(8), pp. 1093–1105. Available at: https://doi.org/10.1139/cjfr-2020-0433.

Delegido, J. *et al.* (2013) 'A red-edge spectral index for remote sensing estimation of green LAI over agroecosystems', *European Journal of Agronomy*, 46, pp. 42–52. Available at: https://doi.org/10.1016/j.eja.2012.12.001.

Dhar, A. *et al.* (2015) 'Impact of a Mountain Pine Beetle Outbreak on Young Lodgepole Pine Stands in Central British Columbia', *Forests*, 6(10), pp. 3483–3500. Available at: https://doi.org/10.3390/f6103483.

Dietmaier, A. *et al.* (2019) 'Comparison of LiDAR and Digital Aerial Photogrammetry for Characterizing Canopy Openings in the Boreal Forest of Northern Alberta', *Remote Sensing*, 11(16), p. 1919. Available at: https://doi.org/10.3390/rs11161919.

DJI (2020) ‘P4 Multispectral User Manual’, pp. 1–148.

Duran, Z., Ozcan, K. and Atik, M.E. (2021) ‘Classification of Photogrammetric and Airborne LiDAR Point Clouds Using Machine Learning Algorithms’, *Drones*, 5(4), p. 104. Available at: https://doi.org/10.3390/drones5040104.

Edwards, M., Krawchuk, M.A. and Burton, P.J. (2015) ‘Short-interval disturbance in lodgepole pine forests, British Columbia, Canada: Understory and overstory response to mountain pine beetle and fire’, *Forest Ecology and Management*, 338, pp. 163–175. Available at: https://doi.org/10.1016/j.foreco.2014.11.011.

Embrey, S., Remais, J. V. and Hess, J. (2012) ‘Climate Change and Ecosystem Disruption: The Health Impacts of the North American Rocky Mountain Pine Beetle Infestation’, *American Journal of Public Health*, 102(5), pp. 818–827. Available at: https://doi.org/10.2105/AJPH.2011.300520.

Enayetullah, H. *et al.* (2022) ‘Identifying Conifer Tree vs. Deciduous Shrub and Tree Regeneration Trajectories in a Space-for-Time Boreal Peatland Fire Chronosequence Using Multispectral Lidar’, *Atmosphere*, 13(1), p. 112. Available at: https://doi.org/10.3390/atmos13010112.

Esri (2025) *Overview of georeferencing, ArcGIS Pro Documentation*. Available at: https://pro.arcgis.com/en/pro-app/latest/help/data/imagery/overview-of-georeferencing.htm.

Ester, M. *et al.* (1996) ‘A Density-Based Algorithm for Discovering Clusters in Large Spatial Databases with Noise’, *Comprehensive Chemometrics: Chemical and Biochemical Data Analysis, Second Edition: Four Volume Set* [Preprint]. Available at: https://doi.org/10.1016/B978-0-444-64165-6.03005-6.

Eugenio, F.C. *et al.* (2020) ‘Remotely piloted aircraft systems and forests: a global state of the art and future challenges’, *Canadian Journal of Forest Research*, 50(8), pp. 705–716. Available at: https://doi.org/10.1139/cjfr-2019-0375.

Falkowski, M.J. *et al.* (2005) ‘Characterizing and mapping forest fire fuels using ASTER imagery and gradient modeling’, *Forest Ecology and Management*, 217(2–3), pp. 129–146. Available at: https://doi.org/10.1016/j.foreco.2005.06.013.

Fassnacht, F.E., Latifi, H. and Hartig, F. (2018) ‘Using synthetic data to evaluate the benefits of large field plots for forest biomass estimation with LiDAR’, *Remote Sensing of Environment*, 213, pp. 115–128. Available at: https://doi.org/10.1016/j.rse.2018.05.007.

Feduck, C., McDermid, G.J. and Castilla, G. (2018) ‘Detection of Coniferous Seedlings in UAV Imagery’, *Forests*, 9(7), p. 432. Available at: https://doi.org/10.3390/f9070432.

Fernández-Guisuraga, J.M., Calvo, L. and Suárez-Seoane, S. (2022) ‘Monitoring post-fire neighborhood competition effects on pine saplings under different environmental conditions by means of UAV multispectral data and structure-from-motion photogrammetry’, *Journal of Environmental Management*, 305, p. 114373. Available at: https://doi.org/10.1016/j.jenvman.2021.114373.

Flannigan, M. *et al.* (2009) ‘Impacts of climate change on fire activity and fire management in the circumboreal forest’, *Global Change Biology*, 15(3), pp. 549–560. Available at: https://doi.org/10.1111/j.1365-2486.2008.01660.x.

Fowler, B. (2000) ‘A Sociological Analysis of the Satanic Verses Affair’, *Theory, Culture & Society*, 17(1), pp. 39–61. Available at: https://doi.org/10.1177/02632760022050997.

Franklin, S.E. and Ahmed, O.S. (2018) ‘Deciduous tree species classification using object-based analysis and machine learning with unmanned aerial vehicle multispectral data’, *International Journal of Remote Sensing*, 39(15–16), pp. 5236–5245. Available at:

https://doi.org/10.1080/01431161.2017.1363442.

Gale, M.G. *et al.* (2021) ‘Forest fire fuel through the lens of remote sensing: Review of approaches, challenges and future directions in the remote sensing of biotic determinants of fire behaviour’, *Remote Sensing of Environment*, 255(January), p. 112282. Available at: https://doi.org/10.1016/j.rse.2020.112282.

Gibson, K., Kegley, S. and Bentz, and B. (2009) ‘Mountain Pine Beetle. Forest Insect & Disease Leaflet 2’, *U.S. Department of Agriculture, Forest Service, Pacific Northwest Region. 46 pp*.

Goldbergs, G. *et al.* (2018) ‘Efficiency of Individual Tree Detection Approaches Based on Light-Weight and Low-Cost UAS Imagery in Australian Savannas’, *Remote Sensing*, 10(2), p. 161. Available at: https://doi.org/10.3390/rs10020161.

Goodbody, T.R.H. *et al.* (2017) ‘Unmanned aerial systems for precision forest inventory purposes: A review and case study’, *The Forestry Chronicle*, 93(01), pp. 71–81. Available at: https://doi.org/10.5558/tfc2017-012.

Goodbody, T.R.H. *et al.* (2023) ‘sgsR : a structurally guided sampling toolbox for LiDAR-based forest inventories’, *Forestry*. Edited by F. Fassnacht, 96(4), pp. 411–424. Available at: https://doi.org/10.1093/forestry/cpac055.

GovermentOfCanada (2025) *Indigenous connections, Jasper National Park.* Available at: https://parks.canada.ca/pn-np/ab/jasper/autochtones-indigenous.

Gray, C.A. *et al.* (2021) ‘Spatial and temporal fuels changes in whitebark pine (Pinus albicaulis) from mountain pine beetle (Dendroctonus ponderosae)’, *Forest Ecology and Management*, 482, p. 118789. Available at: https://doi.org/10.1016/j.foreco.2020.118789.

Griffith, D. and Hay, G. (2018) ‘Integrating GEOBIA, Machine Learning, and Volunteered Geographic Information to Map Vegetation over Rooftops’, *ISPRS International Journal of Geo-*

Information, 7(12), p. 462. Available at: https://doi.org/10.3390/ijgi7120462.

Guimarães, N. *et al.* (2020) ‘Forestry Remote Sensing from Unmanned Aerial Vehicles: A Review Focusing on the Data, Processing and Potentialities’, *Remote Sensing*, 12(6), p. 1046. Available at: https://doi.org/10.3390/rs12061046.

Hall, R.J. *et al.* (2016) *Remote sensing of natural disturbance caused by insect defoliation and dieback: a review*. Available at: https://doi.org/10.4095/299044.

Hanes, C.C. *et al.* (2019) ‘Fire-regime changes in Canada over the last half century’, *Canadian Journal of Forest Research*, 49(3), pp. 256–269. Available at: https://doi.org/10.1139/cjfr-2018-0293.

Hartley, R.J.L. *et al.* (2022) ‘A Mixed Methods Approach for Fuel Characterisation in Gorse (Ulex europaeus L.) Scrub from High-Density UAV Laser Scanning Point Clouds and Semantic Segmentation of UAV Imagery’, *Remote Sensing*, 14(19), p. 4775. Available at: https://doi.org/10.3390/rs14194775.

He, L. *et al.* (2023) ‘GFOICP: Geometric Feature Optimized Iterative Closest Point for 3-D Point Cloud Registration’, *IEEE Transactions on Geoscience and Remote Sensing*, 61, pp. 1–17. Available at: https://doi.org/10.1109/TGRS.2023.3317822.

Hicke, J.A. *et al.* (2006) ‘Changing temperatures influence suitability for modeled mountain pine beetle (Dendroctonus ponderosae) outbreaks in the western United States’, *Journal of Geophysical Research: Biogeosciences*, 111(G2). Available at: https://doi.org/10.1029/2005JG000101.

Hoffrén, R., Lamelas, M.T. and de la Riva, J. (2023) ‘UAV-derived photogrammetric point clouds and multispectral indices for fuel estimation in Mediterranean forests’, *Remote Sensing Applications: Society and Environment*, 31, p. 100997. Available at: https://doi.org/10.1016/j.rsase.2023.100997.

Hollis, J.J. *et al.* (2025) ‘An efficient and comprehensive field protocol for assessing fuel characteristics for fire behaviour modelling in Australian open forests’, *MethodsX*, p. 103345. Available at: https://doi.org/10.1016/j.mex.2025.103345.

Hopkinson, C. *et al.* (2004) ‘Assessing forest metrics with a ground-based scanning lidar’, *Canadian Journal of Forest Research*, 34(3), pp. 573–583. Available at: https://doi.org/10.1139/x03-225.

Hopkinson, C. *et al.* (2005) ‘Vegetation class dependent errors in lidar ground elevation and canopy height estimates in a boreal wetland environment’, *Canadian Journal of Remote Sensing*, 31(2), pp. 191–206. Available at: https://doi.org/10.5589/m05-007.

Hopkinson, C. (2006) *An overview of airborne laser scanning technology*. Available at: http://agrg.cogs.nscc.ca/publications/hydroscan_book%5Cnhttp://www.cwra.org/branches/cshs/assets/Hydroscan.pdf.

Iglhaut, J. *et al.* (2019) ‘Structure from Motion Photogrammetry in Forestry: a Review’, *Current Forestry Reports*, 5(3), pp. 155–168. Available at: https://doi.org/10.1007/s40725-019-00094-3.

Ireland, A.W. *et al.* (2021) ‘Field experiment demonstrates the potential utility of satellite-derived reflectance indices for monitoring regeneration of boreal forest communities’, *Trees, Forests and People*, 6, p. 100145. Available at: https://doi.org/10.1016/j.tfp.2021.100145.

Jain, P. *et al.* (2020) ‘A review of machine learning applications in wildfire science and management’, *Environmental Reviews*, 28(4), pp. 478–505. Available at: https://doi.org/10.1139/er-2020-0019.

James-Abra, E. (2011) ‘Jasper National Park’. Available at: https://www.thecanadianencyclopedia.ca/en/article/jasper-national-park.

Jarron, L.R. *et al.* (2021) ‘Detection and Quantification of Coarse Woody Debris in Natural Forest Stands Using Airborne LiDAR’, *Forest Science*, 67(5), pp. 550–563. Available at: https://doi.org/10.1093/forsci/fxab023.

Jenkins, M.J. *et al.* (2014) ‘Interactions among the Mountain Pine Beetle, Fires, and Fuels’, *Forest Science*, 60(3), pp. 489–501. Available at: https://doi.org/10.5849/forsci.13-017.
Johnston, L.M. *et al.* (2020) ‘Wildland fire risk research in Canada’, *Environmental Reviews*, 28(2), pp. 164–186. Available at: https://doi.org/10.1139/er-2019-0046.

Jolly, W.M. *et al.* (2012) ‘Relationships between moisture, chemistry, and ignition of Pinus contorta needles during the early stages of mountain pine beetle attack’, *Forest Ecology and Management*, 269, pp. 52–59. Available at: https://doi.org/10.1016/j.foreco.2011.12.022.

Kavzoglu, T. and Tonbul, H. (2017) ‘A comparative study of segmentation quality for multi-resolution segmentation and watershed transform’, in *2017 8th International Conference on Recent Advances in Space Technologies (RAST)*. IEEE, pp. 113–117. Available at: https://doi.org/10.1109/RAST.2017.8002984.

Keane, R.E., Burgan, R. and van Wagtendonk, J. (2001) ‘Mapping wildland fuels for fire management across multiple scales: Integrating remote sensing, GIS, and biophysical modeling’, *International Journal of Wildland Fire*, 10(4), p. 301. Available at: https://doi.org/10.1071/WF01028.

Klutsch, J.G. *et al.* (2009) ‘Stand characteristics and downed woody debris accumulations associated with a mountain pine beetle (Dendroctonus ponderosae Hopkins) outbreak in Colorado’, *Forest Ecology and Management*, 258(5), pp. 641–649. Available at: https://doi.org/10.1016/j.foreco.2009.04.034.

Korhonen, L. *et al.* (2017) ‘Comparison of Sentinel-2 and Landsat 8 in the estimation of boreal forest canopy cover and leaf area index’, *Remote Sensing of Environment*, 195, pp. 259–274. Available at: https://doi.org/10.1016/j.rse.2017.03.021.

Kulshreshtha, S.N. *et al.* (2000) *Carbon Sequestration In Protected Areas Of Canada : An Economic Valuation, Dept. of Agricultural Economics, University of Saskatchewan*.

Kutner, M.H. (1983) *Applied linear regression models*. Edited by Emory University. Available at: https://users.stat.ufl.edu/~winner/sta4211/ALSM_5Ed_Kutner.pdf.

de la Giroday, H.C., Carroll, A.L. and Aukema, B.H. (2012) 'Breach of the northern Rocky Mountain geoclimatic barrier: initiation of range expansion by the mountain pine beetle', *Journal of Biogeography*, 39(6), pp. 1112–1123. Available at: https://doi.org/10.1111/j.1365-2699.2011.02673.x.

Lambert, M.-C., Ung, C.-H. and Raulier, F. (2005) 'Canadian national tree aboveground biomass equations', *Canadian Journal of Forest Research*, 35(8), pp. 1996–2018. Available at: https://doi.org/10.1139/x05-112.

Lawson, C.L. (1977) 'Software for C1 Surface Interpolation', in *Mathematical Software*. Elsevier, pp. 161–194. Available at: https://doi.org/10.1016/B978-0-12-587260-7.50011-X.

Lefsky, M.A. *et al.* (1999) 'Lidar Remote Sensing of the Canopy Structure and Biophysical Properties of Douglas-Fir Western Hemlock Forests', *Remote Sensing of Environment*, 70(3), pp. 339–361. Available at: https://doi.org/10.1016/S0034-4257(99)00052-8.

Lefsky, M.A. *et al.* (2005) 'Combining lidar estimates of aboveground biomass and Landsat estimates of stand age for spatially extensive validation of modeled forest productivity', *Remote Sensing of Environment*, 95(4), pp. 549–558. Available at: https://doi.org/10.1016/j.rse.2004.12.022.

Li, P. *et al.* (2020) 'Evaluation of the ICP Algorithm in 3D Point Cloud Registration', *IEEE Access*, 8, pp. 68030–68048. Available at: https://doi.org/10.1109/ACCESS.2020.2986470.

Li, S. *et al.* (2022) 'VPRNet: Virtual Points Registration Network for Partial-to-Partial Point Cloud Registration', *Remote Sensing*, 14(11), p. 2559. Available at:

https://doi.org/10.3390/rs14112559.

Li, W. *et al.* (2012) ‘A New Method for Segmenting Individual Trees from the Lidar Point Cloud’, *Photogrammetric Engineering & Remote Sensing*, 78(1), pp. 75–84. Available at: https://doi.org/10.14358/PERS.78.1.75.

Liu, X. *et al.* (2022) ‘Accuracy Assessment of a UAV Direct Georeferencing Method and Impact of the Configuration of Ground Control Points’, *Drones*, 6(2), p. 30. Available at: https://doi.org/10.3390/drones6020030.

Logan, J.A., Macfarlane, W.W. and Willcox, L. (2010) ‘Whitebark pine vulnerability to climate-driven mountain pine beetle disturbance in the Greater Yellowstone Ecosystem’, *Ecological Applications*, 20(4), pp. 895–902. Available at: https://doi.org/10.1890/09-0655.1.

Lopes Queiroz, G. *et al.* (2019) ‘Mapping Coarse Woody Debris with Random Forest Classification of Centimetric Aerial Imagery’, *Forests*, 10(6), p. 471. Available at: https://doi.org/10.3390/f10060471.

Lopes Queiroz, G. *et al.* (2020) ‘Estimating Coarse Woody Debris Volume Using Image Analysis and Multispectral LiDAR’, *Forests*, 11(2), p. 141. Available at: https://doi.org/10.3390/f11020141.

Loudermilk, E.L. *et al.* (2022) ‘Vegetation’s influence on fire behavior goes beyond just being fuel’, *Fire Ecology*, 18(1), p. 9. Available at: https://doi.org/10.1186/s42408-022-00132-9.

De Luca, G. *et al.* (2019) ‘Object-Based Land Cover Classification of Cork Oak Woodlands using UAV Imagery and Orfeo ToolBox’, *Remote Sensing*, 11(10), p. 1238. Available at: https://doi.org/10.3390/rs11101238.

Maiseli, B., Gu, Y. and Gao, H. (2017) ‘Recent developments and trends in point set registration methods’, *Journal of Visual Communication and Image Representation*, 46, pp. 95–106.

Available at: https://doi.org/10.1016/j.jvcir.2017.03.012.

Mansor, N.S. *et al.* (2024) ‘Support Vector Machine for Satellite Images Classification Using Radial Basis Function Kernel Method’, in, pp. 301–312. Available at: https://doi.org/10.1007/978-981-99-9589-9_23.

Mao, Z. *et al.* (2021) ‘Precision Evaluation and Fusion of Topographic Data Based on UAVs and TLS Surveys of a Loess Landslide’, *Frontiers in Earth Science*, 9(December), pp. 1–15. Available at: https://doi.org/10.3389/feart.2021.801293.

Mason (1915) *The Life History of Lodgepole Pine in the Rocky Mountains, U.S. Department of Agriculture, Forest Service.*

Matasci, G. *et al.* (2018) ‘Large-area mapping of Canadian boreal forest cover, height, biomass and other structural attributes using Landsat composites and lidar plots’, *Remote Sensing of Environment*, 209, pp. 90–106. Available at: https://doi.org/10.1016/j.rse.2017.12.020.

Ming, D. *et al.* (2018) ‘Coupling Relationship Among Scale Parameter, Segmentation Accuracy, and Classification Accuracy In GeOBIA’, *Photogrammetric Engineering & Remote Sensing*, 84(11), pp. 681–693. Available at: https://doi.org/10.14358/PERS.84.11.681.

Mitton, J.B. and Ferrenberg, S.M. (2012) ‘Mountain pine beetle develops an unprecedented summer generation in response to climate warming’, *American Naturalist*, 179(5). Available at: https://doi.org/10.1086/665007.

Motha, R.P. and Baier, W. (2005) ‘Impacts of Present and Future Climate Change and Climate Variability on Agriculture in the Temperate Regions: North America’, *Climatic Change*, 70(1–2), pp. 137–164. Available at: https://doi.org/10.1007/s10584-005-5940-1.

Natesan, S., Armenakis, C. and Vepakomma, U. (2020) ‘Individual tree species identification using Dense Convolutional Network (DenseNet) on multitemporal RGB images from UAV’, *Journal of Unmanned Vehicle Systems*, 8(4), pp. 310–333. Available at: https://doi.org/10.1139/juvs-2020-0014.

Natural Resources Canada (2022) *The State of Canada's Forests: Annual Report 2022.* Available at: https://natural-resources.canada.ca/sites/nrcan/files/forest/sof2022/SoF_Annual2022_EN_access.pdf.

Nevalainen, O. *et al.* (2017) 'Individual Tree Detection and Classification with UAV-Based Photogrammetric Point Clouds and Hyperspectral Imaging', *Remote Sensing*, 9(3), p. 185. Available at: https://doi.org/10.3390/rs9030185.

Nitze, I., Schulthess, U., & Asche, H. (2012) 'omparison of Machine Learning Algorithms Random Forest , Artificial Neural Network and Support Vector Machine', in *Proceedings of the 4th GEOBIA*. Rio de Janeiro, Brazil, pp. 35–40.

Nuijten, R.J.G. *et al.* (2024) 'Estimation of fine-scale vegetation distribution information from RPAS-generated imagery and structure to aid restoration monitoring', *Science of Remote Sensing*, 9, p. 100114. Available at: https://doi.org/10.1016/j.srs.2023.100114.

Nunes Miranda, E. *et al.* (2022) 'Variable selection for estimating individual tree height using genetic algorithm and random forest', *Forest Ecology and Management*, 504, p. 119828. Available at: https://doi.org/10.1016/j.foreco.2021.119828.

O'Neill, N.A. (2011) *Transboundary Regional Planning Collaboration for Climate Change Adaptation: A Case Study of Jasper National Park, Mount Robson Provincial Park, and Willmore Wilderness Park*.

Padró, J.-C. *et al.* (2019) 'Comparison of four UAV georeferencing methods for environmental monitoring purposes focusing on the combined use with airborne and satellite remote sensing platforms', *International Journal of Applied Earth Observation and Geoinformation*, 75, pp. 130–140. Available at: https://doi.org/10.1016/j.jag.2018.10.018.

Page, W.G., Jenkins, M.J. and Alexander, M.E. (2013) ‘Foliar moisture content variations in lodgepole pine over the diurnal cycle during the red stage of mountain pine beetle attack’, *Environmental Modelling & Software*, 49, pp. 98–102. Available at: https://doi.org/10.1016/j.envsoft.2013.08.001.

Palaiologou, P., Kalabokidis, K. and Kyriakidis, P. (2013) ‘Forest mapping by geoinformatics for landscape fire behaviour modelling in coastal forests, Greece’, *International Journal of Remote Sensing*, 34(12), pp. 4466–4490. Available at: https://doi.org/10.1080/01431161.2013.779399.

Pearse, B.E.N. (2024) *Monitoring vegetation regeneration using multiple remotely piloted aircraft system sensors and methodologies*, University of Lethbridge.

Peng, C., Zhang, L. and Liu, J. (2001) ‘Developing and Validating Nonlinear Height–Diameter Models for Major Tree Species of Ontario’s Boreal Forests’, *Northern Journal of Applied Forestry*, 18(3), pp. 87–94. Available at: https://doi.org/10.1093/njaf/18.3.87.

Perrakis, D.D.B. *et al.* (2014) ‘Modeling Wildfire Spread in Mountain Pine Beetle-Affected Forest Stands, British Columbia, Canada’, *Fire Ecology*, 10(2), pp. 10–35. Available at: https://doi.org/10.4996/fireecology.1002010.

Persad, R.A. *et al.* (2017) ‘Automatic integration of 3-D point clouds from UAS and airborne LiDAR platforms’, *Journal of Unmanned Vehicle Systems*, p. juvs-2016-0034. Available at: https://doi.org/10.1139/juvs-2016-0034.

Phelps, N. *et al.* (2022a) ‘The Alberta Wildland Fuels Inventory Program (AWFIP): data description and reference tables’, *Annals of Forest Science*, 79(1), pp. 1–16. Available at: https://doi.org/10.1186/s13595-022-01144-w.

Phelps, N. *et al.* (2022b) ‘The Alberta Wildland Fuels Inventory Program (AWFIP): data description and reference tables’, *Annals of Forest Science*, 79(1), p. 28. Available at: https://doi.org/10.1186/s13595-022-01144-w.

Pimont, F. *et al.* (2016) ‘Modeling fuels and fire effects in 3D: Model description and applications’, *Environmental Modelling & Software*, 80, pp. 225–244. Available at: https://doi.org/10.1016/j.envsoft.2016.03.003.

Prescott, C.E. *et al.* (2000) ‘Decomposition of broadleaf and needle litter in forests of British Columbia: influences of litter type, forest type, and litter mixtures’, *Canadian Journal of Forest Research*, 30(11), pp. 1742–1750. Available at: https://doi.org/10.1139/x00-097.

Price, D.T. *et al.* (2013) ‘Anticipating the consequences of climate change for Canada’s boreal forest ecosystems’, *Environmental Reviews*, 21(4), pp. 322–365. Available at: https://doi.org/10.1139/er-2013-0042.

Proulx, R. (2021) ‘On the general relationship between plant height and aboveground biomass of vegetation stands in contrasted ecosystems’, *PLOS ONE*. Edited by M. Bosela, 16(5), p. e0252080. Available at: https://doi.org/10.1371/journal.pone.0252080.

Puliti, S., Breidenbach, J. and Astrup, R. (2020) ‘Estimation of Forest Growing Stock Volume with UAV Laser Scanning Data: Can It Be Done without Field Data?’, *Remote Sensing*, 12(8), p. 1245. Available at: https://doi.org/10.3390/rs12081245.

Qi, Y. *et al.* (2022) ‘Assessing the effects of burn severity on post-fire tree structures using the fused drone and mobile laser scanning point clouds’, *Frontiers in Environmental Science*, pp. 1–20. Available at: https://doi.org/10.3389/fenvs.2022.949442.

Rhemtulla, J.M. *et al.* (2002) ‘Eighty years of change: Vegetation in the montane ecoregion of Jasper National Park, Alberta, Canada’, *Canadian Journal of Forest Research*, 32(11), pp. 2010–2021. Available at: https://doi.org/10.1139/x02-112.

Roberti, G. *et al.* (2021) ‘Structure from motion used to revive archived aerial photographs for geomorphological analysis: an example from Mount Meager volcano, British Columbia, Canada’, *Canadian Journal of Earth Sciences*, 58(12), pp. 1253–1267. Available at: https://doi.org/10.1139/cjes-2020-0140.

Robertson, C. *et al.* (2009) ‘Spatial–temporal analysis of species range expansion: the case of the mountain pine beetle, Dendroctonus ponderosae’, *Journal of Biogeography*, 36(8), pp. 1446–1458. Available at: https://doi.org/10.1111/j.1365-2699.2009.02100.x.

Robinson, D.J., Redding, N.J., & Crisp, D.J. (2002) ‘Implementation of a fast algorithm for segmenting SAR imagery’, *Engineering, Environmental Science, Computer Science* [Preprint]. Available at: https://www.semanticscholar.org/paper/Implementation-of-a-Fast-Algorithm-for-Segmenting-Robinson-Redding/c6dde80055fb57d492797604864e9b2e2f4ce43b.

Rodney W. Sando, C.H.W. (1972) ‘A method of evaluating crown fuels in forest stands’.
La Roi, G.H. and Hnatiuk, R.J. (1980) ‘The Pinus Contorta Forests of Banff and Jasper National Parks: A Study in Comparative Synecology and Syntaxonomy’, *Ecological Monographs*, 50(1), pp. 1–29. Available at: https://doi.org/10.2307/2937244.

Rollins, R. (2012) ‘Manufacturing National Park Nature: Photography Ecology, and the Wilderness Industry of Jasper’, *Northwest Science*, 86(3), pp. 230–233. Available at: https://doi.org/10.3955/046.086.0308.

Romualdi, D.C., Wilkinson, S.L. and James, P.M.A. (2023) ‘On the limited consensus of mountain pine beetle impacts on wildfire’, *Landscape Ecology*, 38(9), pp. 2159–2178. Available at: https://doi.org/10.1007/s10980-023-01720-z.

Saatchi, S. *et al.* (2007) ‘Estimation of Forest Fuel Load From Radar Remote Sensing’, *IEEE Transactions on Geoscience and Remote Sensing*, 45(6), pp. 1726–1740. Available at: https://doi.org/10.1109/TGRS.2006.887002.

Safranyik, L. and Wilson, B. (2006) *The mountain pine beetle: a synthesis of biology, management, and impacts on lodgepole pine.*, *The mountain pine beetle: A synthesis of biology, management, and impacts on lodgepole pine*. Natural Resources Canada, Canadian Forest Service, Pacific Forestry Centre, Victoria, British Columbia. Available at: http://www.cfs.nrcan.gc.ca/pubwarehouse/pdfs/26116.pdf#page=106.

Sambaraju, K.R. *et al.* (2012) 'Climate change could alter the distribution of mountain pine beetle outbreaks in western Canada', *Ecography*, 35(3), pp. 211–223. Available at: https://doi.org/10.1111/j.1600-0587.2011.06847.x.

Sang, M., Wang, W. and Pan, Y. (2022) 'RGB-ICP Method to Calculate Ground Three-Dimensional Deformation Based on Point Cloud from Airborne LiDAR', *Remote Sensing*, 14(19), p. 4851. Available at: https://doi.org/10.3390/rs14194851.

Schoennagel, T. *et al.* (2012) 'Effects of Mountain Pine Beetle on Fuels and Expected Fire Behavior in Lodgepole Pine Forests, Colorado, USA', *PLoS ONE*. Edited by H.Y.H. Chen, 7(1), p. e30002. Available at: https://doi.org/10.1371/journal.pone.0030002.

Serbouti, I. *et al.* (2021) 'Pixel and Object-Based Machine Learning Classification Schemes for Lithological Mapping Enhancement of Semi-Arid Regions Using Sentinel-2A Imagery: A Case Study of the Southern Moroccan Meseta', *IEEE Access*, 9, pp. 119262–119278. Available at: https://doi.org/10.1109/ACCESS.2021.3107294.

Sheykhmousa, M. *et al.* (2020) 'Support Vector Machine Versus Random Forest for Remote Sensing Image Classification: A Meta-Analysis and Systematic Review', *IEEE Journal of Selected Topics in Applied Earth Observations and Remote Sensing*, 13, pp. 6308–6325. Available at: https://doi.org/10.1109/JSTARS.2020.3026724.

Shin, P. *et al.* (2018) 'Evaluating unmanned aerial vehicle images for estimating forest canopy fuels in a ponderosa pine stand', *Remote Sensing*, 10(8), pp. 3–5. Available at: https://doi.org/10.3390/rs10081266.

Šiljeg, A. *et al.* (2022) ‘Comparative Assessment of Pixel and Object-Based Approaches for Mapping of Olive Tree Crowns Based on UAV Multispectral Imagery’, *Remote Sensing*, 14(3), p. 757. Available at: https://doi.org/10.3390/rs14030757.

Simard, M. *et al.* (2011) ‘Do mountain pine beetle outbreaks change the probability of active crown fire in lodgepole pine forests?’, *Ecological Monographs*, 81(1), pp. 3–24. Available at: https://doi.org/10.1890/10-1176.1.

Skowronski, N.S., Gallagher, M.R. and Warner, T.A. (2020) ‘Decomposing the Interactions between Fire Severity and Canopy Fuel Structure Using Multi-Temporal, Active, and Passive Remote Sensing Approaches’, *Fire*, 3(1), p. 7. Available at: https://doi.org/10.3390/fire3010007.

Sotille, M.E. *et al.* (2022) ‘UAV-based classification of maritime Antarctic vegetation types using GEOBIA and random forest’, *Ecological Informatics*, 71, p. 101768. Available at: https://doi.org/10.1016/j.ecoinf.2022.101768.

Stueve, K.M. *et al.* (2009) ‘Post-fire tree establishment patterns at the alpine treeline ecotone: Mount Rainier National Park, Washington, USA’, *Journal of Vegetation Science*, 20(1), pp. 107–120. Available at: https://doi.org/10.1111/j.1654-1103.2009.05437.x.

Talucci, A.C. and Krawchuk, M.A. (2019) ‘Dead forests burning: the influence of beetle outbreaks on fire severity and legacy structure in sub-boreal forests’, *Ecosphere*, 10(5). Available at: https://doi.org/10.1002/ecs2.2744.

Tang, L. and Shao, G. (2015) ‘Drone remote sensing for forestry research and practices’, *Journal of Forestry Research*, 26(4), pp. 791–797. Available at: https://doi.org/10.1007/s11676-015-0088-y.

Tinkham, W.T. and Swayze, N.C. (2021) ‘Influence of Agisoft Metashape Parameters on UAS Structure from Motion Individual Tree Detection from Canopy Height Models’, *Forests*, 12(2),

p. 250. Available at: https://doi.org/10.3390/f12020250.

Le Toan, T. *et al.* (1992) ‘Relating forest biomass to SAR data’, *IEEE Transactions on Geoscience and Remote Sensing*, 30(2), pp. 403–411. Available at: https://doi.org/10.1109/36.134089.

Tondewad, M.P.S. and Dale, M.M.P. (2020) ‘Remote Sensing Image Registration Methodology: Review and Discussion’, *Procedia Computer Science*, 171, pp. 2390–2399. Available at: https://doi.org/10.1016/j.procs.2020.04.259.

Ung, C.-H., Bernier, P. and Guo, X.-J. (2008) ‘Canadian national biomass equations: new parameter estimates that include British Columbia data’, *Canadian Journal of Forest Research*, 38(5), pp. 1123–1132. Available at: https://doi.org/10.1139/X07-224.

Vastaranta, M. *et al.* (2012) ‘Combination of individual tree detection and area-based approach in imputation of forest variables using airborne laser data’, *ISPRS Journal of Photogrammetry and Remote Sensing*, 67, pp. 73–79. Available at: https://doi.org/10.1016/j.isprsjprs.2011.10.006.
Wallace, L. *et al.* (2012) ‘Development of a UAV-LiDAR System with Application to Forest Inventory’, *Remote Sensing*, 4(6), pp. 1519–1543. Available at: https://doi.org/10.3390/rs4061519.

Wallace, L. *et al.* (2016) ‘Assessment of Forest Structure Using Two UAV Techniques: A Comparison of Airborne Laser Scanning and Structure from Motion (SfM) Point Clouds’, *Forests*, 7(12), p. 62. Available at: https://doi.org/10.3390/f7030062.

Wang, E. *et al.* (2024) ‘Experimental Study on Effects of Moisture Content and Tree Height on Crown Fire Behaviors of Live Cypress Trees’, *Combustion Science and Technology*, pp. 1–16. Available at: https://doi.org/10.1080/00102202.2024.2323576.

Wang, Y. and Anderson, K.R. (2010) ‘An evaluation of spatial and temporal patterns of lightning- and human-caused forest fires in Alberta, Canada, 1980 - 2007’, *International Journal* *of Wildland Fire*, 19(8), p. 1059. Available at: https://doi.org/10.1071/WF09085.

Wehr, A. and Lohr, U. (1999) ‘Airborne laser scanning—an introduction and overview’, *ISPRS Journal of Photogrammetry and Remote Sensing*, 54(2–3), pp. 68–82. Available at: https://doi.org/10.1016/S0924-2716(99)00011-8.

Weinmann, M. *et al.* (2015) ‘Semantic point cloud interpretation based on optimal neighborhoods, relevant features and efficient classifiers’, *ISPRS Journal of Photogrammetry and Remote Sensing*, 105, pp. 286–304. Available at: https://doi.org/10.1016/j.isprsjprs.2015.01.016.

Westoby, M.J. *et al.* (2012) ‘“Structure-from-Motion” photogrammetry: A low-cost, effective tool for geoscience applications’, *Geomorphology*, 179, pp. 300–314. Available at: https://doi.org/10.1016/j.geomorph.2012.08.021.

White, J.C. *et al.* (2013) ‘A best practices guide for generating forest inventory attributes from airborne laser scanning data using an area-based approach’, *The Forestry Chronicle*, 89(06), pp. 722–723. Available at: https://doi.org/10.5558/tfc2013-132.

White, J.C. *et al.* (2017) ‘A nationwide annual characterization of 25 years of forest disturbance and recovery for Canada using Landsat time series’, *Remote Sensing of Environment*, 194, pp. 303–321. Available at: https://doi.org/10.1016/j.rse.2017.03.035.

Whiteside, T.G., Boggs, G.S. and Maier, S.W. (2011) ‘Comparing object-based and pixel-based classifications for mapping savannas’, *International Journal of Applied Earth Observation and Geoinformation*, 13(6), pp. 884–893. Available at: https://doi.org/10.1016/j.jag.2011.06.008.

Wulder, M.A. *et al.* (2006) ‘Estimating the probability of mountain pine beetle red-attack damage’, *Remote Sensing of Environment*, 101(2), pp. 150–166. Available at: https://doi.org/10.1016/j.rse.2005.12.010.

Wulder, Michael A. *et al.* (2006) ‘Surveying mountain pine beetle damage of forests: A review of remote sensing opportunities’, *Forest Ecology and Management*, 221(1–3), pp. 27–41. Available at: https://doi.org/10.1016/j.foreco.2005.09.021.

Xi, Z. and Hopkinson, C. (2022) ‘3D Graph-Based Individual-Tree Isolation (Treeiso) from Terrestrial Laser Scanning Point Clouds’, *Remote Sensing*, 14(23), p. 6116. Available at: https://doi.org/10.3390/rs14236116.

Xu, Z., Shen, X. and Cao, L. (2023) ‘Extraction of Forest Structural Parameters by the Comparison of Structure from Motion (SfM) and Backpack Laser Scanning (BLS) Point Clouds’, *Remote Sensing*, 15(8), p. 2144. Available at: https://doi.org/10.3390/rs15082144.

Yang, J. *et al.* (2016) ‘Go-ICP: A Globally Optimal Solution to 3D ICP Point-Set Registration’, *IEEE Transactions on Pattern Analysis and Machine Intelligence*, 38(11), pp. 2241–2254. Available at: https://doi.org/10.1109/TPAMI.2015.2513405.

Ye, S., Pontius, R.G. and Rakshit, R. (2018) ‘A review of accuracy assessment for object-based image analysis: From per-pixel to per-polygon approaches’, *ISPRS Journal of Photogrammetry and Remote Sensing*, 141, pp. 137–147. Available at: https://doi.org/10.1016/j.isprsjprs.2018.04.002.

Yu, X. *et al.* (2010) ‘Comparison of Area-Based and Individual Tree-Based Methods for Predicting Plot-Level Forest Attributes’, *Remote Sensing*, 2(6), pp. 1481–1495. Available at: https://doi.org/10.3390/rs2061481.

Zhan, Q. *et al.* (2005) ‘Quality assessment for geo-spatial objects derived from remotely sensed data’, *International Journal of Remote Sensing*, 26(14), pp. 2953–2974. Available at: https://doi.org/10.1080/01431160500057764.

Zhang, H. *et al.* (2021) ‘Mapping Canopy Heights in Dense Tropical Forests Using Low-Cost UAV-Derived Photogrammetric Point Clouds and Machine Learning Approaches’, *Remote*

Sensing, 13(18), p. 3777. Available at: https://doi.org/10.3390/rs13183777.

Zhang, W. *et al.* (2016) ‘An Easy-to-Use Airborne LiDAR Data Filtering Method Based on Cloth Simulation’, *Remote Sensing*, 8(6), p. 501. Available at: https://doi.org/10.3390/rs8060501.

Zhang, X., Glennie, C. and Kusari, A. (2015) ‘Change Detection From Differential Airborne LiDAR Using a Weighted Anisotropic Iterative Closest Point Algorithm’, *IEEE Journal of Selected Topics in Applied Earth Observations and Remote Sensing*, 8(7), pp. 3338–3346. Available at: https://doi.org/10.1109/JSTARS.2015.2398317.

Appendix 1: Scripts

Tain Support Vector Machine Algorithm (Point-Based Classification)

```
clear all
format long g
clc
close all
% Load train data
TrainData = load('TrainMore.txt');

Attributes= TrainData(:,7:14);
Classes= TrainData(:,15);

svmModel = fitcsvm(Attributes, Classes);
save('svm_classifier2.mat', 'svmModel');
```

Apply Support Vector Machine algorithm (Point-Based cClassification)

```
clear all
clc
% Load the classifier
load('svm_classifier.mat');
REMOTELY PILOTED AIRCRAFT SYSTEMPoints=load("REMOTELY PILOTED AIRCRAFT SYSTEM1.txt");
% Seprate geometric features
REMOTELY PILOTED AIRCRAFT SYSTEMAttributes= REMOTELY PILOTED AIRCRAFT
SYSTEMPoints(:,7:13);
predictedLabels = predict(svmModel, REMOTELY PILOTED AIRCRAFT SYSTEMAttributes);
XYZ=REMOTELY PILOTED AIRCRAFT SYSTEMPoints(:,1:3);
% Create a new classified point cloud
ClassifyREMOTELY PILOTED AIRCRAFT SYSTEM= pointCloud(XYZ, Intensity=predictedLabels);
pcwrite(ClassifyREMOTELY PILOTED AIRCRAFT SYSTEM,'StemSVM.ply','Encoding','binary');
```

Modify Individual Tree Detection using DBSCAN

```
clc
clear
% Import the number of trees identified using TreeIso

N=input('Please Enter the Number of Trees=');

% Each loop reads the results of TreeIso (exported from CloudCompare as .txt) and
applies DBSCAN to separate close trees.

for i=1:N
```

```
    PC = sprintf('%d.txt',i);
    A = load(PointCloud);
    XYZTotal=A(:,1:3);
    Classes=A(:,7);
    PC2 = pointCloud(XYZTotal, "Intensity", Classes);
    epsilon = 0.60;
    minPts = 20;
    idx = dbscan(XYZTotal, epsilon, minPts);
    Trees=unique(idx);
    NumberOfTrees = size (unique(idx), 1);
    ALLPoints= [XYZTotal Classes idx];

         for j=1:NumberOfTrees

              FF=Trees(j);
              rows = ALLPoints(:, 5) == FF;

              resulting_rows = ALLPoints(rows, :);
              XYZsmall=resulting_rows(:,1:3);
              Classes2=resulting_rows(:,4);

              Result= pointCloud (XYZsmall,'Intensity',Classes2);
              pcFileName = sprintf('PointCloud_%d.ply', i,j);
              pcwrite(Result, pcFileName);
         end
end
```

Tree Metrics Required for Fuel Mmodeling:

```
clc
clear
close all
format long

%Import the number of trees identified using TreeIso+DBSCAN

N=input('Please Enter the Number of Trees=');

%Import airborne lidar ground points
ALSGround= pcread("ALS.ply");

Report=[];
for i=1:N
    PC = sprintf('%d.txt',i);
    A = load(PC);
    XYZTotal=A(:,1:3);
    Classes=A(:,4);
    KOl=[XYZTotal Classes];

     FF=XYZTotal;
     FE=Classes;
```

```
     A=[FF FE];


   % Separate Stem and Foliage Points

    ind1 = A(:,4) == 1;
    ind2 = A(:,4) == 0;

    Stem = A(ind1,:);
    StemXYZ= Stem(:, 1:3);
    StemClass= Stem(:, 4);
    Stem=[StemXYZ, StemClass];
    NumberOfStemPoints = size(Stem,1);

    Foliage = A(ind2,:);
    FoliageXYZ= Foliage(:, 1:3);
    FoliageClass= Foliage(:, 4);
    Foliage= [FoliageXYZ, FoliageClass];
    NumberOfFoliagePoints = size(Foliage,1);
    NumKol=NumberOfStemPoints+NumberOfFoliagePoints;

    % Remove noises and small components that are identified as trees

    if NumKol < 1000
        continue
    end

     % Generate point cloud Just XYZ and Classes

    Kol=[Stem; Foliage];
    PcKol = pointCloud(Kol(:,1:3),"Intensity", Kol(:,4));



      % Find the center of the trees

    X=median(Kol(:,1));
    Y=median(Kol(:,2));
    Z=median(Kol(:,3));


      % Find tree height and the location of tree height of each tree (X, Y)

    RowOfMaxElevation= max(Kol, [], 1);
    MaxElevation= RowOfMaxElevation(3);
    rowsOfmax = any(Kol == MaxElevation, 2);
    matchingRows = Kol(rowsOfmax, :);
    XHeight=matchingRows(1,1);
    YHeight=matchingRows(1,2);
    ZHeight=matchingRows(1,3);
    ROIALS = [(XHeight-0.15) (XHeight+0.15) (YHeight-0.15) (YHeight+0.15) (ZHeight-
40) (ZHeight+40)];
    indices = findPointsInROI(ALSGround,ROIALS);
    ALSTreeG = select(ALSGround,indices);
    ZGround= ALSTreeG.Location(:,3);
```

```
MeanZALSGround=mean(ZGround);
MinZALSGround=min(ZGround);
MaxZALSGround=max(ZGround);
Height= MaxElevation-MeanZALSGround;

                     % Measuring canopy base height (CANOPY BASE HEIGHT)

                     RatioOfStem = (NumberOfStemPoints/NumKol)*100;
                     RatioOfFoliage = (NumberOfFoliagePoints/NumKol)*100;



if  RatioOfFoliage >= 98.00     %  Without Stem
    CANOPY BASE HEIGHT= min( Foliage(:,3))-MeanZALSGround;
    CANOPY BASE HEIGHTELEVATION = min( Foliage(:,3));
    CANOPY BASE HEIGHTall= Foliage(:,3);
elseif RatioOfStem >= 98.00  %  Snag
    CANOPY BASE HEIGHT= Height;
    CANOPY BASE HEIGHTELEVATION = MaxElevation;
    CANOPY BASE HEIGHTall= 50000;
else  %  Otherwise (normal trees with enough stem and foliage)

              VoxelZsize = 0.50;
              MinX=min(Kol(:,1)); MaxX=max(Kol(:,1));
              MinY=min(Kol(:,2)); MaxY=max(Kol(:,2));
              MinZ=min(Kol(:,3)); MaxZ=max(Kol(:,3));

              NumberofVexelZ= floor((MaxZ-MinZ)/VoxelZsize +1);

              for x=0:NumberofVexelZ

                           roi2 = [MinX MaxX MinY MaxY MinZ (MinZ+VoxelZsize)];
                           indices = findPointsInROI(PcKol,roi2);
                           Voxel = select(PcKol,indices);
                                      LocationVoxel=Voxel.Location;
                                      Class = Voxel.Intensity;
                                      KolVoxel = [LocationVoxel Class];
                                      TotalROI1 = size(KolVoxel,1);
                                      ind3 = KolVoxel(:,4) == 1;
                                      indF = KolVoxel(:,4) == 0;
                                      StemVoxel1 = KolVoxel(ind3,:);
                                      FoliageVoxel1 = KolVoxel(indF,:);
                                      NumberofStemVoxel1 = size(StemVoxel1,1);
                 NumberofFoliageVoxel1 = size(FoliageVoxel1,1);
          StemRatio = (NumberofStemVoxel1/NumberofFoliageVoxel1)*100;
          roi3 = [MinX MaxX MinY MaxY (MinZ+VoxelZsize) (MinZ+2*VoxelZsize)];
                                      indices2 = findPointsInROI(PcKol,roi3);
                                      Voxel = select(PcKol,indices2);
                                      LocationVoxel=Voxel.Location;
                                      Class = Voxel.Intensity;
                                      KolVoxel = [LocationVoxel Class];
                                      TotalROI2 = size(KolVoxel,1);
                                      ind3 = KolVoxel(:,4) == 1;
                                      indF = KolVoxel(:,4) == 0;
                                      StemVoxel2 = KolVoxel(ind3,:);
```

```
                                          FoliageVoxel2 = KolVoxel(indF,:);
                                          NumberofStemVoxel2 = size(StemVoxel2,1);
                                    NumberofFoliageVoxel2 = size(FoliageVoxel2,1);
                 FoliageRatio = (NumberofFoliageVoxel2/NumberofStemVoxel2)*100;

                                         if StemRatio>=75 &&  FoliageRatio>=75
                                             CANOPY BASE HEIGHTall=LocationVoxel(:,
end);
                                             CANOPY BASE HEIGHT= mean(CANOPY BASE
HEIGHTall)-MeanZALSGround;
                                             CANOPY BASE HEIGHTELEVATION =
mean(CANOPY BASE HEIGHTall);
                                             continue
                                         end
                                         MinZ=MinZ+VoxelZsize;
                  end


    end

                              % Calculting Volume and Area of foliage


         row_indices = any(Foliage(:,3) > min(CANOPY BASE HEIGHTall), 2);
         Foliage= Foliage(row_indices, :);
         D=size (Foliage,1);

         if D>10
         [k,AreaFoliage] = boundary(Foliage(:,1),Foliage(:,2));
         DT = delaunayTriangulation(Foliage(:,1:3));
         [C,V] = convexHull(DT);
         else
             V=0;
             AreaFoliage=0;
         end




                      % Report included: "Number of tree", "XYZ of the center of
trees", "XYZ of the tree tops","Mean of ALS ground points", "Min of ALS ground
points", "Max of ALS ground points", "the elevation of CANOPY BASE HEIGHT", "Tree
Height", "Canopy base height", "Volume of foliage", "Area of foliage",
                  Report=[Report; i,X, Y, Z, XHeight, YHeight, ZHeight,
MeanZALSGround, MinZALSGround, MaxZALSGround, CANOPY BASE HEIGHTELEVATION, Height,
CANOPY BASE HEIGHT, V, AreaFoliage];
                  Report=Report;

end
filename = 'Report.xlsx';
sheet = 'Sheet1';
xlswrite(filename, Report, sheet);
```

Vertical Vegetation Profiles

```
clc
clear
close all
format long g
N=input('Please Enter the Number of Trees=');
ALSGround= pcread("ALS.ply");
Report=[];
for i=1:N
    PC = sprintf('%d.txt',i);
    A = load(PC);
    XYZTotal=A(:,1:3);
    Classes=A(:,4);
    KOl=[XYZTotal Classes];


   % Finding Stem and Foliage Points
    ind1 = KOl(:,4) == 1;
    ind2 = KOl(:,4) == 0;

    Foliage = KOl(ind2,:);
    if size(Foliage,1)==0
        continue
    end
    FoliageXYZ= Foliage(:, 1:3);


                  VoxelZsize = 1;
                  MinX=min(FoliageXYZ(:,1)); MaxX=max(FoliageXYZ(:,1));
                  MinY=min(FoliageXYZ(:,2)); MaxY=max(FoliageXYZ(:,2));
                  MinZ=min(FoliageXYZ(:,3)); MaxZ=max(FoliageXYZ(:,3));

                  NumberofVexelZ= floor((MaxZ-MinZ)/VoxelZsize +1);
                  Foliage_pointCloud=pointCloud (FoliageXYZ);


                               roi2 = [MinX MaxX MinY MaxY (MinZ-50) (MinZ+50)];
                               indices2 = findPointsInROI(ALSGround,roi2);
                               ALS=select(ALSGround,indices2);
                               ALSXYZ = ALS.Location;
                               ALSZ1=ALSXYZ(:,3);
                               ALSZ=mean(ALSZ1);

                  for x=0:NumberofVexelZ

                               roi = [MinX MaxX MinY MaxY MinZ (MinZ+VoxelZsize)];

                               indices = findPointsInROI(Foliage_pointCloud,roi);

                               Voxel = select(Foliage_pointCloud,indices);

                               LocationVoxel=Voxel.Location;
                               D=size(LocationVoxel,1);
```

```
                                                            if D>4
                DT = delaunayTriangulation(LocationVoxel(:,1:3));
                [C,V] = convexHull(DT);
                                                            else
                                                                     V=0;
                                                            end
               HeightofVolume=(MinZ-ALSZ)+(VoxelZsize/2);
               MinZ=MinZ+VoxelZsize;



                  Report=[Report;HeightofVolume, V];


                  end
end

A=Report(:,1);
B=Report(:,2);
MinA=min(A);
MaxA=max(A);
H=floor(MaxA)+1;
Volume1=[];
for k=0:H
                 lower_threshold = k;
                 upper_threshold = k+0.50;

rows_within_range = Report(:, 1) >= lower_threshold & Report(:, 1) <=upper_threshold;


sum_of_values = sum(Report(rows_within_range, 2));
Volume1=[Volume1; upper_threshold, sum_of_values];

end

filename = 'VolumeProfile.xlsx';
sheet = 'Sheet1';
xlswrite(filename, Volume1, sheet);
```

Plot Vertical Vegetation Profiles

```
clc
clear all
close all

Plot1= load("Plot1.txt");
Plot2= load("Plot2.txt");
Plot3= load("Plot3.txt");
Plot4= load("Plot4.txt");
Plot5= load("Plot5.txt");
```

```
Plot6= load("Plot6.txt");
Plot7= load("Plot7.txt");
Plot8= load("Plot8.txt");
Plot9= load("Plot9.txt");
Plot10= load("Plot10.txt");
Plot11= load("Plot11.txt");
Plot12= load("Plot12.txt");
Plot13= load("Plot13.txt");
Plot14= load("Plot14.txt");
Plot15= load("Plot15.txt");
Plot16= load("Plot16.txt");

figure;
subplot(1, 16, 1)
plot(Plot15(:,2:2), Plot15(:,1:1), 'Color', 'Green', 'LineWidth', 1.7);
title('Plot 15');


subplot(1, 16, 2)
plot(Plot14(:,2:2), Plot14(:,1:1), 'Color', 'Green', 'LineWidth', 1.7);
title('Plot 14');

subplot(1, 16, 3)
plot(Plot6(:,2:2), Plot6(:,1:1), 'Color', 'Green', 'LineWidth', 1.7);
title('Plot 6');

subplot(1, 16, 4)
plot(Plot16(:,2:2), Plot16(:,1:1), 'Color', 'Green', 'LineWidth', 1.7);
title('Plot 16');

subplot(1, 16, 5)
plot(Plot5(:,2:2), Plot5(:,1:1), 'Color', 'Green', 'LineWidth', 1.7);
title('Plot 5');


subplot(1, 16, 6)
plot(Plot10(:,2:2), Plot10(:,1:1), 'Color', 'Green', 'LineWidth', 1.7);
title('Plot 10');

subplot(1, 16, 7)
plot(Plot13(:,2:2), Plot13(:,1:1), 'Color', 'red', 'LineWidth', 1.7);
title('Plot 13');

subplot(1, 16, 8)
plot(Plot9(:,2:2), Plot9(:,1:1), 'Color', 'red', 'LineWidth', 1.7);
title('Plot 9');

subplot(1, 16, 9)
plot(Plot11(:,2:2), Plot11(:,1:1), 'Color', 'red', 'LineWidth', 1.7);
title('Plot 11');

subplot(1, 16, 10)
plot(Plot1(:,2:2), Plot1(:,1:1), 'Color', 'red', 'LineWidth', 1.7);
title('Plot 1');
```

```
subplot(1, 16, 11)
plot(Plot8(:,2:2), Plot8(:,1:1), 'Color', 'red', 'LineWidth', 1.7);
title('Plot 8');


subplot(1, 16, 12)
plot(Plot2(:,2:2), Plot2(:,1:1), 'Color', 'red', 'LineWidth', 1.7);
title('Plot 2');


subplot(1, 16, 13)
plot(Plot3(:,2:2), Plot3(:,1:1), 'Color', 'black', 'LineWidth', 1.7);
title('Plot 3');

subplot(1, 16, 14)
plot(Plot7(:,2:2), Plot7(:,1:1), 'Color', 'black', 'LineWidth', 1.7);
title('Plot 7');

subplot(1, 16, 15)
plot(Plot4(:,2:2), Plot4(:,1:1), 'Color', 'black', 'LineWidth', 1.7);
title('Plot 4');

subplot(1, 16, 16)
plot(Plot12(:,2:2), Plot12(:,1:1), 'Color', 'black', 'LineWidth', 1.7);
title('Plot 12');

linkaxes(findall(gcf, 'type', 'axes'), 'xy');
saveas(gcf, 'high_res_figure', 'png');
```

Appendix 2: Detailed Software Parameter Screenshots

ICP Parameters

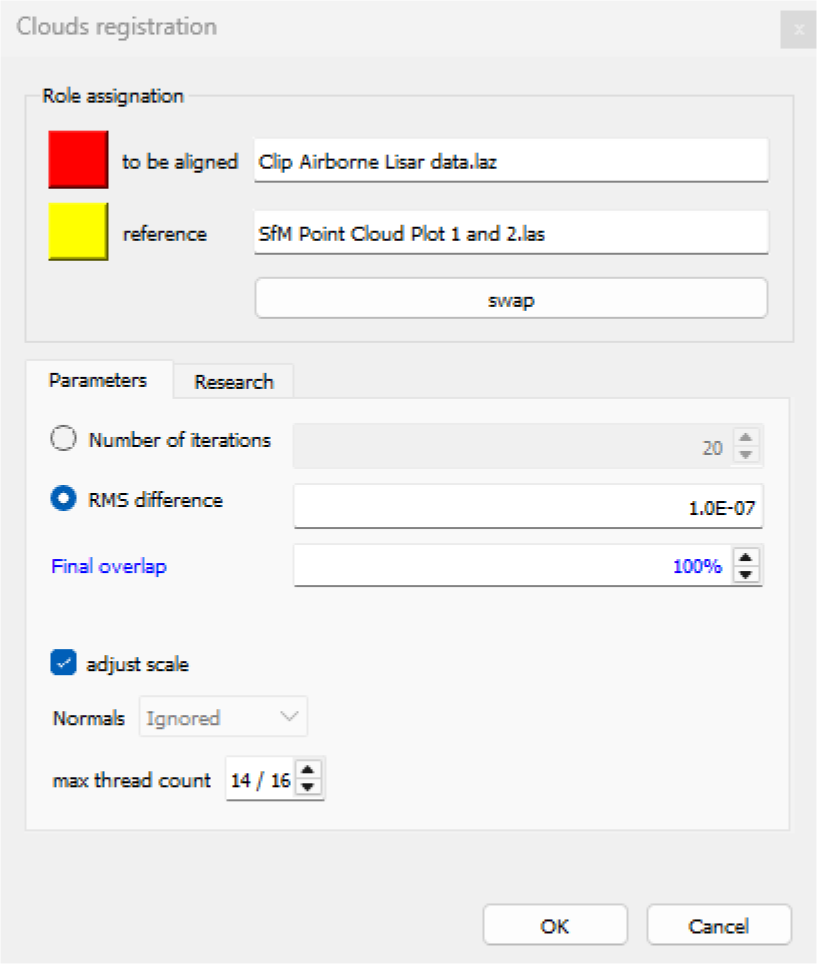

Clouds registration

Role assignation

🟥 to be aligned: Clip Airborne Lisar data.laz

🟨 reference: SfM Point Cloud Plot 1 and 2.las

○ Number of iterations: 20

● RMS difference: 1.0E-07

Final overlap: 100%

☑ adjust scale

Normals: Ignored

max thread count: 14 / 16

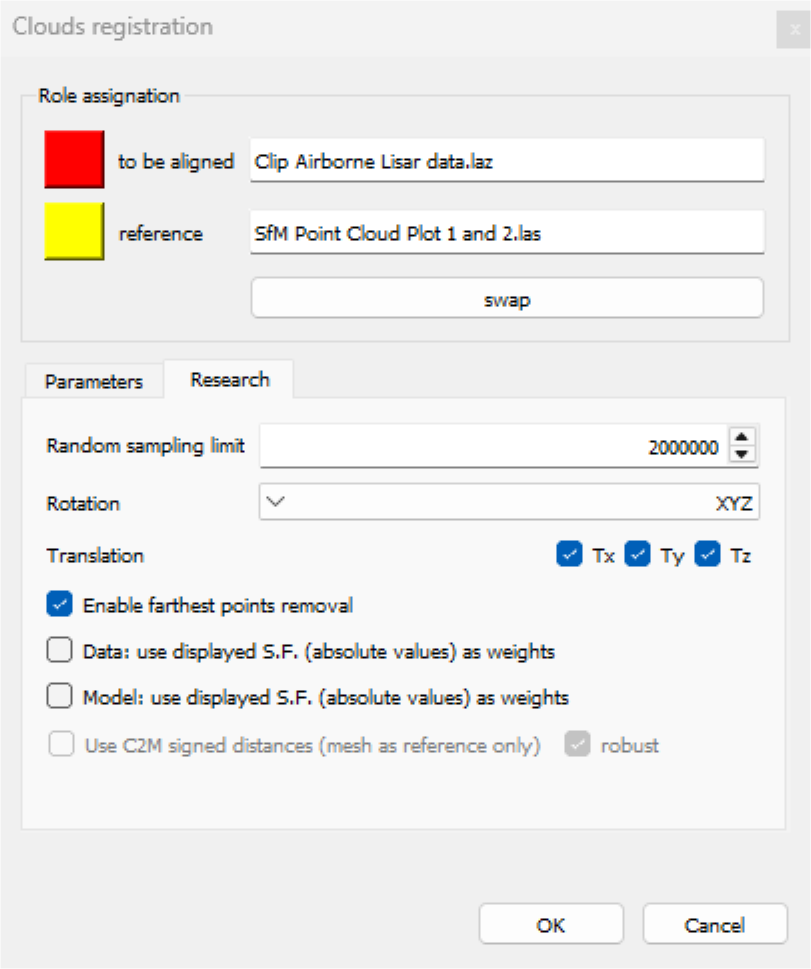

🟥 to be aligned: Clip Airborne Lisar data.laz

🟨 reference: SfM Point Cloud Plot 1 and 2.las

Random sampling limit: 2000000

Rotation: XYZ

Translation: ☑ Tx ☑ Ty ☑ Tz

☑ Enable farthest points removal

☐ Data: use displayed S.F. (absolute values) as weights

☐ Model: use displayed S.F. (absolute values) as weights

☐ Use C2M signed distances (mesh as reference only) ☑ robust

Cloth Simulation Filter (CSF)

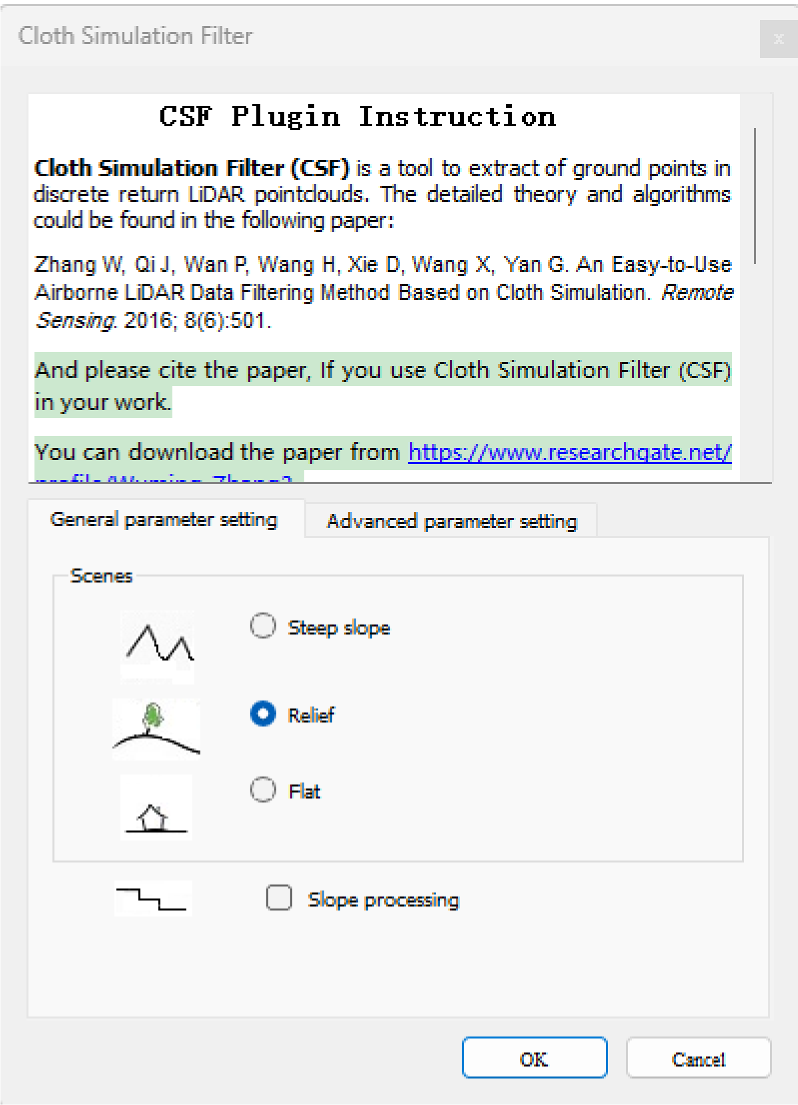

CSF Plugin Instruction

Cloth Simulation Filter (CSF) is a tool to extract of ground points in discrete return LiDAR pointclouds. The detailed theory and algorithms could be found in the following paper:

Zhang W, Qi J, Wan P, Wang H, Xie D, Wang X, Yan G. An Easy-to-Use Airborne LiDAR Data Filtering Method Based on Cloth Simulation. *Remote Sensing*. 2016; 8(6):501.

And please cite the paper, If you use Cloth Simulation Filter (CSF) in your work.

You can download the paper from https://www.researchgate.net/

○ Steep slope
● Relief
○ Flat

☐ Slope processing

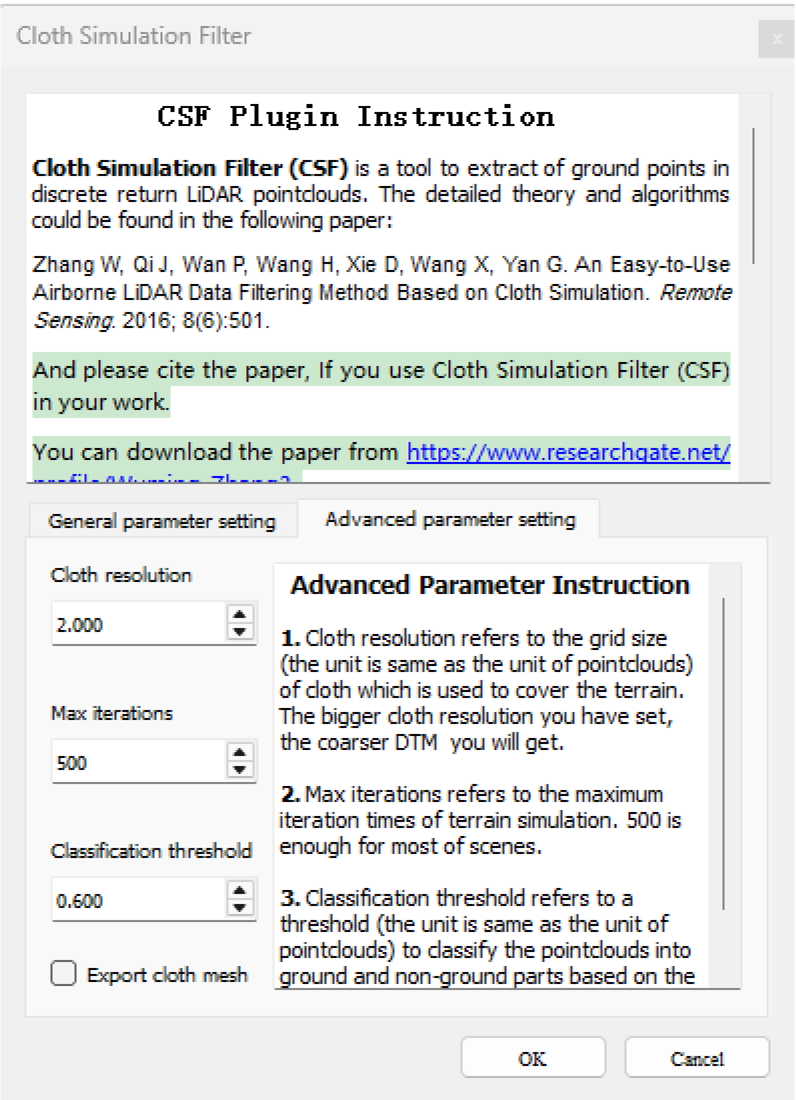

CSF Plugin Instruction

Cloth Simulation Filter (CSF) is a tool to extract of ground points in discrete return LiDAR pointclouds. The detailed theory and algorithms could be found in the following paper:

Zhang W, Qi J, Wan P, Wang H, Xie D, Wang X, Yan G. An Easy-to-Use Airborne LiDAR Data Filtering Method Based on Cloth Simulation. *Remote Sensing*. 2016; 8(6):501.

And please cite the paper, If you use Cloth Simulation Filter (CSF) in your work.

You can download the paper from https://www.researchgate.net/

Cloth resolution: 2.000

Max iterations: 500

Classification threshold: 0.600

☐ Export cloth mesh

Advanced Parameter Instruction

1. Cloth resolution refers to the grid size (the unit is same as the unit of pointclouds) of cloth which is used to cover the terrain. The bigger cloth resolution you have set, the coarser DTM you will get.

2. Max iterations refers to the maximum iteration times of terrain simulation. 500 is enough for most of scenes.

3. Classification threshold refers to a threshold (the unit is same as the unit of pointclouds) to classify the pointclouds into ground and non-ground parts based on the

The Second-Order Polynomial Transformation Parameters

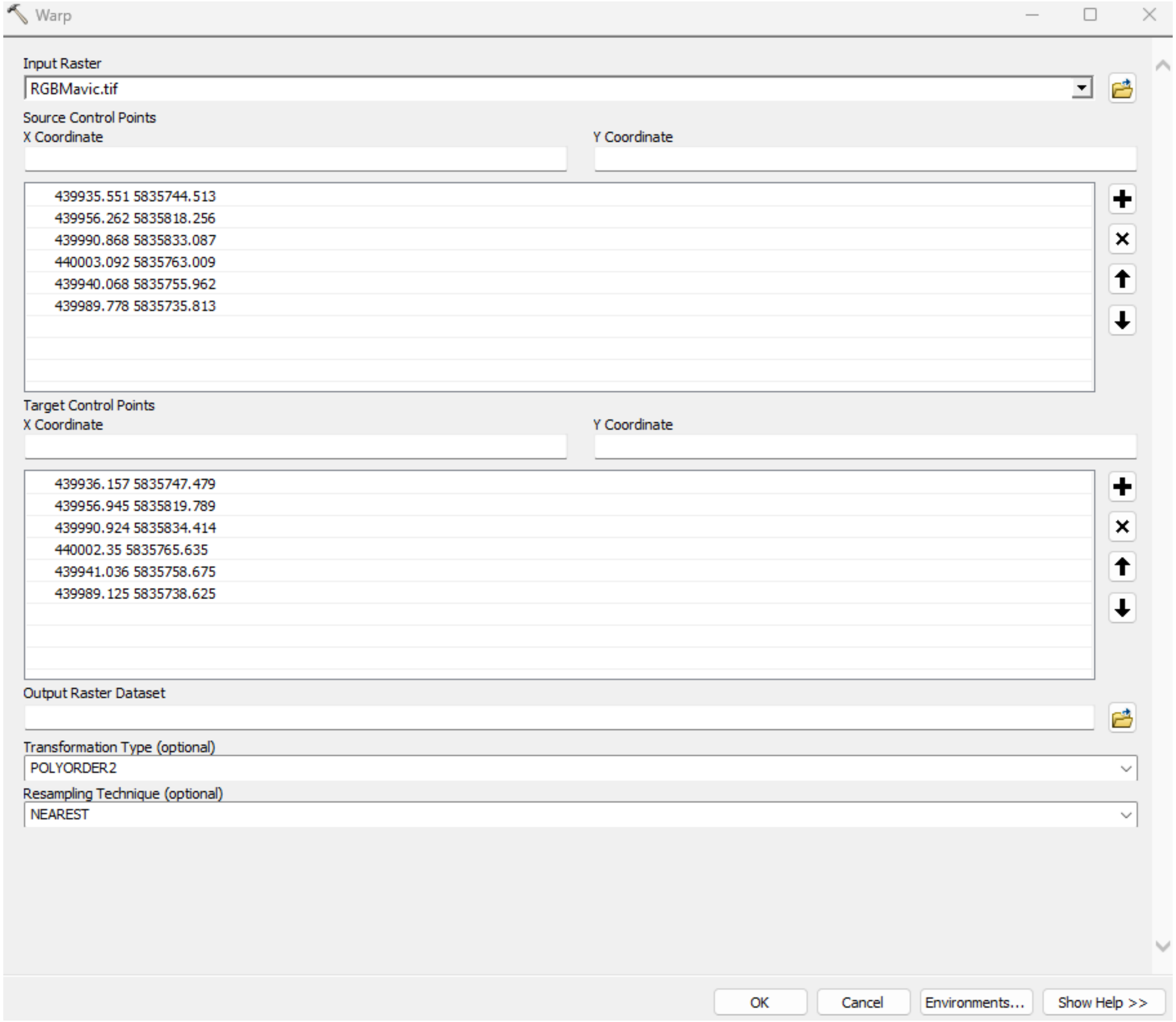

Input Raster
RGBMavic.tif

Source Control Points
X Coordinate
Y Coordinate

439935.551 5835744.513
439956.262 5835818.256
439990.868 5835833.087
440003.092 5835763.009
439940.068 5835755.962
439989.778 5835735.813

Target Control Points
X Coordinate
Y Coordinate

439936.157 5835747.479
439956.945 5835819.789
439990.924 5835834.414
440002.35 5835765.635
439941.036 5835758.675
439989.125 5835738.625

Output Raster Dataset

Transformation Type (optional)
POLYORDER2

Resampling Technique (optional)
NEAREST

TreeIso Parameters

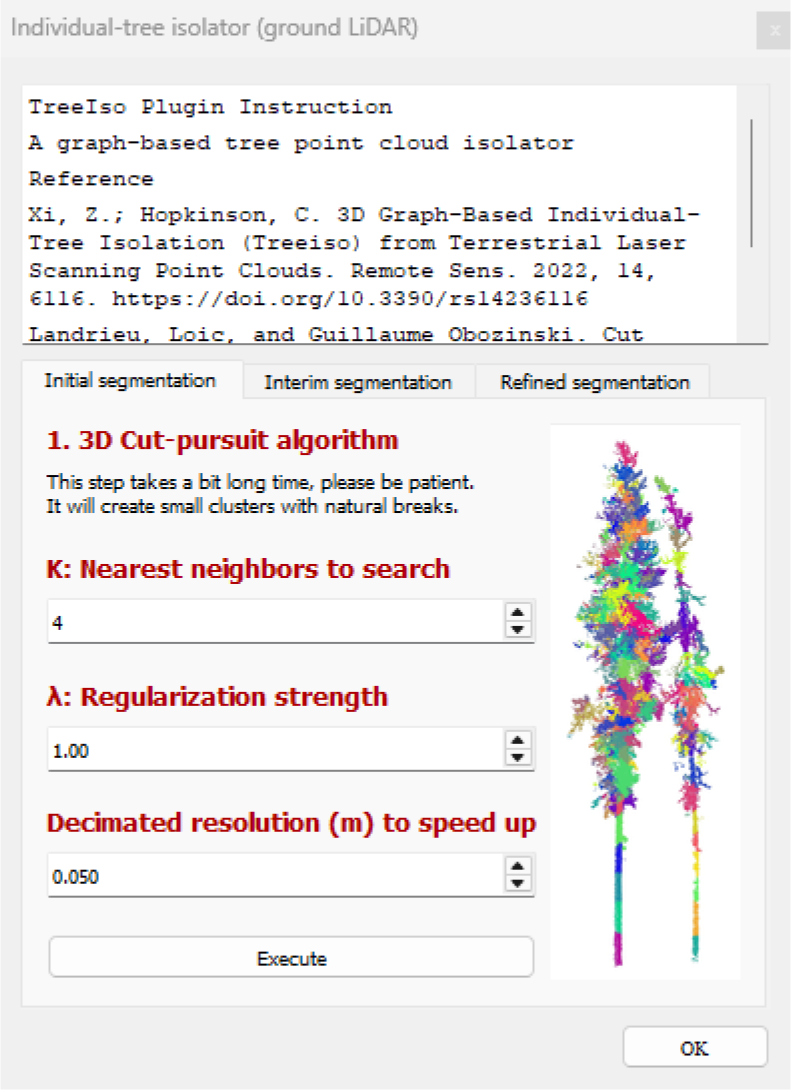

Individual-tree isolator (ground LiDAR)

TreeIso Plugin Instruction

A graph-based tree point cloud isolator

Reference

Xi, Z.; Hopkinson, C. 3D Graph-Based Individual-Tree Isolation (Treeiso) from Terrestrial Laser Scanning Point Clouds. Remote Sens. 2022, 14, 6116. https://doi.org/10.3390/rs14236116

Landrieu, Loic, and Guillaume Obozinski. Cut

1. 3D Cut-pursuit algorithm

This step takes a bit long time, please be patient.
It will create small clusters with natural breaks.

K: Nearest neighbors to search: 4

λ: Regularization strength: 1.00

Decimated resolution (m) to speed up: 0.050

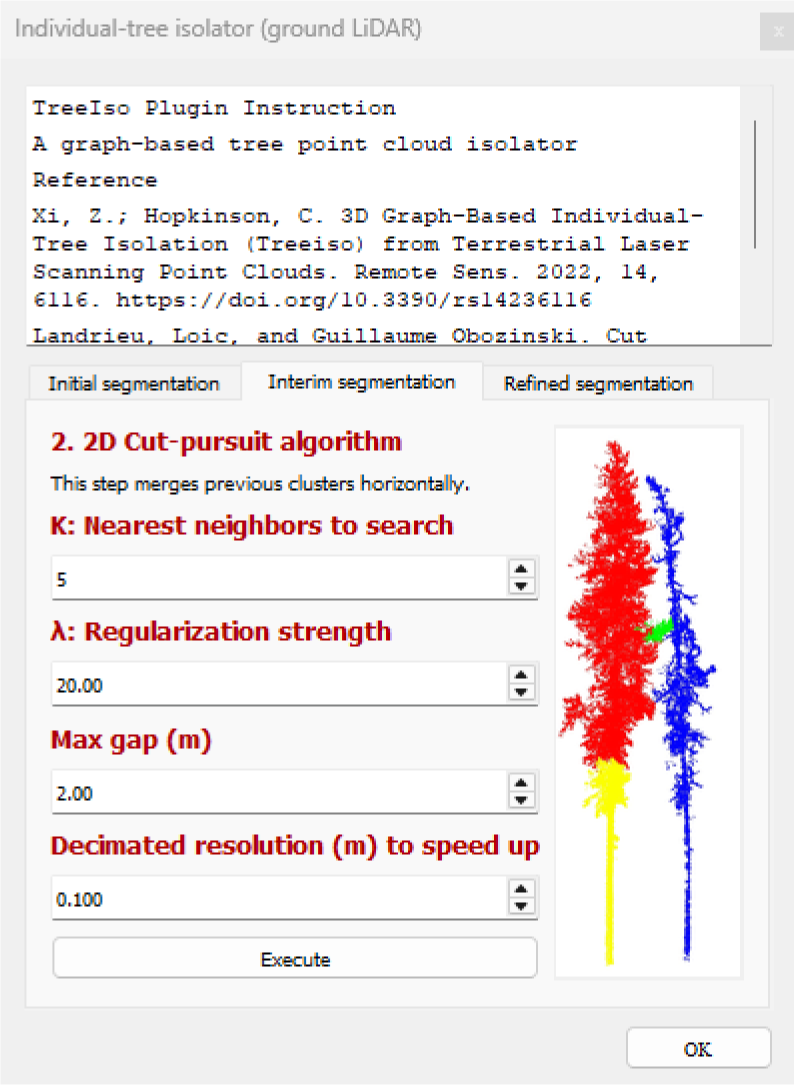

```
TreeIso Plugin Instruction
A graph-based tree point cloud isolator
Reference
Xi, Z.; Hopkinson, C. 3D Graph-Based Individual-
Tree Isolation (Treeiso) from Terrestrial Laser
Scanning Point Clouds. Remote Sens. 2022, 14,
6116. https://doi.org/10.3390/rs14236116
Landrieu, Loic, and Guillaume Obozinski. Cut
```

2. 2D Cut-pursuit algorithm

This step merges previous clusters horizontally.

K: Nearest neighbors to search

5

λ: Regularization strength

20.00

Max gap (m)

2.00

Decimated resolution (m) to speed up

0.100

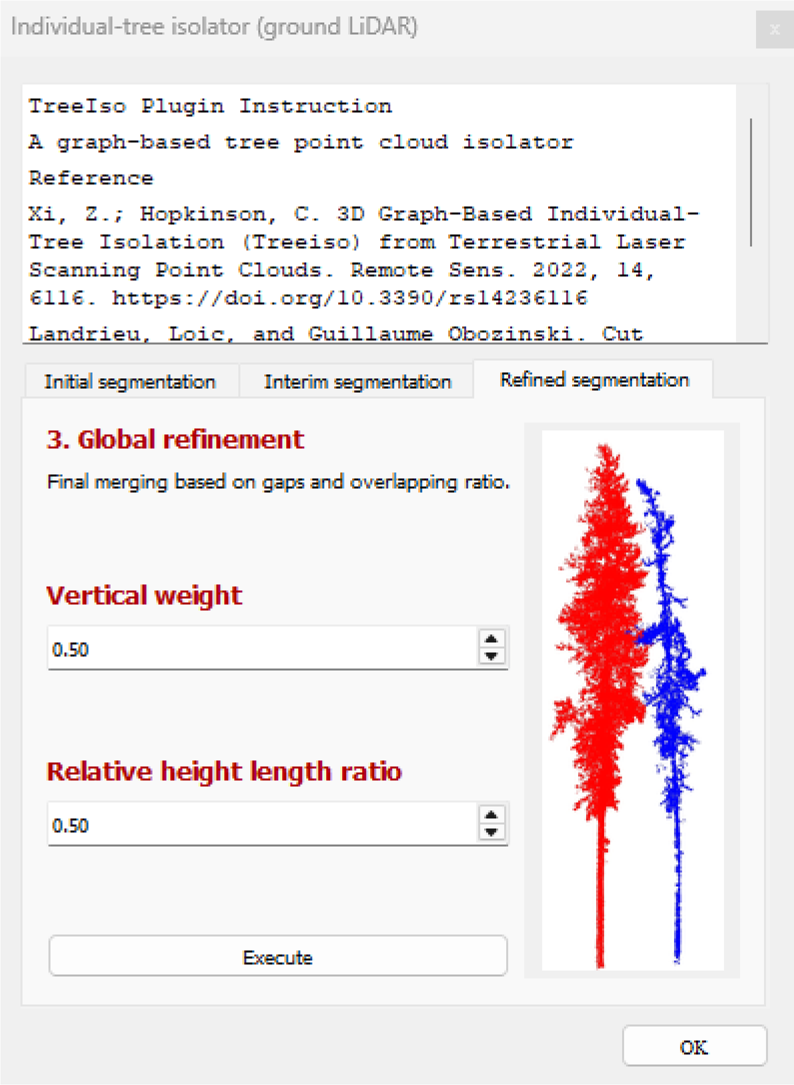

TreeIso Plugin Instruction

A graph-based tree point cloud isolator

Reference

Xi, Z.; Hopkinson, C. 3D Graph-Based Individual-Tree Isolation (Treeiso) from Terrestrial Laser Scanning Point Clouds. Remote Sens. 2022, 14, 6116. https://doi.org/10.3390/rs14236116

Landrieu, Loic, and Guillaume Obozinski. Cut

3. Global refinement

Final merging based on gaps and overlapping ratio.

Vertical weight

0.50

Relative height length ratio

0.50

Appendix 3: Confusion Matrices

Plots 1&2:

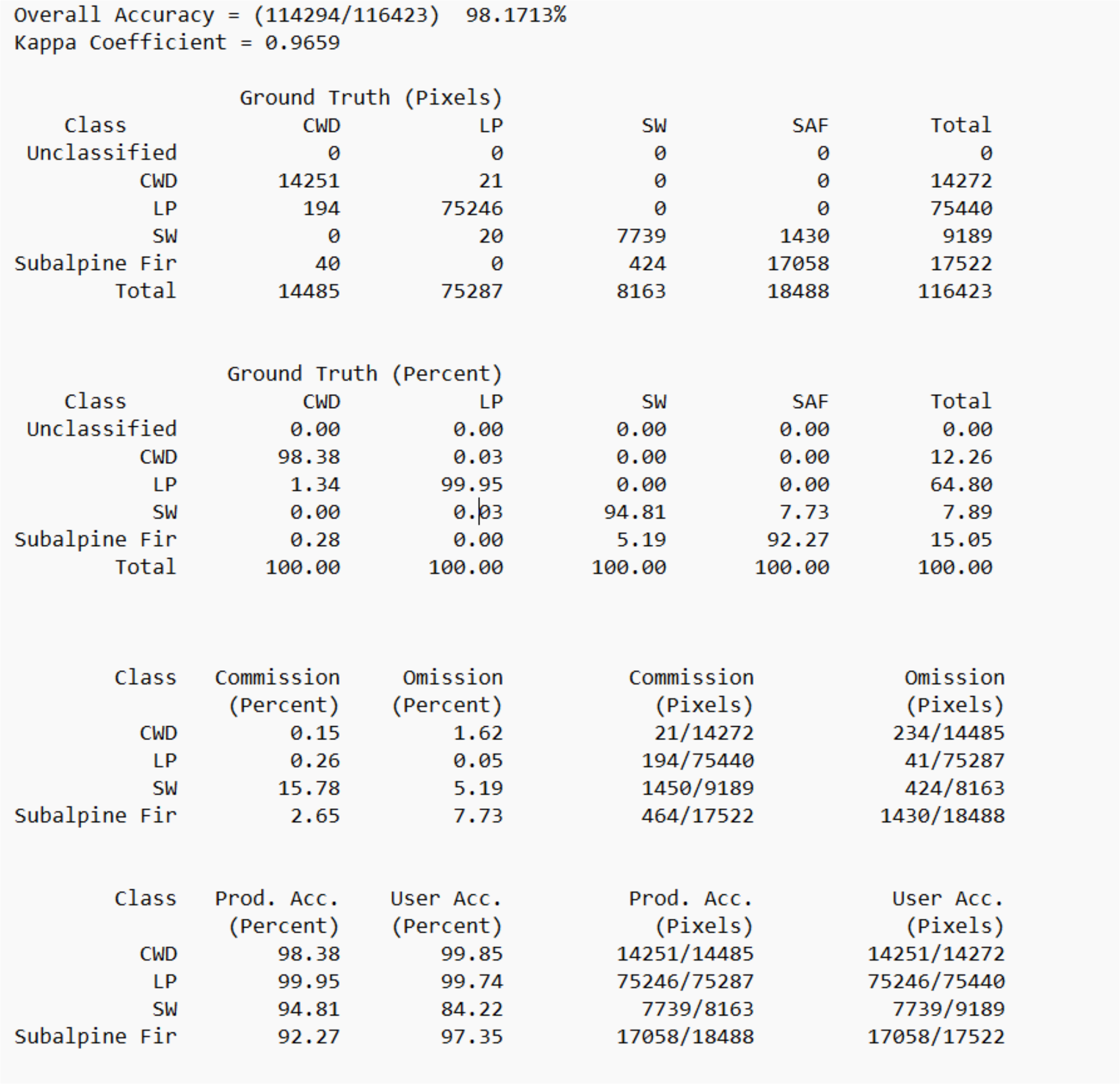

```
Overall Accuracy = (114294/116423)  98.1713%
Kappa Coefficient = 0.9659

                  Ground Truth (Pixels)
    Class              CWD           LP           SW          SAF        Total
 Unclassified            0            0            0            0            0
          CWD        14251           21            0            0        14272
           LP          194        75246            0            0        75440
           SW            0           20         7739         1430         9189
Subalpine Fir           40            0          424        17058        17522
        Total        14485        75287         8163        18488       116423


                 Ground Truth (Percent)
    Class              CWD           LP           SW          SAF        Total
 Unclassified         0.00         0.00         0.00         0.00         0.00
          CWD        98.38         0.03         0.00         0.00        12.26
           LP         1.34        99.95         0.00         0.00        64.80
           SW         0.00         0.03        94.81         7.73         7.89
Subalpine Fir         0.28         0.00         5.19        92.27        15.05
        Total       100.00       100.00       100.00       100.00       100.00



        Class   Commission     Omission          Commission            Omission
                 (Percent)    (Percent)            (Pixels)            (Pixels)
          CWD         0.15         1.62            21/14272           234/14485
           LP         0.26         0.05           194/75440            41/75287
           SW        15.78         5.19           1450/9189            424/8163
Subalpine Fir         2.65         7.73           464/17522          1430/18488


        Class   Prod. Acc.    User Acc.          Prod. Acc.           User Acc.
                 (Percent)    (Percent)            (Pixels)            (Pixels)
          CWD        98.38        99.85         14251/14485         14251/14272
           LP        99.95        99.74         75246/75287         75246/75440
           SW        94.81        84.22           7739/8163           7739/9189
Subalpine Fir        92.27        97.35         17058/18488         17058/17522
```

Plots 3&4:

```
Overall Accuracy = (244734/288948)  84.6983%
Kappa Coefficient = 0.7496

                 Ground Truth (Pixels)
    Class             CWD         SAF          LP          WS       Total
Unclassified            0           0           0           0           0
         CWD         5650           0           0           0        5650
         SAF           25       32409           0         149       32583
          LP          536       36056      138005        5836      180433
          SW           10        1514          88       68670       70282
       Total         6221       69979      138093       74655      288948


                Ground Truth (Percent)
    Class             CWD         SAF          LP          WS       Total
Unclassified         0.00        0.00        0.00        0.00        0.00
         CWD        90.82        0.00        0.00        0.00        1.96
         SAF         0.40       46.31        0.00        0.20       11.28
          LP         8.62       51.52       99.94        7.82       62.44
          SW         0.16        2.16        0.06       91.98       24.32
       Total       100.00      100.00      100.00      100.00      100.00



       Class   Commission    Omission          Commission             Omission
                (Percent)   (Percent)            (Pixels)             (Pixels)
         CWD         0.00        9.18              0/5650             571/6221
         SAF         0.53       53.69           174/32583          37570/69979
          LP        23.51        0.06        42428/180433           88/138093
          SW         2.29        8.02          1612/70282           5985/74655


       Class   Prod. Acc.   User Acc.          Prod. Acc.            User Acc.
                (Percent)   (Percent)            (Pixels)             (Pixels)
         CWD        90.82      100.00           5650/6221            5650/5650
         SAF        46.31       99.47         32409/69979          32409/32583
          LP        99.94       76.49       138005/138093        138005/180433
          SW        91.98       97.71         68670/74655          68670/70282
```

Plots 5&6:

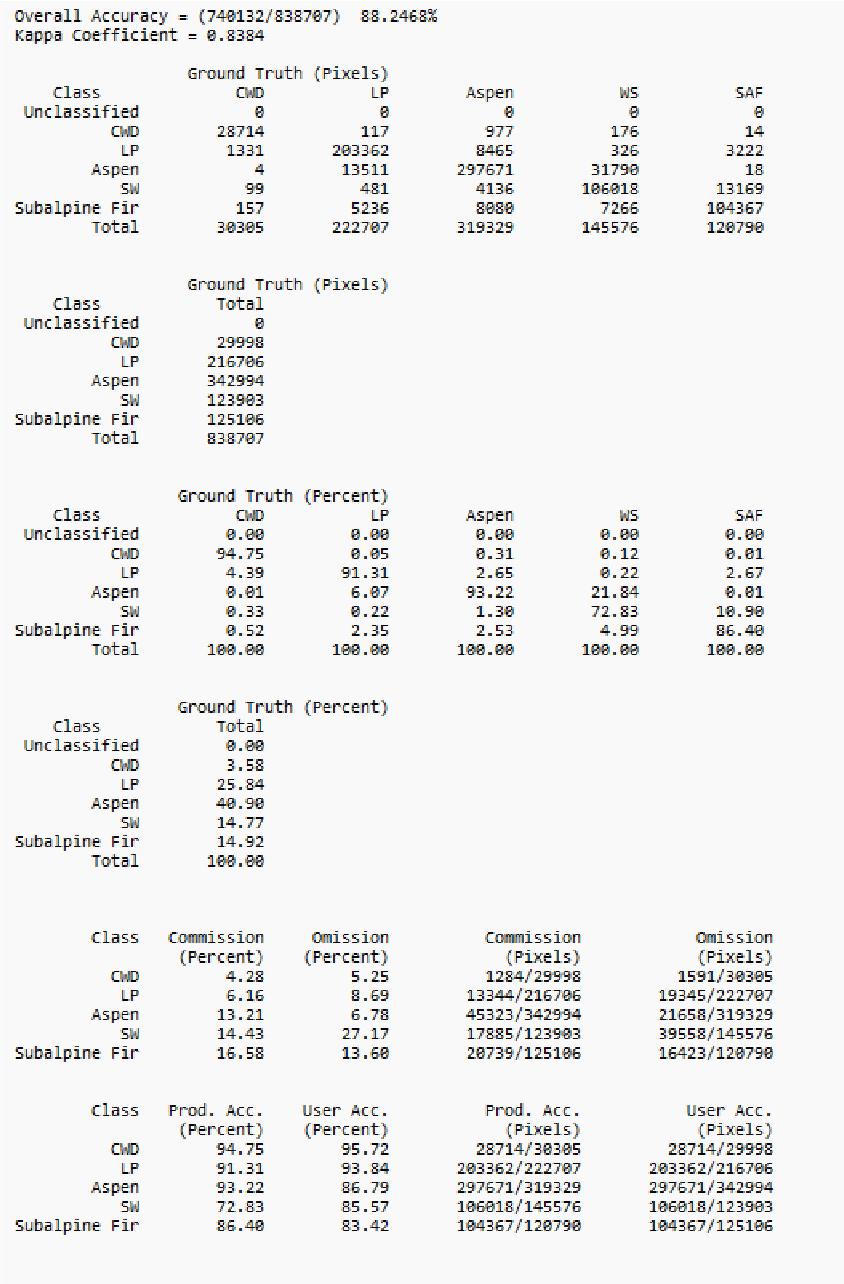

```
Overall Accuracy = (740132/838707)  88.2468%
Kappa Coefficient = 0.8384

                  Ground Truth (Pixels)
    Class              CWD           LP        Aspen           WS          SAF
 Unclassified            0            0            0            0            0
          CWD        28714          117          977          176           14
           LP         1331       203362         8465          326         3222
        Aspen            4        13511       297671        31790           18
           SW           99          481         4136       106018        13169
Subalpine Fir          157         5236         8080         7266       104367
        Total        30305       222707       319329       145576       120790


                  Ground Truth (Pixels)
    Class            Total
 Unclassified            0
          CWD        29998
           LP       216706
        Aspen       342994
           SW       123903
Subalpine Fir       125106
        Total       838707


                 Ground Truth (Percent)
    Class              CWD           LP        Aspen           WS          SAF
 Unclassified         0.00         0.00         0.00         0.00         0.00
          CWD        94.75         0.05         0.31         0.12         0.01
           LP         4.39        91.31         2.65         0.22         2.67
        Aspen         0.01         6.07        93.22        21.84         0.01
           SW         0.33         0.22         1.30        72.83        10.90
Subalpine Fir         0.52         2.35         2.53         4.99        86.40
        Total       100.00       100.00       100.00       100.00       100.00


                 Ground Truth (Percent)
    Class            Total
 Unclassified         0.00
          CWD         3.58
           LP        25.84
        Aspen        40.90
           SW        14.77
Subalpine Fir        14.92
        Total       100.00



        Class   Commission     Omission           Commission             Omission
                 (Percent)    (Percent)             (Pixels)             (Pixels)
          CWD         4.28         5.25           1284/29998           1591/30305
           LP         6.16         8.69         13344/216706         19345/222707
        Aspen        13.21         6.78         45323/342994         21658/319329
           SW        14.43        27.17         17885/123903         39558/145576
Subalpine Fir        16.58        13.60         20739/125106         16423/120790

        Class   Prod. Acc.    User Acc.           Prod. Acc.            User Acc.
                 (Percent)    (Percent)             (Pixels)             (Pixels)
          CWD        94.75        95.72          28714/30305          28714/29998
           LP        91.31        93.84        203362/222707        203362/216706
        Aspen        93.22        86.79        297671/319329        297671/342994
           SW        72.83        85.57        106018/145576        106018/123903
Subalpine Fir        86.40        83.42        104367/120790        104367/125106
```

Plots 7&8:

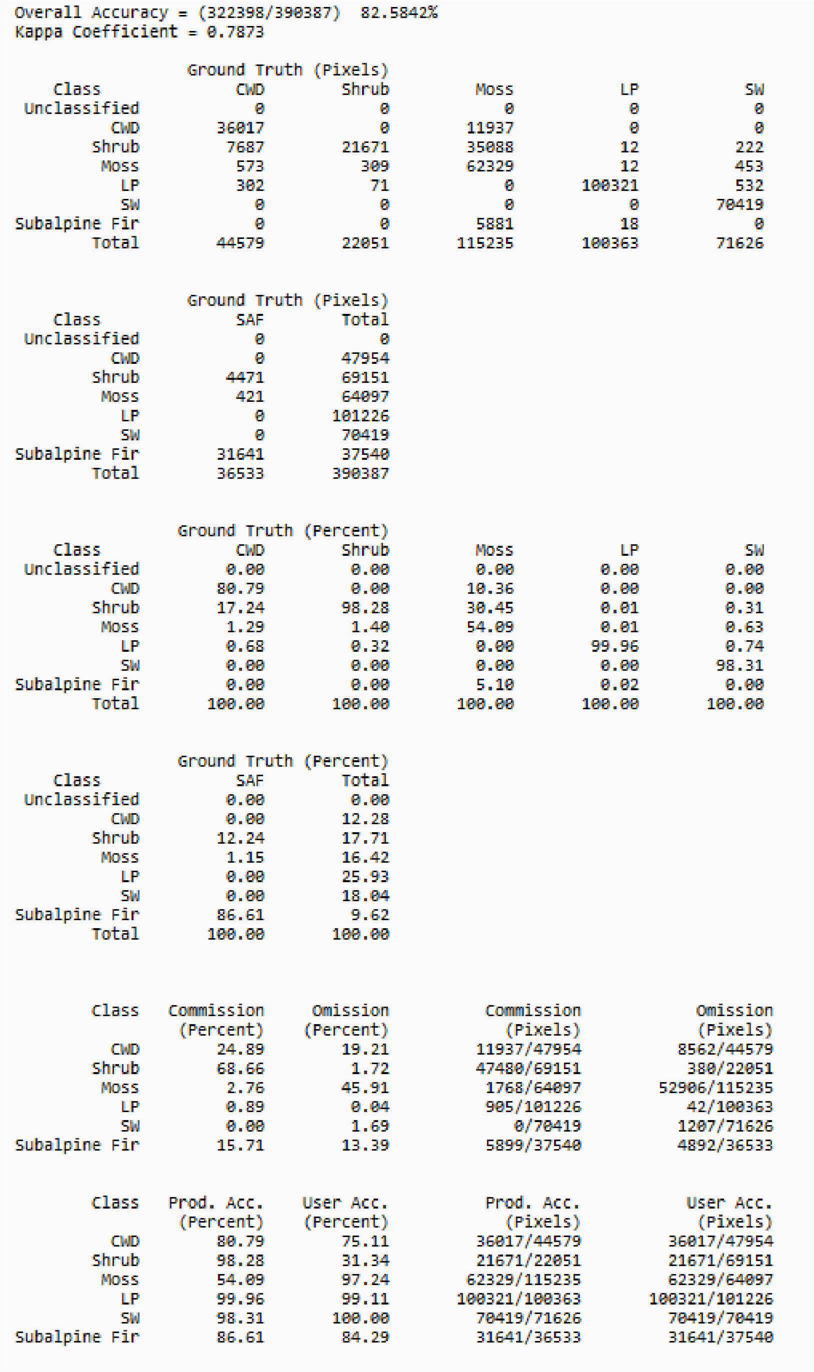

```
Overall Accuracy = (322398/390387)  82.5842%
Kappa Coefficient = 0.7873

                  Ground Truth (Pixels)
    Class              CWD        Shrub         Moss           LP           SW
 Unclassified            0            0            0            0            0
          CWD        36017            0        11937            0            0
        Shrub         7687        21671        35088           12          222
         Moss          573          309        62329           12          453
           LP          302           71            0       100321          532
           SW            0            0            0            0        70419
Subalpine Fir            0            0         5881           18            0
        Total        44579        22051       115235       100363        71626


                  Ground Truth (Pixels)
    Class              SAF        Total
 Unclassified            0            0
          CWD            0        47954
        Shrub         4471        69151
         Moss          421        64097
           LP            0       101226
           SW            0        70419
Subalpine Fir        31641        37540
        Total        36533       390387


                 Ground Truth (Percent)
    Class              CWD        Shrub         Moss           LP           SW
 Unclassified         0.00         0.00         0.00         0.00         0.00
          CWD        80.79         0.00        10.36         0.00         0.00
        Shrub        17.24        98.28        30.45         0.01         0.31
         Moss         1.29         1.40        54.09         0.01         0.63
           LP         0.68         0.32         0.00        99.96         0.74
           SW         0.00         0.00         0.00         0.00        98.31
Subalpine Fir         0.00         0.00         5.10         0.02         0.00
        Total       100.00       100.00       100.00       100.00       100.00


                 Ground Truth (Percent)
    Class              SAF        Total
 Unclassified         0.00         0.00
          CWD         0.00        12.28
        Shrub        12.24        17.71
         Moss         1.15        16.42
           LP         0.00        25.93
           SW         0.00        18.04
Subalpine Fir        86.61         9.62
        Total       100.00       100.00


        Class   Commission     Omission          Commission            Omission
                 (Percent)    (Percent)            (Pixels)            (Pixels)
          CWD        24.89        19.21         11937/47954          8562/44579
        Shrub        68.66         1.72         47480/69151          380/22051
         Moss         2.76        45.91          1768/64097        52906/115235
           LP         0.89         0.04          905/101226          42/100363
           SW         0.00         1.69             0/70419          1207/71626
Subalpine Fir        15.71        13.39          5899/37540          4892/36533

        Class   Prod. Acc.    User Acc.          Prod. Acc.           User Acc.
                 (Percent)    (Percent)            (Pixels)            (Pixels)
          CWD        80.79        75.11         36017/44579         36017/47954
        Shrub        98.28        31.34         21671/22051         21671/69151
         Moss        54.09        97.24        62329/115235         62329/64097
           LP        99.96        99.11       100321/100363       100321/101226
           SW        98.31       100.00         70419/71626         70419/70419
Subalpine Fir        86.61        84.29         31641/36533         31641/37540
```

Plots 9&10:

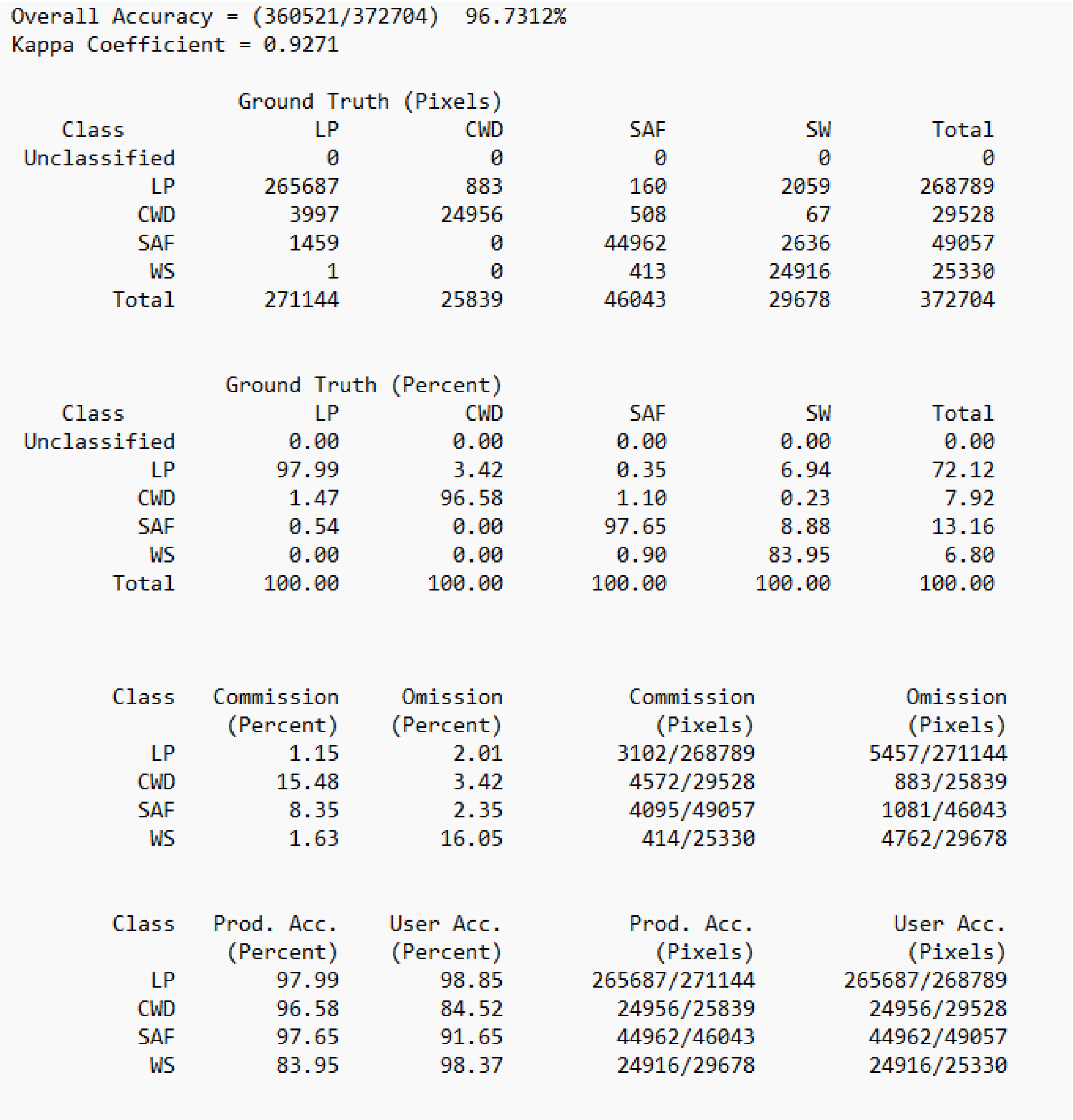

```
Overall Accuracy = (360521/372704)  96.7312%
Kappa Coefficient = 0.9271

                  Ground Truth (Pixels)
    Class                 LP           CWD          SAF           SW        Total
 Unclassified              0             0            0            0            0
          LP          265687           883          160         2059       268789
         CWD            3997         24956          508           67        29528
         SAF            1459             0        44962         2636        49057
          WS               1             0          413        24916        25330
       Total          271144         25839        46043        29678       372704


                 Ground Truth (Percent)
    Class                 LP           CWD          SAF           SW        Total
 Unclassified           0.00          0.00         0.00         0.00         0.00
          LP           97.99          3.42         0.35         6.94        72.12
         CWD            1.47         96.58         1.10         0.23         7.92
         SAF            0.54          0.00        97.65         8.88        13.16
          WS            0.00          0.00         0.90        83.95         6.80
       Total          100.00        100.00       100.00       100.00       100.00



        Class   Commission     Omission          Commission            Omission
                 (Percent)    (Percent)            (Pixels)            (Pixels)
          LP          1.15         2.01       3102/268789         5457/271144
         CWD         15.48         3.42        4572/29528           883/25839
         SAF          8.35         2.35        4095/49057          1081/46043
          WS          1.63        16.05         414/25330          4762/29678


        Class   Prod. Acc.    User Acc.          Prod. Acc.           User Acc.
                 (Percent)    (Percent)            (Pixels)            (Pixels)
          LP         97.99        98.85     265687/271144       265687/268789
         CWD         96.58        84.52       24956/25839         24956/29528
         SAF         97.65        91.65       44962/46043         44962/49057
          WS         83.95        98.37       24916/29678         24916/25330
```

Plots 11&12:

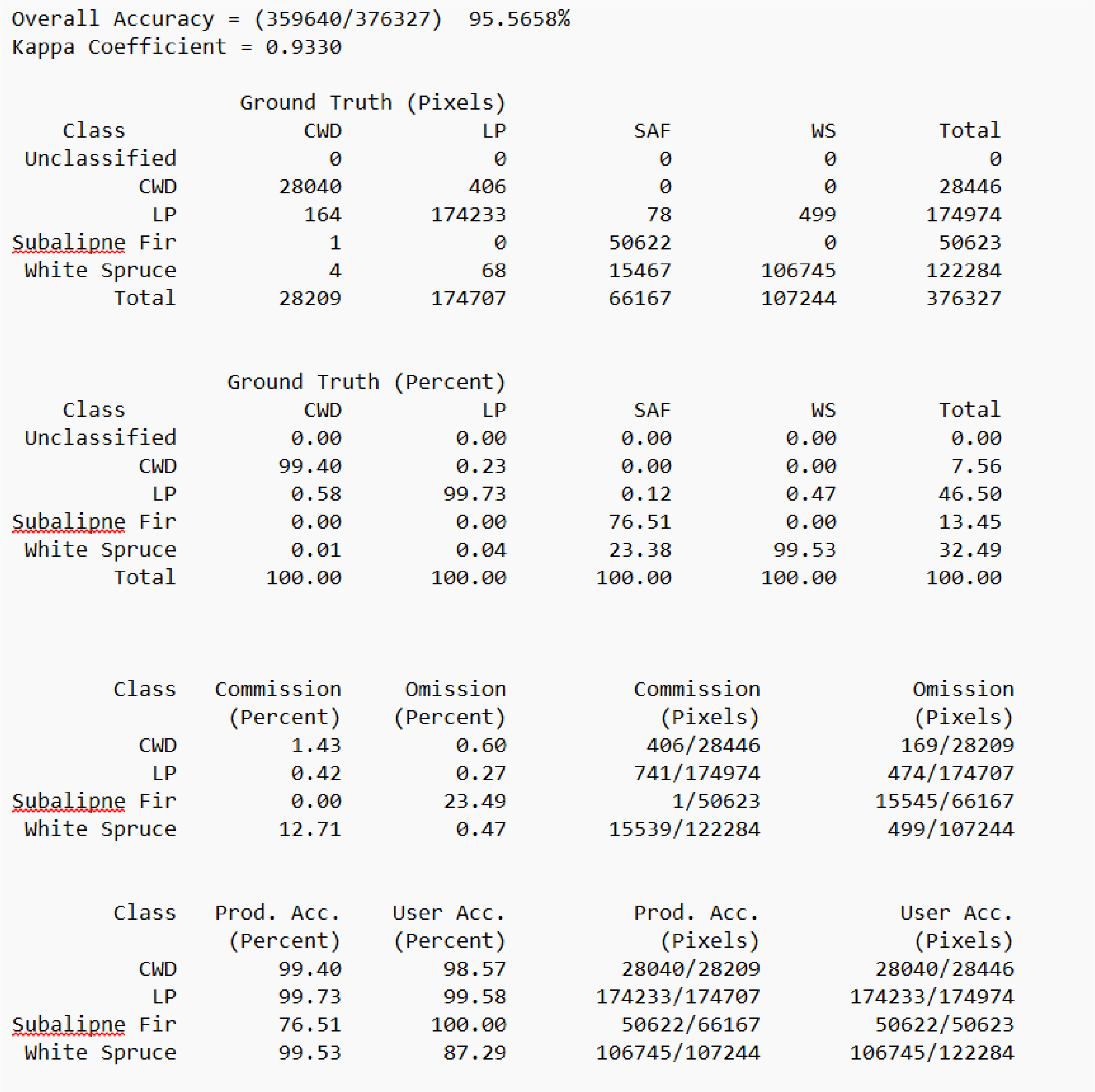

```
Overall Accuracy = (359640/376327)  95.5658%
Kappa Coefficient = 0.9330

                  Ground Truth (Pixels)
    Class            CWD          LP          SAF          WS        Total
 Unclassified          0           0            0           0            0
          CWD      28040         406            0           0        28446
           LP        164      174233           78         499       174974
Subalipne Fir          1           0        50622           0        50623
 White Spruce          4          68        15467      106745       122284
        Total      28209      174707        66167      107244       376327


                 Ground Truth (Percent)
    Class            CWD          LP          SAF          WS        Total
 Unclassified       0.00        0.00         0.00        0.00         0.00
          CWD      99.40        0.23         0.00        0.00         7.56
           LP       0.58       99.73         0.12        0.47        46.50
Subalipne Fir       0.00        0.00        76.51        0.00        13.45
 White Spruce       0.01        0.04        23.38       99.53        32.49
        Total     100.00      100.00       100.00      100.00       100.00



        Class Commission    Omission          Commission           Omission
               (Percent)   (Percent)            (Pixels)           (Pixels)
          CWD       1.43        0.60           406/28446          169/28209
           LP       0.42        0.27          741/174974         474/174707
Subalipne Fir       0.00       23.49             1/50623        15545/66167
 White Spruce      12.71        0.47        15539/122284        499/107244


        Class Prod. Acc.   User Acc.          Prod. Acc.          User Acc.
               (Percent)   (Percent)            (Pixels)           (Pixels)
          CWD      99.40       98.57         28040/28209        28040/28446
           LP      99.73       99.58       174233/174707      174233/174974
Subalipne Fir      76.51      100.00         50622/66167        50622/50623
 White Spruce      99.53       87.29       106745/107244      106745/122284
```

Plots 13&14:

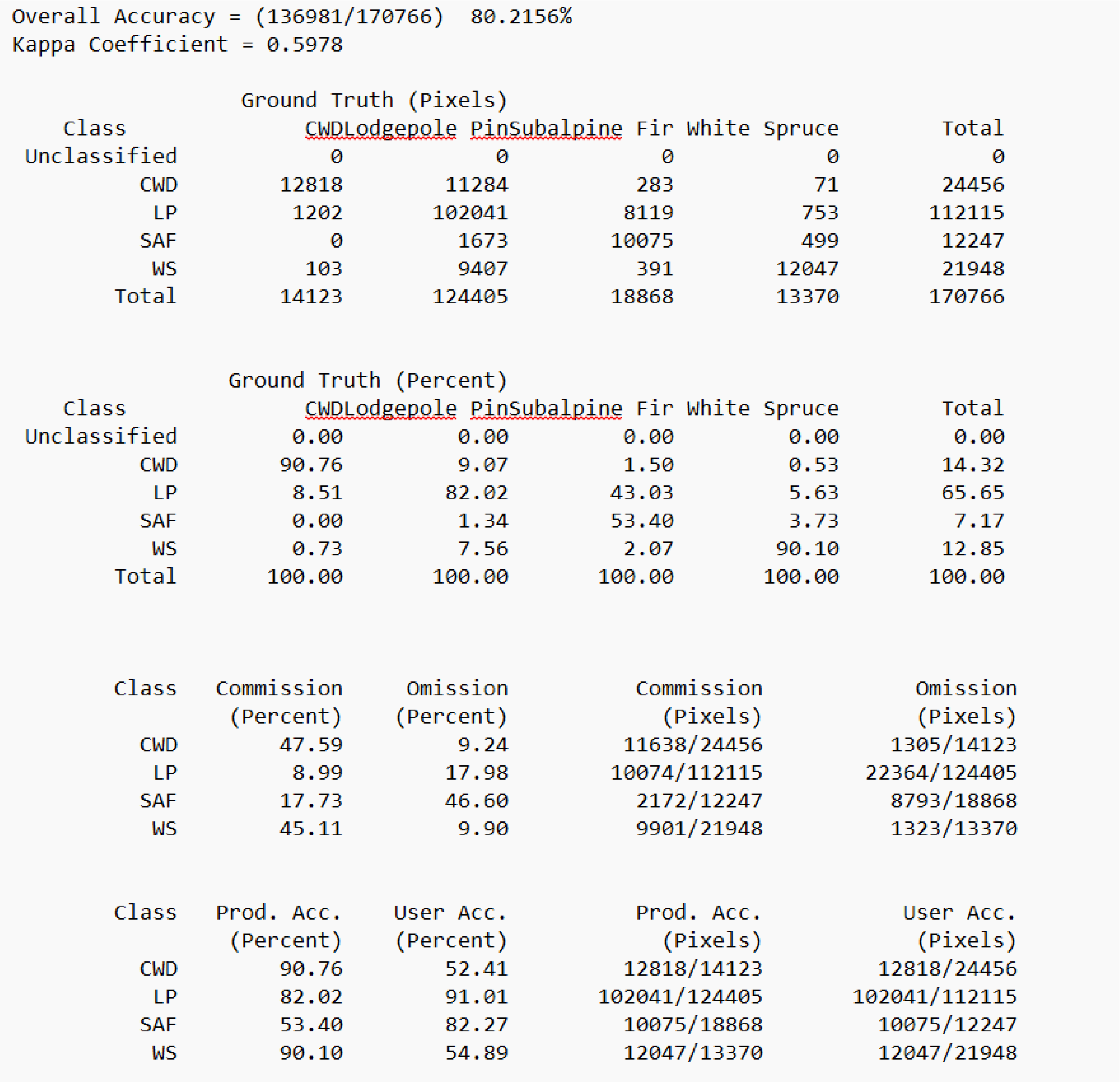

```
Overall Accuracy = (136981/170766)  80.2156%
Kappa Coefficient = 0.5978

                 Ground Truth (Pixels)
    Class             CWDLodgepole PinSubalpine Fir White Spruce         Total
 Unclassified              0            0            0            0            0
          CWD          12818        11284          283           71        24456
           LP           1202       102041         8119          753       112115
          SAF              0         1673        10075          499        12247
           WS            103         9407          391        12047        21948
        Total          14123       124405        18868        13370       170766


                Ground Truth (Percent)
    Class             CWDLodgepole PinSubalpine Fir White Spruce         Total
 Unclassified           0.00         0.00         0.00         0.00         0.00
          CWD          90.76         9.07         1.50         0.53        14.32
           LP           8.51        82.02        43.03         5.63        65.65
          SAF           0.00         1.34        53.40         3.73         7.17
           WS           0.73         7.56         2.07        90.10        12.85
        Total         100.00       100.00       100.00       100.00       100.00



        Class   Commission     Omission          Commission             Omission
                 (Percent)    (Percent)            (Pixels)             (Pixels)
          CWD        47.59         9.24         11638/24456           1305/14123
           LP         8.99        17.98        10074/112115         22364/124405
          SAF        17.73        46.60          2172/12247           8793/18868
           WS        45.11         9.90          9901/21948           1323/13370


        Class   Prod. Acc.    User Acc.          Prod. Acc.            User Acc.
                 (Percent)    (Percent)            (Pixels)             (Pixels)
          CWD        90.76        52.41         12818/14123          12818/24456
           LP        82.02        91.01       102041/124405        102041/112115
          SAF        53.40        82.27         10075/18868          10075/12247
           WS        90.10        54.89         12047/13370          12047/21948
```

Plots 15&16:

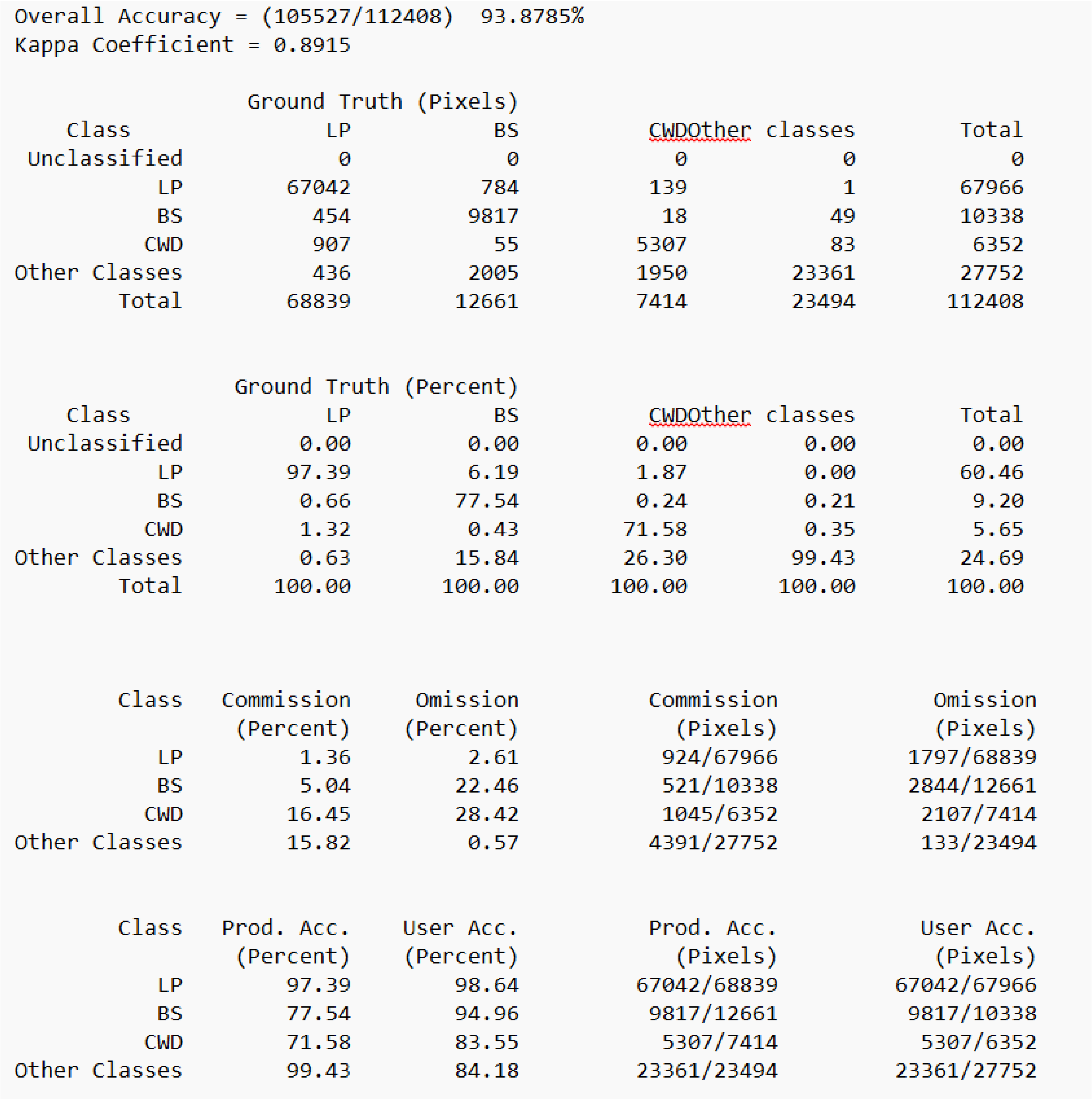

```
Overall Accuracy = (105527/112408)  93.8785%
Kappa Coefficient = 0.8915

                  Ground Truth (Pixels)
    Class               LP           BS         CWDOther classes        Total
 Unclassified            0            0            0            0            0
           LP        67042          784          139            1        67966
           BS          454         9817           18           49        10338
          CWD          907           55         5307           83         6352
Other Classes          436         2005         1950        23361        27752
        Total        68839        12661         7414        23494       112408


                 Ground Truth (Percent)
    Class               LP           BS         CWDOther classes        Total
 Unclassified         0.00         0.00         0.00         0.00         0.00
           LP        97.39         6.19         1.87         0.00        60.46
           BS         0.66        77.54         0.24         0.21         9.20
          CWD         1.32         0.43        71.58         0.35         5.65
Other Classes         0.63        15.84        26.30        99.43        24.69
        Total       100.00       100.00       100.00       100.00       100.00



        Class   Commission     Omission           Commission             Omission
                 (Percent)    (Percent)             (Pixels)             (Pixels)
           LP         1.36         2.61            924/67966           1797/68839
           BS         5.04        22.46            521/10338           2844/12661
          CWD        16.45        28.42            1045/6352            2107/7414
Other Classes        15.82         0.57           4391/27752            133/23494


        Class   Prod. Acc.    User Acc.           Prod. Acc.            User Acc.
                 (Percent)    (Percent)             (Pixels)             (Pixels)
           LP        97.39        98.64          67042/68839          67042/67966
           BS        77.54        94.96           9817/12661           9817/10338
          CWD        71.58        83.55            5307/7414            5307/6352
Other Classes        99.43        84.18          23361/23494          23361/27752
```

Appendix 4. Validation Results and Source Data for Lodgepole Pine MPB Attack Phase Classification (Table 4.7) Using GEOBIA

	Id	Field Data	Predicted
Plot 1 & 2	0	Red	Red
	1	Red	Red
	2	Red	Red
	3	Red	Red
	4	Red	Red
	5	Red	Green
	6	Green	Green
	7	Green	Green
	8	Green	Green
	9	Green	Green
	10	Green	Green
	11	Green	Green
	12	Green	Green
	13	Gray	Gray
	14	Gray	Gray
	15	Gray	Gray
	16	Gray	Red
	17	Gray	Gray
	18	Gray	Gray
	19	Gray	Gray
	20	Gray	Gray
	21	Gray	Gray
Plots 3 & 4	0	Red	Red
	1	Gray	Gray
	2	Red	Red
	3	Gray	Gray
	4	Green	Gray
	5	Gray	Gray
	6	Gray	Gray
	7	Green	Red
	8	Green	Red
Plots 5 & 6	0	Green	Green
	1	Green	Green
	2	Green	Green
	3	Green	Gray
	4	Green	Green

	5	Green	Green
	6	Green	Green
	7	Green	Green
	8	Green	Green
	9	Green	Green
	10	Green	Green
	11	Red	Red
	12	Red	Red
	13	Red	Gray
	14	Red	Red
	15	Red	Red
	16	Red	Red
	17	Gray	Red
	18	Gray	Gray
	19	Gray	Red
	20	Gray	Gray
	21	Gray	Red
	22	Gray	Gray
	23	Gray	Gray
	24	Gray	Gray
	25	Gray	Red
Plot 7 & 8	0	Green	Green
	1	Green	Green
	2	Green	Green
	3	Red	Red
	4	Red	Red
	5	Gray	Gray
	6	Gray	Red
	7	Gray	Gray
	8	Gray	Gray
	9	Gray	Red
	10	Gray	Gray
	11	Gray	Gray
Plots 9 & 10	0	Green	Green
	1	Green	Green
	2	Green	Green
	3	Green	Green
	4	Green	Green
	5	Green	Green
	6	Green	Green
	7	Gray	Gray

	8	Gray	Gray
	9	Gray	Gray
	10	Gray	Gray
	11	Red	Red
	12	Red	Gray
	13	Red	Gray
	14	Red	Green
Plots 11 & 12	0	Green	Green
	1	Green	Green
	2	Green	Green
	3	Green	Green
	4	Green	Red
	5	Green	Green
	6	Green	Green
	7	Red	Red
	8	Red	Red
	9	Red	Red
	10	Red	Red
	11	Gray	Gray
	12	Gray	Gray
	13	Gray	Gray
	14	Gray	Red
Plots 13 & 14	0	Green	Green
	1	Green	Green
	2	Green	Green
	3	Green	Green
	4	Red	Gray
	5	Red	Red
	6	Red	Red
	7	Red	Gray
	8	Red	Gray
	9	Red	Red
	10	Gray	Unclassified
	11	Gray	Unclassified
	12	Gray	Unclassified
	13	Gray	Unclassified
	14	Gray	Gray
	15	Gray	Gray
	16	Gray	Gray
	17	Gray	Gray
	18	Gray	Gray

Plots 15 & 16	0	Green	Green
	1	Green	Green
	2	Green	Green
	3	Green	Green
	4	Green	Green
	5	Green	Green
	6	Green	Green
	7	Green	Green
	8	Red	Gray
	9	Red	Gray
	10	Red	Red
	11	Red	Red
	12	Red	Red
	13	Red	Red
	14	Green	Green
	15	Green	Green
	16	Green	Green
	17	Green	Unclassified
	18	Gray	Red
	19	Gray	Red
	20	Gray	Gray
	21	Gray	Gray
	22	Gray	Red
	23	Gray	Red
	24	Gray	Red
	25	Gray	Gray
	26	Gray	Gray
	27	Gray	Green
	28	Gray	Gray
	29	Gray	Gray